UNIVERSIDAD NACIONAL AUTÓNOMA DE MÉXICO
PROGRAMA DE POSGRADO EN ASROFÍSICA

INSTITUTO DE ASTRONOMÍA (IA-CU)

A SPATIALLY RESOLVED STELLAR POPULATION STUDY OF 8 GALAXIES WITH DIRECT MEASUREMENTS OF THEIR SUPERMASSIVE BLACK HOLES

TESIS

QUE PARA OPTAR POR EL GRADO DE
MAESTRO EN CIENCIAS (ASTROFÍSICA)

PRESENTA:
ALEJANDRO MIGUEL MUNGUÍA CÓRDOVA

TUTORES PRINCIPALES:
DRA. MARIANA CANO DÍAZ
CONACyT - Instituto de Astronomía, CU.
DR. ALDO RODRÍGUEZ PUEBLA
Instituto de Astronomía, CU.

CIUDAD UNIVERSITARIA, CIUDAD DE MÉXICO, OCTUBRE 2022

Abstract

Even though relations between the central Supermassive Black Holes (SMBHs) and their host galaxies have been extensively observed and studied, to investigate the details about the co-evolution of both of them remains as a key problem to be solved in the galaxy formation and evolution scenario. In this work we intend to exploit the state of the art spatially resolved observations provided by the largest Integral Field Spectroscopy (IFS) survey of galaxies: Mapping Nearby Galaxies at APO (MaNGA), to investigate more about the co-evolution of the SMBHs and their hosts for a small sample of galaxies. We selected eight galaxies from the MaNGA final sample that also have the best constrained measurements of their central black holes (by dynamical methods and reverberation mapping as well) available in the literature.

In this work we report results of a pilot study for our sample, in which the IFS observations are carefully analysed by a self modified version of the spectra and image modelling code BAGPIPES to obtain star formation and mass assembly histories, among other results that allow us to start investigating the co-evolution of the galaxies and their central SMBHs, in a spatially resolved way which was performed defining a series of apertures that allowed us to study the evolution of the galaxies at different radial regimes. In order to complement the results, we perform a broad-band SED fitting analysis using the photometric data of the NSA.

The results that we highlight from our work are: *1)* seven of the galaxies in our sample are classified as AGNs, two of them are consistent with Type 1 AGNs and for which we were able to infer indirectly a BH mass that is very consistent with the mass provided by direct methods. The other five are consistent with a classification of Type 2 AGNs. *2)* Three galaxies in our sample are still actively forming stars, two are consistent with being quenched and also had their star formation activity peak at early epochs. Another two galaxies show a peak in their star formation history at recent epochs, which makes them consistent with being late type galaxies with young stellar populations. *3)* For the quenched galaxies we propose that the central BHs may have been responsible for maintaining them quenched over several cosmic epochs. *4)* Three galaxies are consistent with experiencing a compaction event, gas of low angu-

lar momentum feeding the central region of the galaxy. *5)* Two galaxies that quenched earlier than $z \sim 3$ and are candidates to be the descendants of the first quenchers. Since this work is a pilot study, it is our intention to extend our results by using IFS data from other public surveys in the near future in order to obtain a larger sample of galaxies, which will allow us to obtain more statistically robust conclusions.

Contents

Chapter 1

Introduction

The radius of the observable universe is estimated to be about 46.5 billion light-years, from the current cosmological parameters in a ΛCDM model, and contains about $\sim 2 \times 10^{12}$ galaxies (Conselice *et al.*, 2016). Most of the knowledge we have about these galaxies comes from observing and interpreting their electromagnetic radiation, so we now know that they are mainly composed of stars, gas, and dust. Besides of the *baryon* content of the galaxies, there is a large list of evidences, both from theory and observations, that galaxies are hosted by large gravitationally bounded structures of particles that interact mainly due to gravitational forces (and more rare times very *weakly* with ordinary matter and electromagnetic radiation) that are approximately in virial equilibrium and between $\sim 10^{2}-10^{3}$ times more massive than galaxies (Rodríguez-Puebla *et al.*, 2017) called dark matter halos (see Frenk & White, 2012, for a recent review).

According to the current paradigm of structure formation, galaxies are formed and evolved within extended dark matter haloes, where multiple physical mechanisms are responsible for self-regulating star formation and thus setting up their observed properties (for a review see Mo *et al.*, 2010; Frenk & White, 2012; Somerville & Davé, 2015). As dark matter haloes and galaxies have evolved, baryons were redistributed from an initial smooth distribution to the complex variety of structures that we observe today.

Gas radiative cooling within the haloes regulates the inflow of cold gas to galaxies. The subsequent formation of stars is regulated by a complex interaction between cold gas inflows and the gas heating outflows produced by the stars, a process that depends on halo mass (for a recent discussion see Pandya *et al.*, 2022). In low-mass halos, the stellar feedback (mostly form Supernova (SN) explosions) is able not only to heat the interstellar medium (ISM) but also to expel large gas fractions from the galaxy. For dark matter haloes larger than $\sim 10^{12}$ solar masses ($M_{\odot}$), galaxy formation theory predicts that there exists a transition above which virial equilibrium reaches temperatures with lower bary-

onic cooling efficiency (White & Rees, 1978, see also Dekel *et al.*, 2019 for a more detailed discussion on the possible existence of a 'golden mass'). Nonetheless, it is now well known that the cooling rate in massive haloes is still over-efficient in forming massive galaxies compared to what it is observed in cosmological surveys (White & Frenk, 1991; Benson *et al.*, 2003). In addition to the the long cooling time of shock-heated gas, the powerful feedback from rapidly accreting supermassive black holes (SMBHs) that heats and/or expels the gas from the galaxy, and thus suppressing the star formation (SF), has been invoked as a way to solve the over-cooling problem (see e.g., Silk & Rees, 1998; Springel & Hernquist, 2003; Benson *et al.*, 2003).

The observational evidence suggests that black holes (BHs) are ubiquitous to the centre of the galaxies (see e.g. Magorrian *et al.*, 1998; Ferrarese & Merritt, 2000; Gebhardt *et al.*, 2000; Tremaine *et al.*, 2002; Kormendy & Ho, 2013), and while there is a convincing evidence suggesting that BHs span a continuum of masses, from stellar black holes ($\sim 10 - 40$ M$_\odot$, Gies & Bolton, 1986; Greiner *et al.*, 2001; Orosz, 2003; Belczynski *et al.*, 2010; Abbott *et al.*, 2016) to intermediate ones ($\sim 10^2 - 10^4$ M$_\odot$, Miller *et al.*, 2003; Miller & Colbert, 2004; Noyola *et al.*, 2008; Graham & Soria, 2019; Graham *et al.*, 2019); the ones in the centre of the galaxies have been observed to range only between $\sim 10^4 - 10^{10}$ M$_\odot$ (Lynden-Bell, 1969; Lynden-Bell & Rees, 1971; Richstone *et al.*, 1998; Ferrarese & Ford, 2005; Kormendy & Ho, 2013; Reines & Volonteri, 2015; van den Bosch, 2016; Schutte *et al.*, 2019).[1]

As discussed above, SMBHs are leading candidates to regulate the SF in massive galaxies, specially at later times. Indeed, it is now well established that SMBHs correlate well with the properties of their host galaxies, particularly with the bulge properties (typically the relation between the SMBH mass (M_{BH}) and the stellar velocity dispersion (σ_*) is often referred to as the tightest relation overall, see e.g., Ferrarese & Merritt, 2000; Gebhardt *et al.*, 2000; Kormendy & Ho, 2013; Savorgnan & Graham, 2015; Schutte *et al.*, 2019), which is often interpreted as being consistent with a co-evolution scenario in which SMBHs regulate the growth of the galaxies (Silk & Rees, 1998; Benson *et al.*, 2003; Merloni *et al.*, 2004; Bower *et al.*, 2006; Croton, 2006; Sijacki *et al.*, 2007;

---

[1]It is interesting to notice that galaxies host approximately $\sim 10^4 - 10^6$ stellar BHs (Elbert *et al.*, 2018) plus a SMBH. Thus, within our observable universe it is expected to find about $\sim 2 \times 10^{17}$ stellar BHs and $\sim 2 \times 10^{12}$ SMBHs. Assuming a nominal mass of $\sim 10 - 20$ M$_\odot$ for stellar BHs and $\sim 10^6$ M$_\odot$ for SMBHs, the total mass expected within the observable universe is around $\sim 2 - 4 \times 10^{18}$ M$_\odot$ and $\sim 2 \times 10^{18}$ M$_\odot$ respectively for stellar and SMBHs, and thus a total mass of $\sim 4 - 6 \times 10^{18}$ M$_\odot$ in BHs. In other words, SMBHs contribute $\sim 1/2 - 1/3$ to total budget of BH mass in our observable universe despite that stellar BHs are way too numerous (a factor of 10^5). Finally, notice that the co-moving mass density of BHs is of the order of $\sim 4.1 \times 10^{-5}$ M$_\odot$/Mpc^3, or equivalently, BHs correspond roughly to $\Omega_{\mathrm{BH}} \sim 3 \times 10^{-6}$ to the total cosmic energy budget in the universe, compared to $\Omega_{\mathrm{baryons}} \sim 3 \times 10^{-3}$ of the baryons (stars+cold gas) within the galaxies (Rodríguez-Puebla *et al.*, 2020).

Merloni & Heinz, 2008; Silverman *et al.*, 2008; Shankar *et al.*, 2009; Kormendy & Ho, 2013; Bower *et al.*, 2017; Terrazas *et al.*, 2017; Weinberger *et al.*, 2017, 2018; Somerville *et al.*, 2018; Chen *et al.*, 2020) and the galaxies regulate the growth of the BHs themselves via the gas reservoir to feed the BH, disk instabilities and/or galaxy mergers. The details of the BH-galaxy co-evolution, however, remain unclear.

During their lifetime, BHs are expected to undergo several episodes of significant gas accretion which power luminous quasars or active galaxy nuclei (AGN, Salpeter, 1964; Zel'dovich & Novikov, 1964; Lynden-Bell, 1969). The total energy released by AGNs during those episodes is of the order of $\sim 10\%$ of their rest-mass energy $= M_{\mathrm{BH}}c^2$ (e.g., Tucci & Volonteri, 2017), and comparable to the amount of binding energy in the halo and energetic enough to heat, blow away or disturb the gas in the ISM to quench the SF.

1.1 Active Galactic Nuclei

As discussed above, SMBHs reside in the centre of the galaxies and AGNs are a special type of SMBHs that emit a huge amount of electromagnetic energy (with luminosities between $10^{38} - 10^{47}$ erg· s^{-1}; Hickox & Alexander, 2018) by gravitationally capturing material (typically cold hydrogen gas and/or dust) that will emit, mostly in the UV part of the spectrum (see Salpeter, 1964; Lynden-Bell, 1969; Brecher, 1976).

In energetic terms, AGNs are extraordinary powerful sources, which could cause a major impact on the intergalactic medium, and therefore in the SF regulation mechanisms, as well as in the evolution of the galaxies. That is why the galaxies that present this type of activity are ideal to carry out studies about the co-evolution of the central SMBHs and their host galaxies (Silk & Rees, 1998; Benson *et al.*, 2003; Hopkins *et al.*, 2008b,a).

According to the unified model of AGNs (see Figure 1.1), these are composed by the following components (Antonucci, 1993; Netzer, 2015):

- A compact central source, orders of magnitude smaller than a parsec, corresponding to an accretion disk around a SMBH. In the optical range of the SED this source resembles a power law.

- A Broad Line Region (BLR), corresponding to a dense ionized gas cloud, orbiting at high Keplerian velocities that can reach up to 10,000 km·s^{-1}, at a luminosity distance (D_L) between 0.1 and 1 pc from the SMBH.

- A dusty torus-shaped structure, that extends to a D_L between 0.1 and 10 pc from the SMBH.

- A Narrow Line Region (NLR) corresponding to low density ionized gas, moving at low Keplerian velocities. It emits permitted and forbidden lines with widths typically under 1,000 km·s^{-1}. It extends from the outside of the dust torus, to hundreds (or even thousands) of parsecs along the opening direction of the toroid. Much of this gas also contains dust.

- Sometimes a central jet with radio emission.
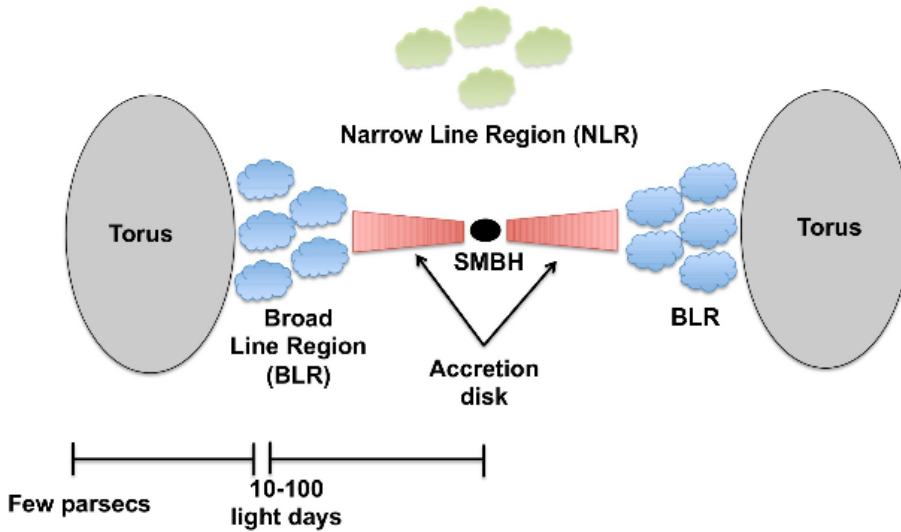
Figure 1.1: Typical structure of an AGN, according to the unified model (not to scale). The accretion disk, the BLR and the torus are under the gravitational influence of the SMBH, while the NLR is further away and under the gravitational influence of the host galaxy. Figure from Ricci, C. 2011, PhD thesis.

AGNs typically display a very broad spectrum that comprises from radio to gamma rays. Several process are responsible for the contribution to the continuum radiation of the AGN but the must probable are (O'Dell, 1986; O'Dell *et al.*, 1987):

1. Radiation by relativistic electrons (e.g., via Synchroton emission or Compton scattering),

2. Radiation by non-relativistic electrons (e.g., via bremsstrahlung and comptonization), and

3. Thermal radiation by dust that is heated by one of the above mechanisms.

Even within the unified model, AGNs can be classified into different types, depending on their photometric and spectral properties, such as the nuclear-stellar luminosity ratio (see Antonucci, 1993; Netzer, 2015), the radio emission (Urry & Padovani, 1995) or according to the presence (or lack) of strong relativistic jets (Padovani, 2017).

1.2 How Does the SF is Quenched by the SMBHs?

The Star Formation History (SFH) of a galaxy is the description of its Star Formation Rate at different epochs, $SFR(z)$. Traditionally, the SFHs have been described using parametric models, even though their stochastic nature (e.g., Caplar & Tacchella, 2019; Tacchella *et al.*, 2020; Iyer *et al.*, 2020). Among the most widely used are: exponentially increasing/decreasing, lognormal, the so-called τ-models and τ-delayed models and combinations among them. It is well known that the activity of the SMBH of a galaxy has effects on its SF, however it is not clear whether the presence of a SMBH is a sufficient condition for a galaxy to quench. Recent studies have found that it may well be that there is a BH threshold mass of $\sim 10^8$ M$_\odot$, above which they are more efficient in quenching the host galaxy (Terrazas *et al.*, 2016; Walters *et al.*, 2022). While the details behind the growth of the SMBHs and their signatures on quenching the SF are still unknown, most likely it depends on the mode that the gas is feeding the SMBH. Broadly speaking, there are two leading modes: 1) the *radiative* mode, and 2) the *radio* mode.

In the radiative mode (Croton *et al.*, 2006; Somerville *et al.*, 2018; Weinberger *et al.*, 2017, also called quasar mode, bright mode or high mode) it is thought that the gas accretion occurred very rapidly and most likely triggered by major mergers (Hopkins *et al.*, 2006) and/or by disk-gas instabilities (Cattaneo *et al.*, 2006). Notice that it is hard to reconcile the stochastic nature of the radiative mode with the fact that today galaxies, mostly the most massive ones, appeared to be quenched and kept in that way over a long period of the cosmic time, $z < 3$ (Bell *et al.*, 2004; Faber *et al.*, 2007; Ilbert *et al.*, 2013; Muzzin *et al.*, 2013).

In the radio mode (Croton *et al.*, 2006; Somerville *et al.*, 2018; Weinberger *et al.*, 2017, also called the jet mode, kinetic mode or low mode), on the other hand, the accretion of gas into the SMBH occurs more slowly resulting in a feedback and/or momentum energy that it is expected to expel the galaxy gas and/or heat the halo gas. Theoretically, highly collimated jets couple more efficiently to the halo gas until haloes reach a critical mass of $\sim 10^{12}$ M$_\odot$ (see e.g., Bower *et al.*, 2017). Thus, halo masses at which cooling efficiencies decline are similar to the halo masses where the feedback from SMBHs becomes more efficient.

By using stellar population synthesis models, various authors have shown that disk galaxies are expected to form from the *inside-out* in the standard paradigm (Kauffmann, 1996; Cole *et al.*, 2000; Firmani & Avila-Reese, 2000; van den Bosch, 2002; Stringer & Benson, 2007; Dutton & van den Bosch, 2009), this implies that the outer disks form later, i.e. the fraction of young stars increases with galactocentric radius. Indeed, gradients obtained by analytical models and numerical simulations that specifically model the inside-out formation via inflow match very well with observational results (e.g. Steinmetz & Mueller, 1994; Prantzos & Boissier, 2000).

1.3   Motivation

Studies aim at understanding the galaxy-BH connection and/or the signature of BH quenching have focused on studying the global properties of the galaxies, such as colors, star formation rates, chemical enrichment, age, etc. (Faber *et al.*, 2007; Peng *et al.*, 2010; Lilly *et al.*, 2013; Trump *et al.*, 2015; Kocevski *et al.*, 2017). Additionally, when the BH is included explicitly, the same studies have been typically biased towards broad-line and powerful AGNs that have been identified based on the most popular diagnostic methods (e.g. Trump *et al.*, 2013b,a, 2015; Kocevski *et al.*, 2017; Sánchez *et al.*, 2018).

In this work we take a different approach. We use a sample of SMBHs with the most robust determinations of BH masses from the literature (see Table 2.1 below obtained from van den Bosch, 2016) and study in detail the spatially resolved assembly histories and properties of the stellar populations in the galaxy.

The above is possible thanks to the recent development of the Integral Field Spectroscopy (IFS) technique that has allowed a higher level of detail in galaxy studies, in terms of spatial resolution, resulting in a unique opportunity to study these properties in different regions of the spatially resolved galaxies. This makes possible the study and characterization of the galaxies with an unprecedented order of accuracy and detail. In particular, in this work we will use data from the Mapping Nearby Galaxies at Apache Point Observatory (MaNGA) project, as it is one of the current state of the art IFS observational programs (Bundy *et al.*, 2015). We describe all the details of the MaNGA data in Section 2.1.

This work represents a *pilot* study in which we will carry out an analysis of the MaNGA data by using one the latest and state of the art code for modelling the spectra and photometry of the galaxies, Bagpipes (Carnall *et al.*, 2018), described in Section 3.2. Briefly, Bagpipes carries out a Bayesian analysis for finding the best fit physical parameters (of stellar, dust and nebular properties) for spectroscopic and/or photometric observations of galaxies. Based on the

above, by using BAGPIPES together with the IFS observations from MaNGA, we are in a privileged position to understand how galaxies and SMBHs coevolve not only globally but in a spatially resolved manner. In other words the main aim of this thesis project is to study the galaxy-SMBH co-evolution and the possible signatures of BH quenching from a sample of SMBHs with robust masses by inferring the stellar properties of the adjacent stellar population via BAGPIPES, from the state of the art IFS observations of the MaNGA project. In addition, we have complemented our IFS results with a photometric analysis using the surface brightness profiles in seven bands (*FUV, NUV, u, g, r, i* and *z*) in a series of circular annuli of fixed angular size from the NASA Sloan Atlas catalog (Blanton *et al.*, 2017), as described in Section 3.2.5.

In Chapter 4 we present the results of the spectroscopic analysis for each galaxy in our sample, followed by the results of a complementary photometric analysis. Finally, in Chapter 5 we discuss our results and in Chapter 6 we present the conclusions, including an outlook for what will come next in this project, given the limited scope of this pilot study for the SMBH-galaxy connection. For this thesis we use the following cosmological parameters: $H_0 = 70$ km s^{-1} Mpc^{-1}, $\Omega_M = 0.3$ and $\Omega_\Lambda = 1 - \Omega_M = 0.7$ and a Initial Mass Function (IMF) described by Kroupa & Boily (2002)[2].

---

[2]The IMF of Kroupa & Boily (2002) has been formulated based on star cluster studies. For stars more massive than the sun, the IMF has a nearly power-law form in which the number of stars increases as the stellar mass decreases, with a slope very similar to the one originally derived for field stars by Salpeter (1955), but it breaks and flattens for subsolar masses, departing significantly from a Salpeter slope and showing a turnover near the hydrogen burning limit (see more in Lada & Lada, 2003; McKee & Ostriker, 2007).

Chapter 2

Data and sample

This chapter provides details on the construction of the sample analyzed in this work. Starting with a brief summary about the IFS technique, the MaNGA catalogue is later introduced in Section 2.1. Finally, a detailed summary of the final sample is given in Section 2.2, including a first discussion about some considerations about each galaxy in our analysis.

The usage of the IFS observational technique has been recently developed and popularized in astronomy. This technique allows to simultaneously obtain image and spectral information from different regions of extended objects in the sky. A two-dimensional detector is used, which obtains a fragmented image of the focal plane, covering a wide range of wavelengths. In this way, when the telescope is pointed at an extended object, the Integral Field Unit (IFU) separates the image into an array of focal plane regions and obtains a spectrum for each of these regions.

The information obtained using IFS is stored in a special format of astronomical files known as data cubes, which contain information stored in three dimensions (x, y, λ), where x and y contain the spatial information, while λ contains the spectral one.

Lately this technique has begun to be used in big surveys of galaxies, such as: MaNGA (Bundy *et al.*, 2015), the 'Calar Alto Legacy Integral Field Area Survey' (CALIFA, Sánchez *et al.*, 2012), the 'All-weather MUse Integral-field of Nearby Galaxies++' (AMUSING++, López-Cobá *et al.*, 2020), and the 'Sydney-AAO Multi-object Integral field spectrograph' (SAMI, Croom *et al.*, 2012), among others. For our analysis we will use data from the MaNGA catalogue.

2.1 Mapping Nearby Galaxies at APO (MaNGA)

MaNGA is a spectroscopic survey of galaxies that used the IFS technique for its observations. It is one of the three projects included in the fourth version of the Sloan Digital Sky Survey (SDSS, Blanton *et al.*, 2017). It made use of the BOSS spectrographs (Smee *et al.*, 2013) installed at the Cassegrain focus of the SDSS 2.5 m telescope at the Apache Point Observatory (APO, Gunn *et al.*, 2006). Hexagonal IFUs were used, ranging in size of 19 to 127 optical fibers, covering diameters between 12 to 32 arcsec of aperture (see Figure 2.1). More details about the MaNGA hardware design are described by Drory *et al.* (2015).
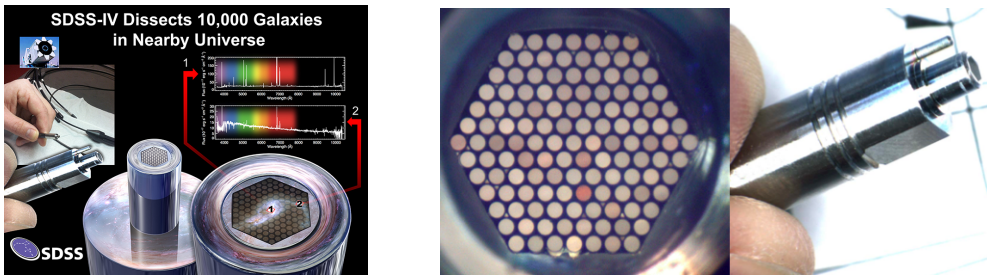

Figure 2.1: Illustrative images of a MaNGA IFU. The left illustrates how the array of fibers spatially samples a galaxy and compares spectra observed by two fibers at different locations. The right illustrates the face of a 127 fiber IFU and its ferrule housing, which holds and allows it to be plugged into the SDSS plate (see more details at Yan *et al.*, 2016). Images from `https://www.sdss.org/surveys/manga/`.

Recently the SDSS-IV made public its final Data Release, DR17 (Abdurro'uf *et al.*, 2022), which contains data for $\sim$ 10,000 galaxies in MaNGA survey. The sample of galaxies was selected from the NASA-Sloan Atlas (NSA)[1]. The main MaNGA survey galaxies are drawn from a flat stellar mass (M_*) distribution in the range $10^9 - 10^{11}$ M$_\odot$, with subsamples reaching 1.5 and 2.5 effective radii and a "color-enhanced" subsample. Details of the sample selection are given by Wake *et al.* (2017).

In this Data Release the raw data, as well as the data cubes reduced by the Data Reduction Pipeline (DRP, Law *et al.*, 2016, 2021) are totally public.[2] The data products and data cubes analyzed by the Data Analysis Pipeline (Westfall *et al.*, 2019) are also public. Alternative the data products are also available in the form of Value Added Catalogues (VAC), such as those obtained with the Pipe3D pipeline (Sánchez *et al.*, 2016b,a, 2018, 2022). The data used in

---

[1] `http://nsatlas.org/`

[2] More information about the data processing done by the DRP can also be found in `https://www.sdss4.org/dr17/manga/manga-pipeline/`

this work are the data cubes provided by the DRP reduction.[3] This reduction has processed the raw data to produce flux-calibrated, sky-subtracted, coadded data cubes from each of the individual exposures for the observed galaxies.

Each data cube contains the spectroscopic information within the visible range (3622-10351 Å), for each of the spatially resolved areas of the galaxies. The data is stored in computer files with a standard astronomical format known as FITS files (from Flexible Image Transport System)[4].

2.2 The Sample

As discussed in the Introduction, theoretically it is expected that SMBHs are responsible for quenching the SF of massive galaxies. Therefore in order to study the above it is important to have a sample with the most robust estimations of $M_{\rm BH}$ in addition of having high quality IFS spatially resolved data. To define the galaxy sample to analyze, we use one of the most recent compilations of galaxies with dynamical estimations of their $M_{\rm BH}$, provided by van den Bosch (2016), where the $M_{\rm BH}$ measurements come from different direct methods such as the analysis of stellar dynamics, gas dynamics and megamasers, or by the use of the reverberation mapping technique. This compilation includes a sample of ~ 250 galaxies, for which the values of some physical parameters, such as $M_{\rm BH}$, the luminosity in the K-band (L_K), the stellar velocity dispersion (σ_*) and the effective radius in the K-band ($R_{\rm eff,K}$) are reported.

An inference of the stellar mass of the galaxies (M_*) is obtained by using the mass-to-light ratio relationship between the L_K and M_* given by Equation 2.1 (Rodriguez-Puebla et al., *in prep.*), this mass is also referred to as $M_{*,K}$:

$$\log\left(\frac{M_{*,K}}{{\rm M}_\odot}\right) = 0.163 + 0.960\log\left(\frac{L_K}{{\rm L}_\odot}\right), \qquad (2.1)$$

where $L_\odot$ is the solar luminosity. Briefly, in order to constrain the above relation, the authors used the stellar masses from Salim *et al.* (2018) and the K-band luminosities from van den Bosch (2016).

We make a cross-correlation to find all the galaxies observed by MaNGA, that are also available in the van den Bosch (2016) compilation, resulting in a final sample of 8 galaxies: Mrk290, ARP151, NGC1194, NGC6086, NGC3982, NGC2960, NGC6264 and NGC4345. For Mrk290 the value of $R_{\rm eff,K}$ is not reported, so we use the value of $R_{\rm eff,r}$ tabulated in the NSA v1_0_1 catalogue

---

[3]Available at: `https://dr17.sdss.org/sas/dr17/manga/spectro/redux/v3_1_1/`

[4]More information can be found in: `https://fits.gsfc.nasa.gov/standard40/fits_standard40aa-le.pdf`

to estimate $R_{\text{eff,K}}$ by using color gradients[5]. Galaxy NGC4395 is a bulgeless dwarf galaxy classified as a Seyfert (see for example: den Brok *et al.*, 2015) and famous for its small BH in a low surface brightness galaxy; we have updated the value tabulated from (van den Bosch, 2016) from a value of $M_{\text{BH}} \sim 3.5 \times 10^5$ M$_\odot$ to a more recent and reliable value of $M_{\text{BH}} \sim 10^4$ M$_\odot$ reported in Woo *et al.* (2019), which is referred as "the best direct mass measurement for a galaxy of this size".

In Figure 2.2 we show our final sample of galaxies located in the M_* vs. M_{BH}, σ_* vs. M_{BH} and M_* vs. $R_{\text{eff,K}}$ diagrams, and in Table 2.1 we list some characteristic parameters and classifications of the galaxies compiled from the specialized literature.

Left panel of Figure 2.2 shows that our sample is dominated by late-type galaxies; that explains why their BHs are small compared to they counterparts for a given stellar mass. We do not see any important source of bias in the σ_* vs. M_{BH} diagram (apart from the fact that in our final sample we have just one massive galaxy, with $M_* \sim 3.6 \times 10^{11}$ M$_\odot$ and black hole mass of $M_{\text{BH}} \sim 3.7 \times 10^9$ M$_\odot$). This is reassuring, as discussed in the Introduction (Chapter 1), it is believed that the relationship between the velocity dispersion and the BH mass is the tightest correlation for the BH-galaxy co-evolution.

Finally, the right panel of Figure 2.2 shows the size-mass relation. We notice that the galaxies NGC4395, NGC3982 and Mrk290 have a very small size compared to the best fit relation from (Lange *et al.*, 2015), considering their morphological classifications, while the size of NGC6264 is a little bigger than expected. As for the other galaxies there are not other obvious sources of bias from the size-mass relations.

We notice that about 5% of all MaNGA targets come from the ancillary target programs, designed to accomplish additional scientific goals to those of the main MaNGA samples. Some ancillary programs are stand alone science projects, while some others were developed to perform calibrations or refinements of the MaNGA spectroscopic programs.[6]. Six galaxies of our final sample belong to one or more ancillary projects, as indicated in column (14) of Table 2.1, these ancillary projects are:

---

[5]We use the mean size-mass relations from Lange *et al.* (2015) parameterized as:

$$\langle R_{\text{eff},\lambda} \rangle = \gamma_\lambda \left(\frac{M_*}{\text{M}_\odot} \right)^{\alpha_\lambda} \left(1 + \frac{M_*}{M_{O,\lambda}} \right)^{\beta_\lambda - \alpha_\lambda}, \tag{2.2}$$

where λ indicates that the parameters depends on the wavelength. Then we take the ratio $\langle R_{\text{eff,K}} \rangle / \langle R_{\text{eff,r}} \rangle$ and multiply by its value of the Sérsic half-light radius that was catalogued in the in the NSA for r-band, $R_{\text{eff,r(s)}}$. The best fit values were taken from Table 3 of Lange *et al.* (2015) and for the case of early-type galaxies based on a Sérsic index cut.

[6]See more in: https://www.sdss4.org/dr17/manga/manga-target-selection/ancillary-targets/
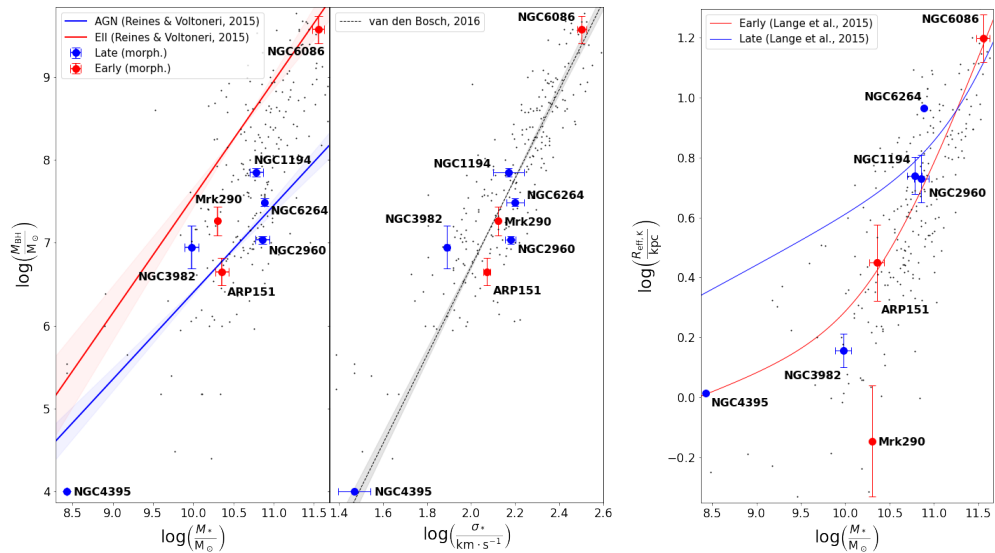
Figure 2.2: The eight galaxies of the final sample are discriminated as early-type (red circles) and late-type (blue circles) by a morphological cut. They are plotted together with the complete sample of van den Bosch (2016) (gray points). *Left panel:* M_* vs. M_{BH} diagram, where the Elliptic and the AGN slopes from Reines & Volonteri (2015) are with red and blue solid lines. *Central panel:* σ_* vs. M_{BH} diagram, where van den Bosch (2016) slope is with a black solid line; notice that all the galaxies in the sample are near the van den Bosch (2016) line and remember that this is the tightest correlation between the SMBH and the galaxy. *Right panel:* M_* vs $R_{\mathrm{eff},K}$ diagram, where the early-type and late-type slopes from Lange *et al.* (2015) are with red and blue solid lines, respectively.

- Massive Nearby Galaxies: this program aims to target massive galaxies, with absolute magnitude in the i-band (M_i) brighter than -21.5, at lower redshifts than the MaNGA sample selection in order to build a sample with comparable spatial resolution to the low mass galaxies in the MaNGA sample. In table 2.1 it is referenced as '*MNG*'.

- Luminous AGN: in aim to increase the dynamic range in AGN luminosity in the MaNGA sample, rare but luminous active galaxies were added. In order to mitigate biases, the selection of these targets was based on hard X-ray emission (using the SWIFT/BAT candidates), [O III] emission (using the SDSS main sample and the work by Mullaney *et al.* (2013)) and WISE colors (Wright *et al.*, 2010). AGNs from the Palomar survey in the DR7 footprint are also considered. These programs are respectively referenced as '*BAT*', '*OIII*', '*WISE*' and '*Palomar*'. The five narrow-line AGN galaxies in our final sample are from these programs. We emphasize

that the above should not be interpreted as a bias in MaNGA, in which its sample selection criteria cuts out the AGNs. However, a further analysis should be performed in order to quantify the frequency of Type 1 and Type 2 AGNs in the MaNGA sample, which is beyond the scope of this thesis.

- DiskMass (*DM*): galaxies from the DiskMass Survey (Bershady *et al.*, 2010) have been observed in MaNGA to compare SPS modeling obtained with MaNGA spectra and the dynamical M_* obtained from the DiskMass Survey, and to calibrate the σ_* and asymmetric-drift measurements from MaNGA against the higher-spectral-resolution results from the DiskMass Survey.

For each galaxy, Figures (2.3)-(2.10) present the *rgb*, radio and ultraviolet (*UV*) images at the field of view (FoV)[7] and their corresponding integrated spectra, as well as the data cube reconstruction images for the entire wavelength range and around the following emission lines: Hα, Hβ, [NII]6583, [OIII]5007, [SII]6717[8]. In addition, in the same figures we listed the properties tabulated in Table 2.1. In a first view we notice the following:

- Mrk290 and ARP151 are both well-identified and characterized Type 1 AGNs (see Cortes-Suárez *et al.*, 2022) exhibit prominent broad emission lines, together with narrow lines, consistent with this classification. It is evident that there is an important continuum emission which dominates the bluest part of their SEDs, mostly in Mrk290. The images from GALEX also exhibit a prominent *UV* emission in the nuclear region of both galaxies. All these facts are consistent with their classification as Markarian galaxies (ARP151 is Mrk040, Markarian, 1967, 1969); actually Mrk290 is also identified as a quasar (QSO) in the Bright Quasar Survey (BQS, Schmidt & Green, 1983) which is a subset of the Palomar-Green catalogue of stellar objects with *UV* excess (PG, Green *et al.*, 1986), being named as PG 1534+580 (see Figures 2.3 and 2.4).

- The spectra of NGC1194, NGC3982, NGC2960, NGC6264 and NGC4395 are very diverse, but all of them exhibit prominent narrow emission lines, which are characteristic of the NLR (see their integrated spectra in Figures 2.5, 2.7, 2.8, 2.9 and 2.10, respectively).

---

[7]The images were taken from `https://www.legacysurvey.org/`, considering: SDSS (Abdurro'uf *et al.*, 2022) for rgb, VLASS 1.2 (Condon *et al.*, 1998) for radio and GALEX (Martin *et al.*, 2005) for *UV*.

[8]It was not necessary to convolve the integrated fluxes with the filters, as they are only illustrative images.

- NGC1194, NGC6086 and NGC6264 exhibit a faint *UV* nuclear emission (see Figures 2.5, 2.6 and 2.9).

- NGC6086 does not exhibit emission lines in its spectrum (see Figure 2.6).

- NGC3982 and NGC4395 are part of the Kiso Survey for UV-excess Galaxies (KUG, Miyauchi-Isobe *et al.*, 2004), being identified as KUG 1153+554 and KUG 1223+338, respectively. This excess is not evident in the bluest part of the integrated visible spectrum obtained from MaNGA data, but it is very significant in their GALEX images, which exhibit an important *UV* emission in all the spiral structure of the galaxies (see Figures 2.7 and 2.10).

- NGC2960 is a Markarian galaxy (Mrk1419), in consequence it is identified as a galaxy with excessive nuclear *UV* emission (Markarian *et al.*, 1981), this is not evident in the bluest part of the integrated visible spectrum obtained from MaNGA data, but in the image from GALEX this nuclear excess can be noticed (see Figure 2.8).

- ARP151 *rgb* image shows a jet-like structure (see Figure 2.4). In fact it has been identified as a galaxy with jets in the "Atlas of Peculiar Galaxies" (Arp, 1966), but spectroscopic, imaging and radio observations indicate that the prominent optical extensions seen in its structure represent tidal tails rather than matter ejected from their nuclei (Keel, 1985), this is confirmed as it is identified as an interactive galaxy, being V-V144 in the "Atlas and Catalog of Interacting Galaxies" (Vorontsov-Velyaminov, 1959). Further study by Sargent (1970) showed that the bright knot in the middle of the "jet" exhibits no emission lines, but has Balmer absorption from an object that is 220 kms^{-1} farther than the nucleus of the host galaxy.

- The images from VLASS show that Mrk290, ARP151, NGC1194, NGC3982 and NGC2960 have a significant nuclear emission in radio, while NGC6086, NGC6264 and NGC4395 do not.

- In the images of NGC4395 it is evident that the FoV of MaNGA (the magenta hexagon) encloses only a central star cluster in the galaxy, but not the entire galaxy (see Figure 2.10).

| Name | M_{BH} | M_* | σ_* | $R_{eff,K}$ | $R_{eff,r(s)}$ | $R_{eff,r(p)}$ | b/a | PA | z | Morph. | AGN | Method | Ancillary | Ref. |
| | $\log(M_\odot)$ | $\log(M_\odot)$ | $\log\left(\frac{km}{s}\right)$ | $\log(kpc)$ | $\log(kpc)$ | $\log(kpc)$ | | degrees | | | | | | |
(1)	(2)	(3)	(4)	(5)	(6)	(7)	(8)	(9)	(10)	(11)	(12)	(13)	(14)	(15)
MRK290 8553-1901	7.26 ±0.17	10.30	2.12[a]	-0.31[b]	-0.06	-0.22	0.90	136.94	0.0302	E	S1.5	reverb	-	[1]
ARP151 9000-1901	6.65 ±0.16	10.36 ±0.08	2.07 ±0.01	0.45 ±0.13	0.17	0.01	0.74	158.34	0.0207	S0	S1[c]	reverb	-	[2]
NGC1194 9193-12701	7.85 ±0.05	10.78 ±0.08	2.17 ±0.07	0.74 ±0.06	0.79	0.62	0.70	143.44	0.0136	Sa	S1.9	maser	BAT, OIII	[3]
NGC6086 9028-6102	9.57 ±0.17	11.55 ±0.07	2.50 ±0.02	1.20 ±0.08	1.12	0.88	0.75	2.77	0.0318	Edc	-	star	MNG	[4]
NGC3982 10510-12704	6.95 +0.26 -6.95	9.98 ±0.09	1.89 ±0.01	0.16 ±0.06	0.16	0.14	0.88	12.46	0.0037	Sc	S1.9	gas	Palomar, DM	[5]
NGC2960 10514-9102	7.03 ±0.05	10.86 ±0.09	2.18 ±0.02	0.73 ±0.08	0.93	0.58	0.79	49.37	0.0164	merger	S3, LINER	maser	Palomar	[6,7]
NGC6264 11952-12704	7.49 ±0.05	10.88	2.20 ±0.04	0.96	1.13	0.92	0.67	34.22	0.0338	SABb	S2	maser	Palomar	[6]
NGC4395 12483-9102	4.00[d]	8.43	1.47 ±0.07	0.01	0.53	0.54	0.69	131.13	0.0011	SABd	S1.8	reverb, gas	Palomar	[8,9]

Table 2.1: Final Sample of galaxies with IFS observations by MaNGA and M_{BH} direct estimations reported in van den Bosch (2016). (1) Name and MaNGA plate-ifu unique name. (2) BH mass. (3) Stellar mass obtained by the luminosity L_K in Equation 2.1.(4) Stellar velocity dispersion inside the half-light radius. (5) Half-light radius in the K-band, derived from the growth curves. (6) Sérsic 50% light radius along major axis in the r-band. (7) Elliptical Petrosian 50% light radius in r-band, no corrections. (8) Axis ratio used for elliptical apertures. (9) Angle (E to N) of major axis in two-dimensional, single-component Sérsic fit in r-band. (10) Heliocentric redshift. (11) Morphology classification from Vázquez-Mata et al. (2022). (12) AGN classification from Véron-Cetty & Véron (2006) unless another reference is indicated. (13) Method used for M_{BH} measurement where *reverb* refers to the reverberation mapping technique, *star* refers to stellar dynamics, *gas* refers to gas dynamics and *maser* refers to megamasers. (14) MaNGA ancillary target program. (15) Literature reference in van den Bosch (2016) for M_{BH} and galactic parameters, with: [1] Denney et al. (2010), [2] Bentz et al. (2010, see also Valenti et al., 2015), [3] Kuo et al. (2011), [4] McConnell et al. (2011), [5] Beifiori et al. (2012), [6] Kuo et al. (2011), [7] van den Bosch et al. (2015), [8] Peterson et al. (2005), [9] den Brok et al. (2015). [a]: σ_* obtained from MaNGA DAP. [b]: $R_{eff,K}$ converted from r-band to K-band as described in text. [c]: AGN classification from Khachikian & Weedman (1974). [d]: M_{BH} updated from a more recent direct measurement by Woo et al. (2019).
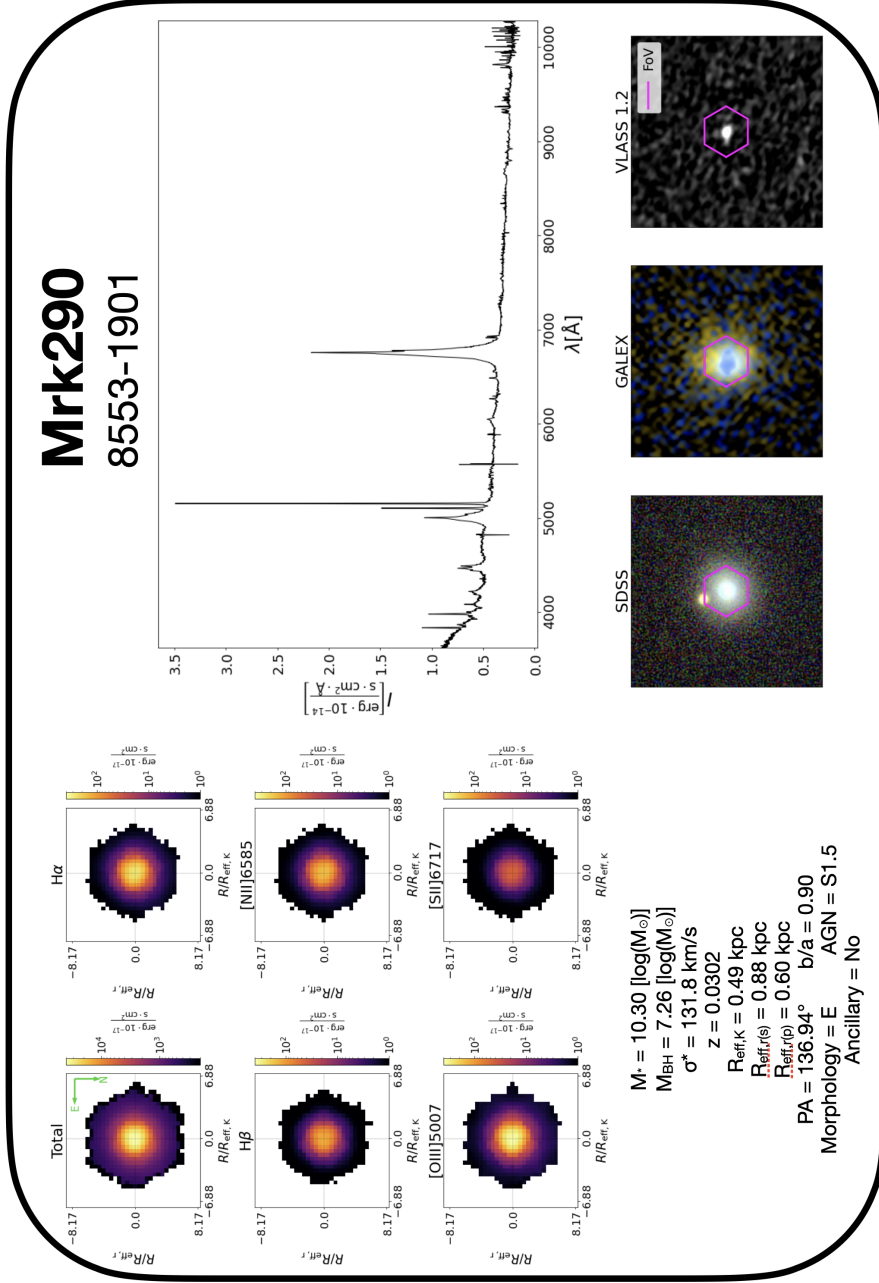
Figure 2.3: Summary of **Mrk290**. The *upper-left* shows the images of the data cube, integrated at the total wavelength range and at different wavelength ranges around the vicinity of the following emission lines: Hα, Hβ, [Nɪɪ]6585, [Oɪɪɪ]5007 and [Sɪɪ]6717. In the *lower-left* side there is a summary of the galaxy main characteristics. The *upper-right* side shows the integrated full spectrum at the MaNGA FoV. In the *lower-right* side there are the *rgb*, *UV* and radio images, showing the MaNGA FoV with a magenta hexagon.
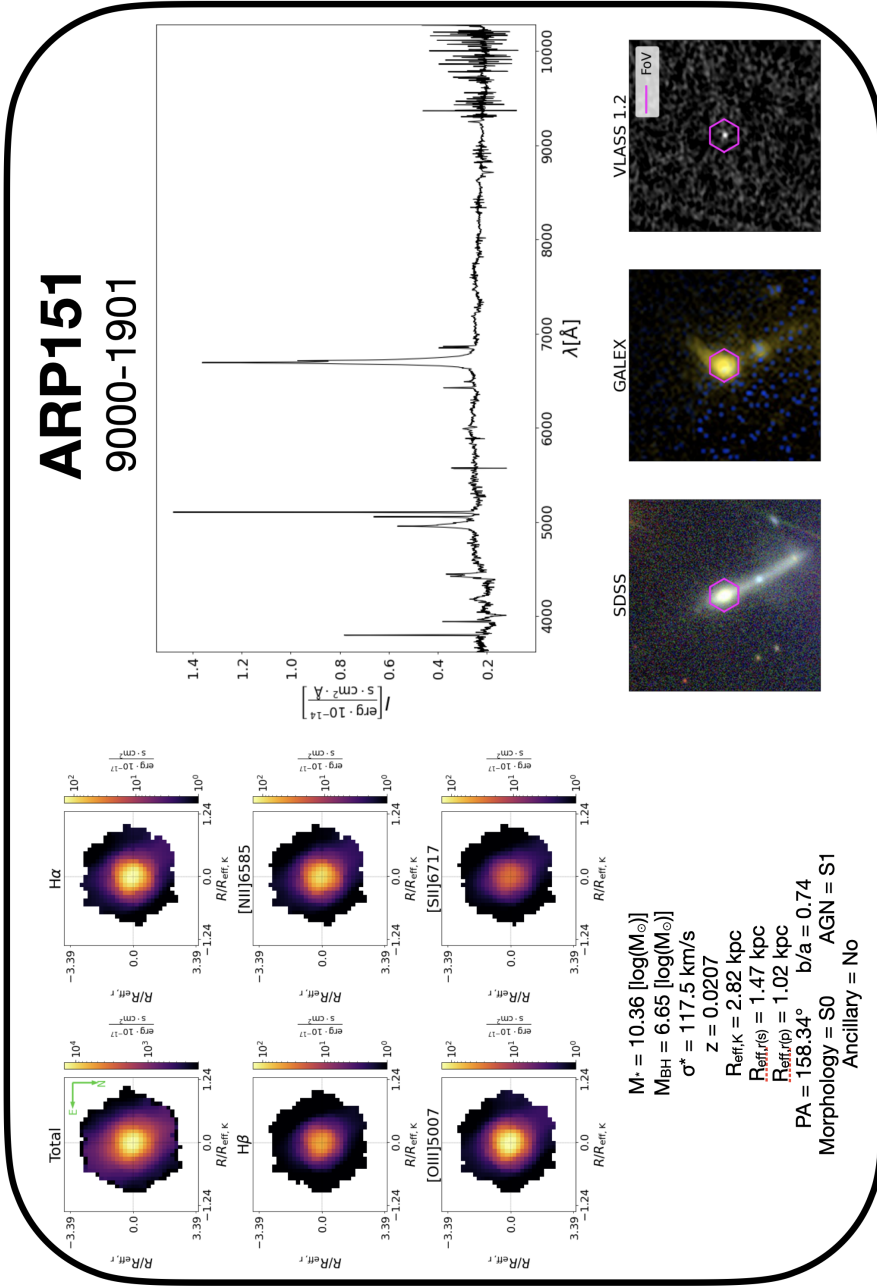
Figure 2.4: Summary of **ARP151**. The description is similar to Figure 2.3.

Figure 2.5: Summary of **NGC1194**. The description is similar to Figure 2.3
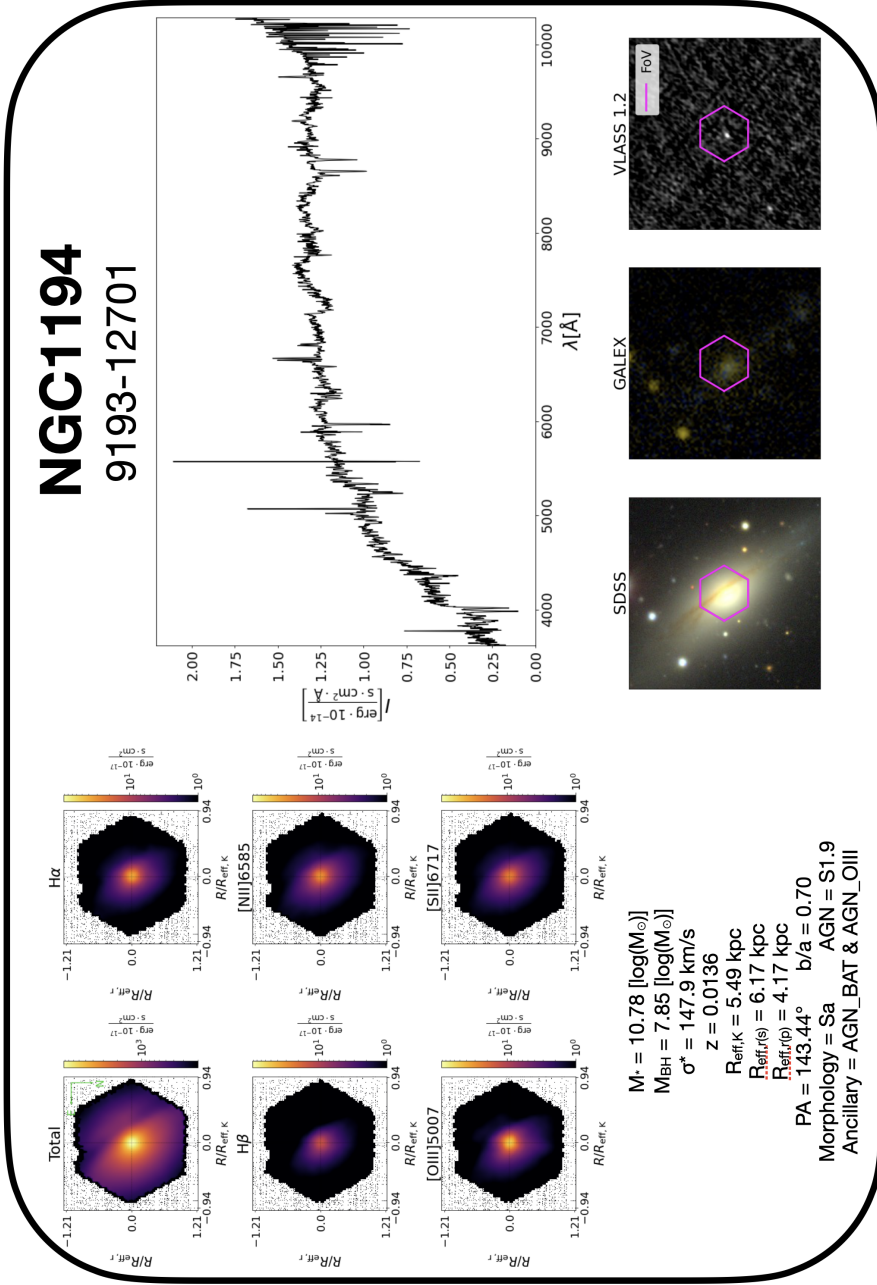
Figure 2.6: Summary of **NGC6086**. The description is similar to Figure 2.3

Figure 2.7: Summary of **NGC3982**. The description is similar to Figure 2.3

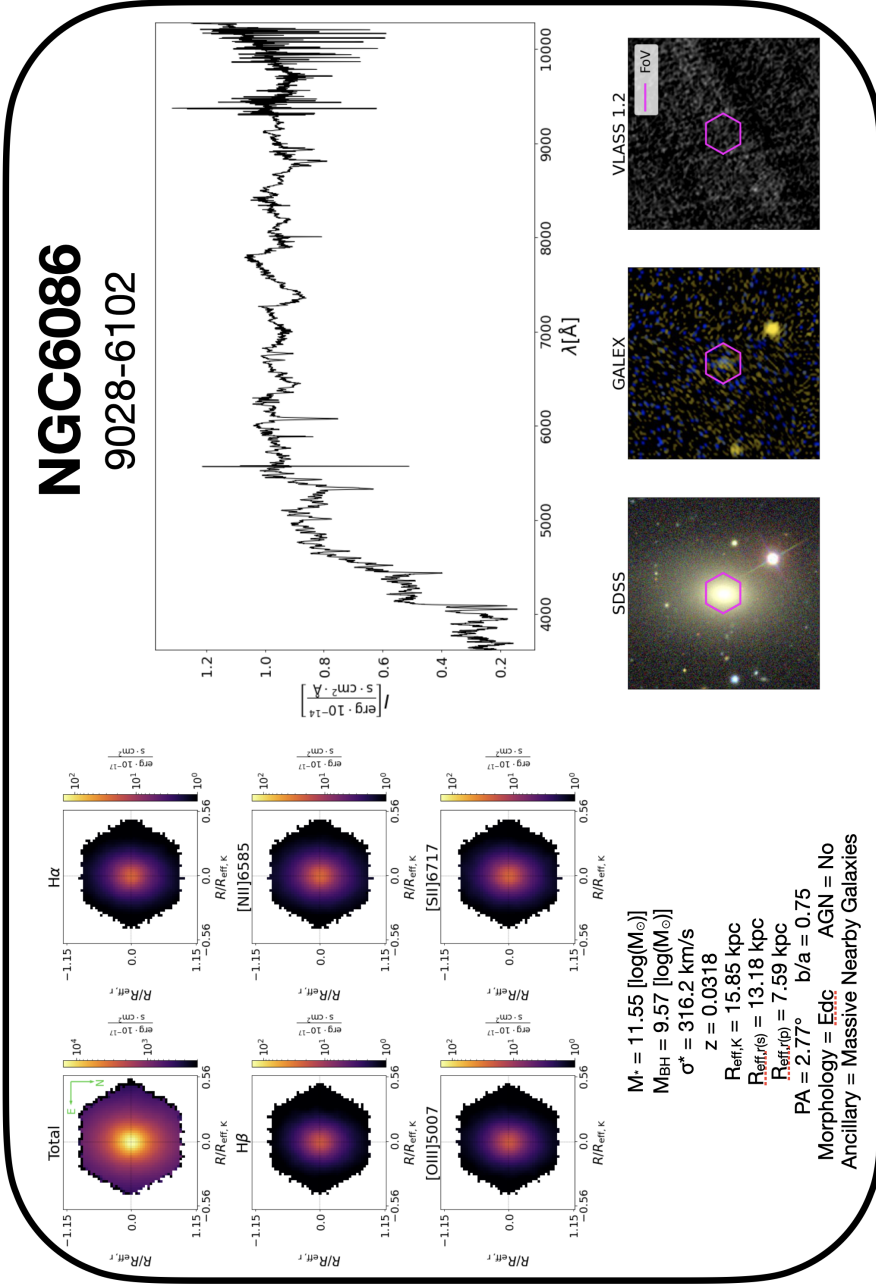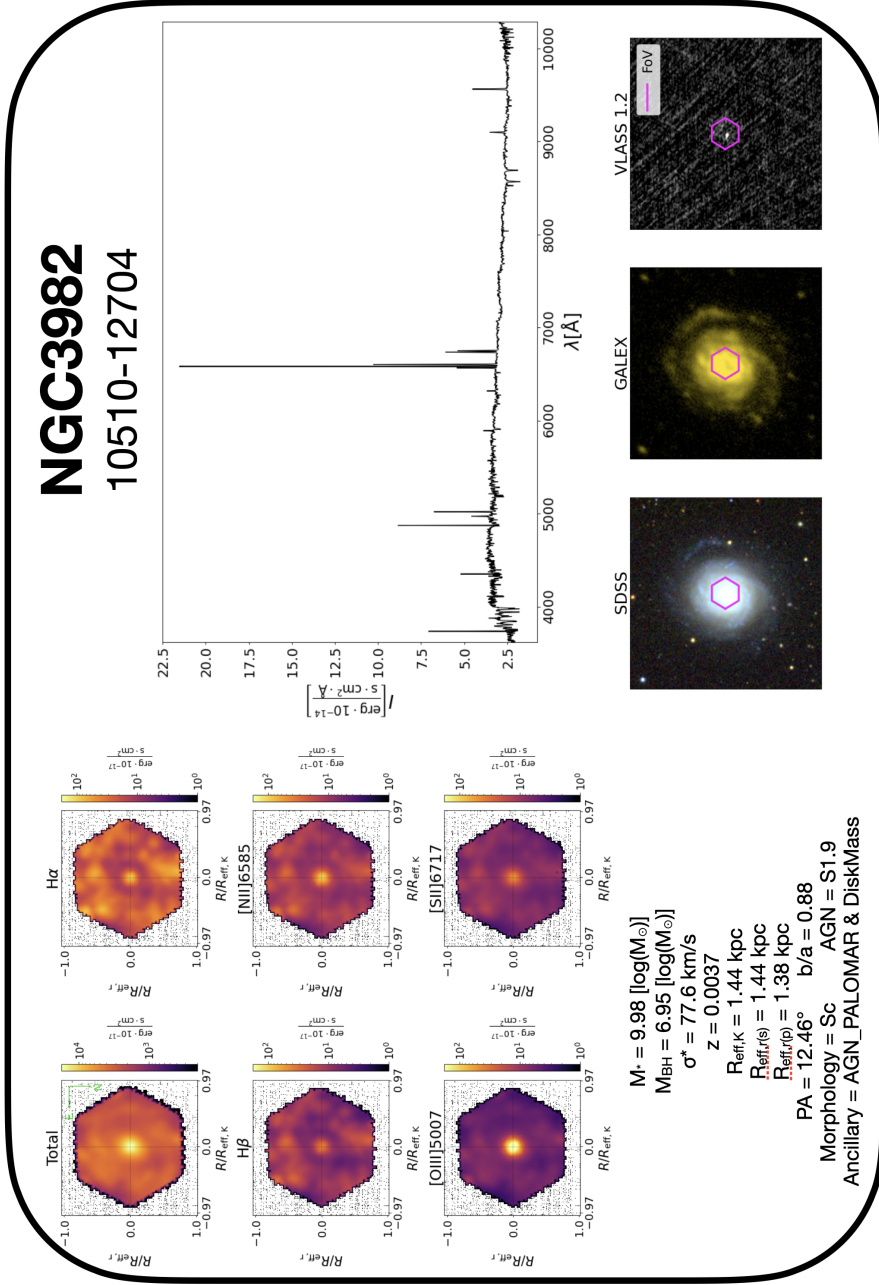Figure 2.8: Summary of **NGC2960**. The description is similar to Figure 2.3
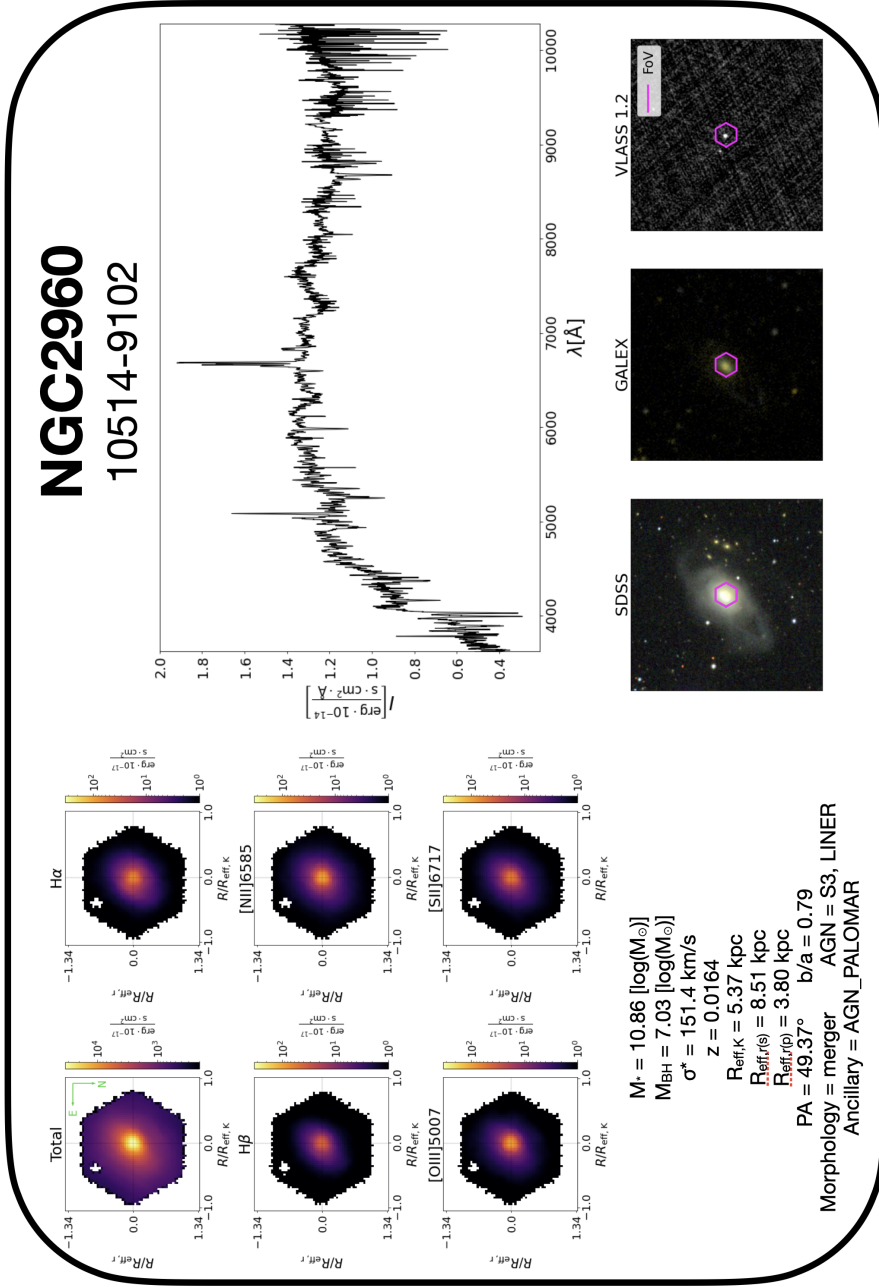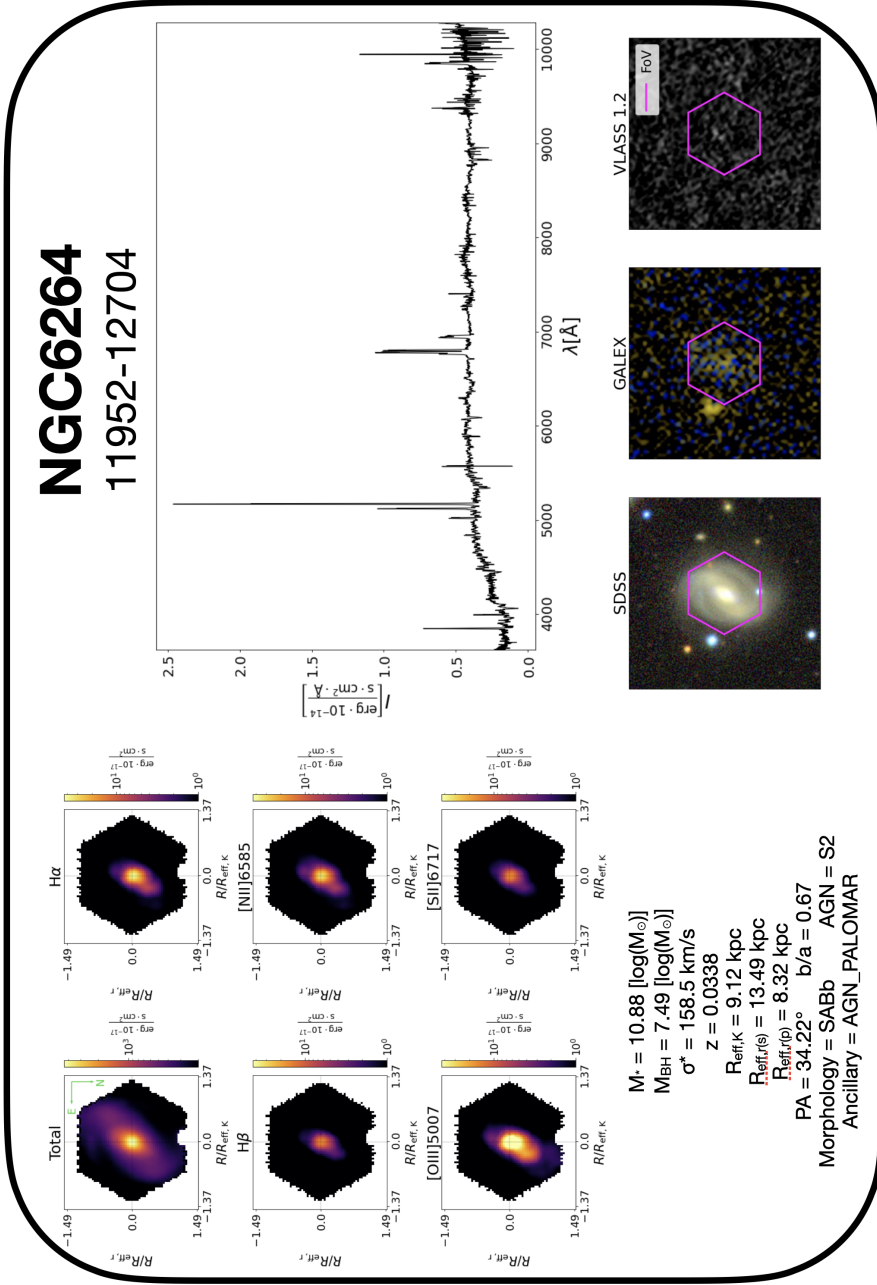
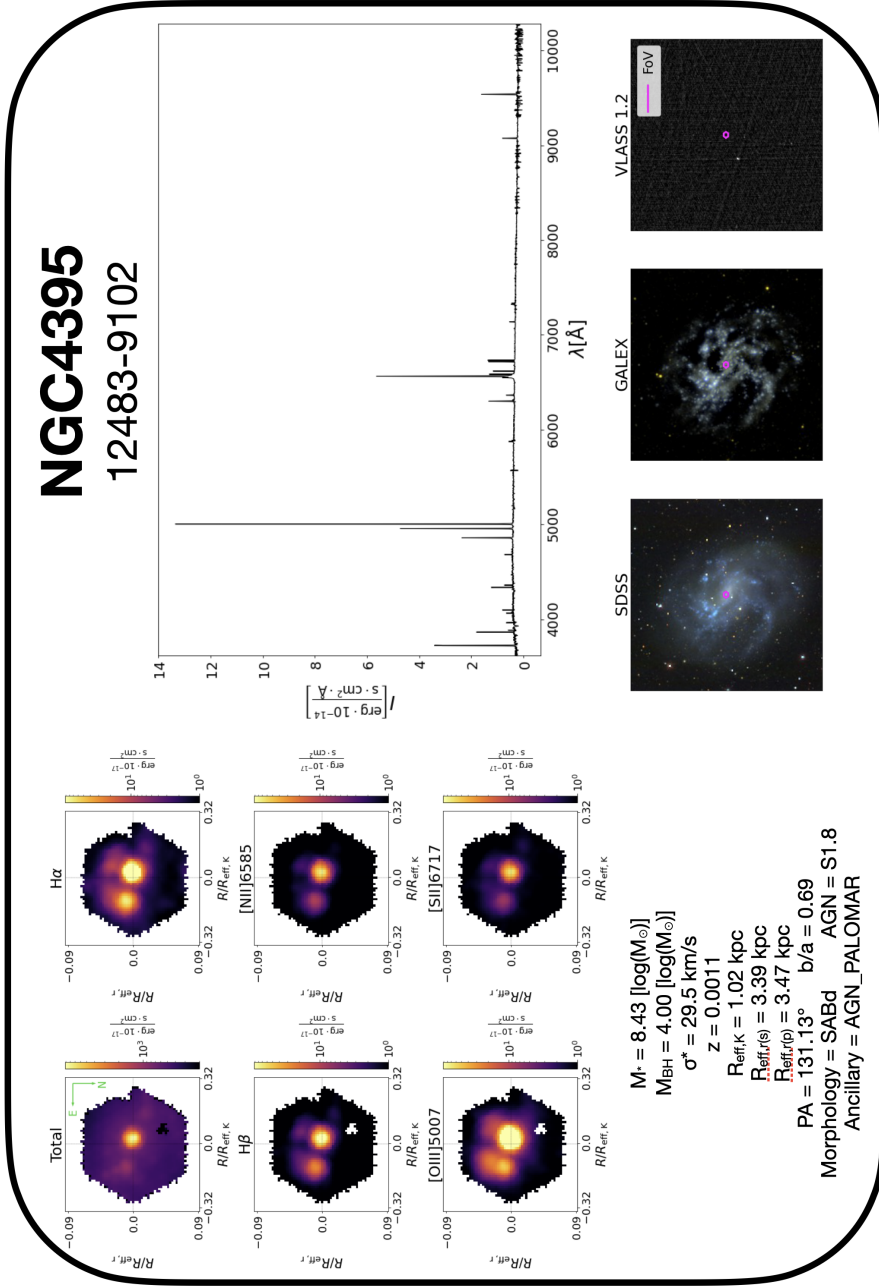Figure 2.9: Summary of **NGC6264**. The description is similar to Figure 2.3

Figure 2.10: Summary of **NGC4395**. The description is similar to Figure 2.3

Finally, it is important to remark some particular characteristics of the galaxies in our sample:

- Mrk290 has been classified as an Ultrafast X-ray outflow (UFO, Tombesi *et al.*, 2010; Kriss *et al.*, 2018; Igo *et al.*, 2020) with kinematic effects visible in the [OIII]5007 line profile (Sexton *et al.*, 2021, see also Weedman, 1973; Kaiser *et al.*, 2006; Zhang *et al.*, 2011, 2015).

- ARP151 is identified as Zw026 in the "Catalogue of selected compact galaxies and of post-eruptive galaxies" (Zwicky & Zwicky, 1971)

- NGC3982 and NGC4395 have been identified as members of a nearby group of galaxies (see Turner & Gott, 1976; Huchra & Geller, 1982; Geller & Huchra, 1983; Fouque *et al.*, 1992; Garcia, 1993; Mahtessian, 1998). Meanwhile NGC6264 has been identified as a member of a nearby poor cluster of galaxies (WBL, White *et al.*, 1999), and NGC6086 is a member of an Abell Brightest Cluster of Galaxies (BCGs de Vaucouleurs *et al.*, 1976; Hoessel *et al.*, 1980; Postman & Lauer, 1995; McConnell *et al.*, 2011).

2.3   Photometry

For this work, we used the azimuthally-averaged radial surface brightness profile reported as the average surface brightness in a series of annuli for the seven-bands *FUV, NUV, u, g, r, i* and *z*, where *FUV* and *NUV* were taken from GALEX (Martin *et al.*, 2005) and *ugriz* from the SDSS photometric data. These are tabulated in the NSA catalog as PROFMEAN together with their inverse variance PROFMEAN_IVAR (Blanton *et al.*, 2017), using the same profile apertures as the standards SDSS imaging pipeline; there are up to 15 annuli averaged profile bins in the NSA, indicated by NPROF, from 0.23 to 263.00 arcsec that are in principle available for each galaxy.[9]

The mean surface brightness (μ) of the PROFMEAN are reported in units of nanomaggies[10] per square arcsec. The galactic extinction (Schlegel *et al.*,

---

[9]See more details about the related outputs of the SDSS's photometry pipelines and some useful considerations and descriptions about various measures of magnitudes in: `https://www.sdss4.org/dr16/algorithms/magnitudes`. For details of the Photo pipeline processing see section 4.4 of Stoughton *et al.* (2002). The photometric flux calibration is also detailed in `https://www.sdss4.org/dr16/algorithms/fluxcal/`

[10]A maggie is a convenient lineal unit of the flux f of a source relative to a standard source f_0, related to the Pogson magnitude m by the following equation:

$$m = [22.5\text{mag}] - 2.5\log_{10}(f) \tag{2.3}$$

1998) and the k-correction (Blanton & Roweis, 2007) are not applied to the magnitudes of the PROFMEAN, but they are computed in the NSA catalog.

Chapter 3

Methodology

In this chapter we describe the methodology that we used to infer the parameter space of the stellar population in our sample (see Section 2.2). In Section 3.1, we describe the generalities about the Stellar Population Synthesis (SPS) models and how they are used to constrain the space parameter of the galaxies. In Section 3.2, we describe the Spectral Energy Distribution (SED) fitting library "Bayesian Analysis of Galaxies for Physical Inference and Parameter EStimation" (BAGPIPES) (Carnall *et al.*, 2018, 2019a,b) that was used in this work. We also describe the Star Formation History (SFH), the IMF, and the priors used over the SPS model space parameter to constrain the properties of the galaxy stellar population. There, it is also described the model that we developed for the emission lines due the presence of an AGN. Finally, in subsection 3.2.5 we describe the methodology used for the complementary photometric analysis.

3.1 SED Fitting Libraries

Most of the information that we have from the galaxies comes from observing the electromagnetic radiation emitted by the contribution of stars of different masses, ages and metallicities. Fortunately, our theory on stellar evolution is very well established so we can use it to compute different properties of the galaxies by studying their SED via their SPS modeling. Indeed, if we fix the IMF, the SED of a galaxy encodes information about the SFH, chemical enrichment and the dust properties of the system. Actually these properties, derived from the SEDs have provided the basis for our modern understanding about galaxy formation and evolution (see, for example, Panter *et al.*, 2004; Conroy, 2013 and Sánchez *et al.*, 2022 for a recent review).

3.1.1   The Stellar Population Synthesis Models

The main goal of the SPS modelling is to infer the physical properties of the galaxies from their observed SEDs. The first attempts to understand the electromagnetic radiation in the visible and the Near Infrared (*NIR*) were approached by a combination of local stars representing different segments of the H-R diagram to synthesize good-fitting models for the nearby galaxies M31, M32, and M81 (Spinrad & Taylor, 1971, see also, Faber, 1972; Tinsley, 1972).

However, over the time, more sophisticated versions of this technique have emerged. Particularly in the last years the progress in understanding stellar evolution theories and the recent development of new SPS fitting models have laid the foundation for what would become the standard approach in the SED modeling (Faber *et al.*, 1977; Tinsley, 1980; Frogel, 1988; Maraston, 1998; Walcher *et al.*, 2011; Conroy, 2013; Leja *et al.*, 2017; Carnall *et al.*, 2018; Sánchez *et al.*, 2022, and many more references therein). Figure 3.1 summarizes the standard methodology to follow in the SPS technique.

Figure 3.1 shows that once an IMF (e.g., Salpeter, 1955; Scalo, 1986; Kroupa & Boily, 2002; Chabrier, 2003) is chosen, and when the stellar evolution, the isochrone models (Schaller *et al.*, 1992; Bertelli *et al.*, 1994; Pietrinferni *et al.*, 2004)[1] and a set of spectral libraries are fixed; one could sample a coeval collection of simple stellar populations through a star formation and a chemical enrichment histories, which combined with dust attenuation (A_V; e.g., Cardelli *et al.*, 1989; Charlot & Fall, 2000; Calzetti, 2001) and emission laws, totally define the SED of a galaxy (a comparison of different SPS models can be seen in Conroy & Gunn, 2010).

Finally, there are different ways to find the best fit parameters for the modelling of the SED of the galaxies; among the most popular are the frequentist methods, like χ^2-minimisation (e.g., Sánchez *et al.*, 2018) and the Bayesian methods (e.g., Leja *et al.*, 2017; Carnall *et al.*, 2018).

---

[1]Isochrones are theoretical models used to depict the evolution of SPs over time. They are constructed based on stellar evolution theory, which describes how stars change and evolve throughout their lifetimes. By modeling the evolutionary tracks of stars with different masses, isochrones show how the properties of stars, such as luminosity and color, change as they age.
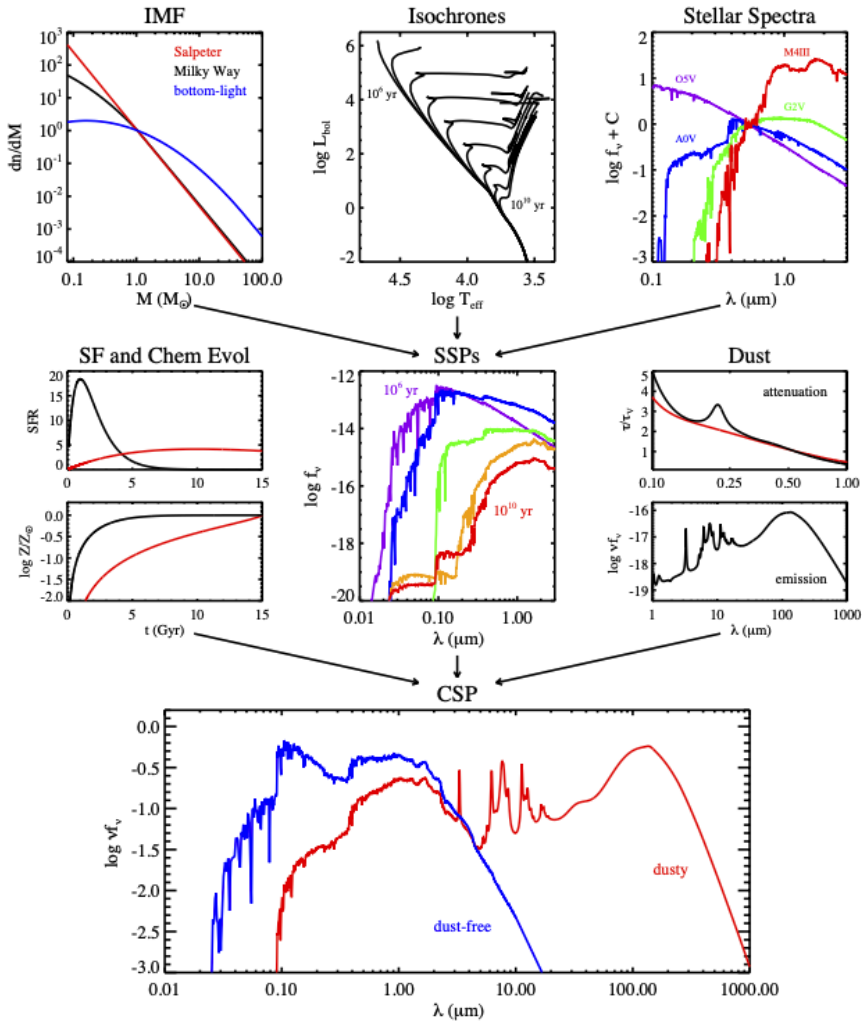
Figure 3.1: Overview of the SPS technique. The upper panels highlight the ingredients necessary for constructing a Simple Stellar Population (SSP): an IMF, isochrones for a range of ages and metallicities, and stellar spectra spanning a range of T_{eff}, L_{bol} and metallicity (Z_*). The middle panels highlight the ingredients necessary for constructing a Composite Stellar Population (CSP): a SFH and chemical evolution, SSPs and a model for dust attenuation and emission. The bottom panel shows the final CSPs both before and after a dust model is applied. Figure from Conroy (2013).

3.1.2   Bayesian Methodology

Bayesian methodology is an approach to statistical inference and modeling that utilizes Bayes' theorem to update our beliefs about a parameter or hypothesis based on new evidence or data. The goal is to estimate the probability distribution of the parameter space given the observed data.

The steps involved in Bayesian parameter fitting are the following:

- We start by defining a prior on the belief about the distribution of the parameters. This belief is represented by probability distributions called the prior distribution. It incorporates any existing knowledge, assumptions, or beliefs about the parameters.

- Next, based on the hypothesis formulated for our analysis, we define a likelihood function that represents the probability of observing the data given a specific value of the parameters. It quantifies how well the parameter space explains the observed data. We also define an evidence which quantifies the probability that the data fits the hypothesis.

- Using the *Bayes' theorem*, we combine the prior distribution and the likelihood function to obtain the posterior distribution, which represents our updated belief about the parameters after taking into account the observed data. It is proportional to the product of the prior distribution and the likelihood function (see Equation 3.1).

$$\text{posterior} = \text{likelihood} \times \frac{\text{prior}}{\text{evidence}} \qquad (3.1)$$

- Once we have the posterior distribution, we can perform various types of inference. For example, we can estimate the most likely value of the parameter and compute credible intervals to quantify uncertainty by using the percentiles of the posterior distribution.

- Finally, Bayesian methodology allows for iterative updating of the posterior distribution as more data becomes available. This means that we can incorporate new evidence and update our beliefs about the parameter multiple times, refining our estimates with each iteration.

Overall, Bayesian parameter fitting provides a probabilistic framework for estimating parameters that takes into account both prior knowledge and observed data, resulting in more nuanced and flexible inference compared to traditional frequentist methods (like χ^2 minimization). In this work we use a Bayesian method because of its robustness in finding the space parameter of a model. Next, we describe Bagpipes.

3.2   Fitting Procedure With BAGPIPES

BAGPIPES is one of the state of the art Python codes for modelling galaxy spectra to fit spectroscopic and photometric observations. BAGPIPES is described in detail in Carnall *et al.* (2018, this paper focused on photometric data) and in Carnall *et al.* (2019b, while this one is focused on describing the application to spectroscopic samples).[2]

BAGPIPES is a code developed in Python with the goal of fitting the SED of a galaxy based on spectroscopic and/or photometric data using the nested sampling algorithm[3] of Skilling (2006) for the Bayesian inference of the space parameter. This nested sampling algorithm is implemented in BAGPIPES using MULTINEST (Feroz & Hobson, 2008; Feroz *et al.*, 2009, 2019), by the PYMULTI-NEST interface (Buchner *et al.*, 2014).

BAGPIPES is a very flexible and versatile code as it can use different parts of the spectrum, SFHs[4], chemical enrichment models, nebular emission, and dust absorption, remission and attenuation laws. In BAGPIPES the SPS is not implemented directly, instead the code is designed to accept pre-defined SPS models in the form of grids of SSP models of different ages across a range of metallicities. The SPS models currently implemented in BAGPIPES are the 2016 version of the Bruzual & Charlot (2003) models, which computes the spectral evolution of stellar populations at ages from 0.1 to 20 Gyr at a resolution of 3 Å across the whole wavelength range from 3200 to 9500 Å for a wide range of metallicities (considering a grid of 0.005, 0.02, 0.2, 0.4, 1.0, 2.5, 5.0 solar metallicities) and uses the Medium-resolution Isaac Newton Telescope library of empirical spectra (MILES; Falcón-Barroso *et al.*, 2011) in the UV-optical spectral region.[5] Next, we describe in more detail the implementation we are using to fit the spectra of each aperture for every galaxy in our sample.

In this work, all the spectral analyses are carried out within the observed wavelength interval from 3800 to 7000 Å, following Lacerda *et al.* (2022) and

---

[2]BAGPIPES can be found here: `https://github.com/ACCarnall/Bagpipes`. And the documentation is here: `https://Bagpipes.readthedocs.io/en/latest/index.html`.

[3]Nested sampling is a method used to estimate the marginal likelihood of a statistical model and obtain posterior distributions. It involves creating nested subsets of the parameter space, exploring regions of higher likelihood and gradually moving towards lower likelihood. By tracking the likelihood levels, it estimates the evidence by sampling from the prior and calculating the associated prior mass. It efficiently handles complex parameter spaces, generates posterior samples and facilitates model comparison, aiding in parameter estimation and uncertainty quantification, however, it can be computationally intensive, especially for high-dimensional models or expensive likelihood evaluations (this problem can be solved by techniques like parallelization).

[4]Which may include parametric as well as non-parametric models.

[5]When a set of SPS models is loaded by BAGPIPES, the models are resampled in age (using a weighted summation method) onto a grid of ages, a_i from $\log(a_i/\text{Gyr}) = 6.0$ to 10.2 with uniform width, having a default spacing of 0.1 dex.

Sánchez *et al.* (2022). Next, we describe all the ingredients that we input into
BAGPIPES.

3.2.1   Star Formation History

Traditionally, the SFH has been described by using the parametric models men-
tioned in Section 1.2, even though its stochastic nature (e.g., Caplar & Tac-
chella, 2019; Tacchella *et al.*, 2020; Iyer *et al.*, 2020). Previous authors (e.g.,
Simha *et al.*, 2014; Diemer *et al.*, 2017) have shown that those models repre-
sent a poor match to the simulated universe. For this reason, in this work we
make use of the Double Power-Law (DPL) function proposed by Behroozi *et al.*
(2013), as a more sophisticated model for the SFH which has been shown repro-
duces the SFHs from semi-empirical models and from the simulated universe
(Diemer *et al.*, 2017). Explicitly our SFH law has the following shape:

$$SFR(t) \propto \left[\left(\frac{t}{\tau_{\mathrm{dpl}}} \right)^{\alpha_{\mathrm{dpl}}} + \left(\frac{t}{\tau_{\mathrm{dpl}}} \right)^{-\beta_{\mathrm{dpl}}} \right]^{-1} \tag{3.2}$$

where τ_{dpl} is the time, measured since the Big Bang (BB), at maximum of the
SFR and the slopes β_{dpl} and α_{dpl} determine the decreasing and raising of the
SFH at later and earlier times respectively. This SFH law is normalized through
the total stellar mass formed across the overall history of the galaxy, $M_{*,\mathrm{formed}}$.[6]

3.2.2   Dust Attenuation

Dust in the interstellar medium (ISM), plays an important role in understanding
the properties of the galaxies. Not only because the light gets absorbed and
scattered but also because it encodes important parts of the evolution of the
galaxies as it originates as a product of the stellar evolution.

   The presence of young stars surrounded by dust will produce emission in
the infrared, IR. The reason for this is because hot young stars will tend to heat
the dust and the dust will produce emission as a "modified black-body" with a
peak in the IR part of the spectrum. It is typically assumed that the fraction of
light emitted by young stars that is absorbed by the dust is directly proportion-
ally to the fraction that it remitted (da Cunha *et al.*, 2008). Nonetheless, dust
also modifies the stellar continuum in the visible part (for a review see Salim &
Narayanan, 2020). While there are several models to describe the dust attenu-
ation law in the galaxies, in this work we use the one described by Cardelli *et
al.* (1989).

---

[6] $M_{*,\mathrm{formed}} > M_*$: $M_{*,\mathrm{formed}}$ considers the total stellar mass at the moment (M_*) together
with the stellar mass remnants (white dwarfs, stellar BHs, gas remnants in the ISM, etc).

3.2.3 Emission From the Ionized Gas

In addition to the properties listed above, the SED of a galaxy contains information about the mechanisms that are not part of our stellar evolution theories. Particularly, the luminosities and widths of some emission lines located in the visible region of the electromagnetic spectrum, could contain information about the components which are not directly linked to the SF of the galaxy, such as the emission lines from gaseous nebulae (diffuse, planetary, and supernovae remnants; Brinchmann *et al.*, 2004) and emission lines from the AGN.

Nebular Emission

The nebular emissions of a galaxy come from different physical sources like diffuse nebulae, planetary nebulae, H II regions and supernova remnants. Diffuse nebulae consist on clouds of dusty interstellar gas that are ionized by ultraviolet radiation from the massive hot stars near or within them. Planetary nebulae consist of ejected mass from dying stars on their last stages to become a white dwarf. H II regions allow us to probe the evolution of the elements and the SFH of the far reaches of our own galaxy and of distant galaxies. Supernova remnants consist on hot ejected material from exploding massive stars and allow us to observe the material from their burned-out deep interiors.

Gaseous nebulae give emission-line spectra dominated, in the optical region of the SED, by forbidden lines of ions of common elements, such as [OIII]4959,5007. In addition the permitted lines of hydrogen (Hα, Hβ, Hγ, and so on) are characteristic features of every nebular spectrum. In the other hand, gaseous nebulae have weak continuous spectra.

The inclusion of nebular emission in the modelling of the SED of the galaxies is so complex that a further discussion is well beyond the scope of this work (see more in Osterbrock & Ferland, 2006; Mo *et al.*, 2010). Note, however, that it is well known that nebular emission is more important in low-metallicity and star forming galaxies (see e.g., Conroy, 2013). In this thesis we include the emission lines the way it is implemented in BAGPIPES via the CLOUDY code (Ferland *et al.*, 2017). The basic physics in which this code is based, it is described in Osterbrock & Ferland (2006). Briefly, BAGPIPES has a preloaded grid of emission lines models based on different degrees of the ionisation of the ISM, which are denoted by the ionisation parameter U.

Active Galactic Nuclei

In particular, the characteristics of the optical spectrum are useful to identify a particular type of AGN, the Seyferts: these usually present prominent emission lines, corresponding to radiation from ionized gas, some of the most distinctive are Hα, Hβ, [NII]6548,6583, [SII]6717,6731 and [OIII]4959,5007. While it is

difficult to model the emission lines from the AGN, their contribution to the
SED of the galaxy are well known and even well characterized. In this section
we discuss our modelling for both the continuum and the emission lines of the
SED.

Figure 3.2 shows typical examples of the optical spectra of Seyfert AGNs,
where the contrast between Type 1 and Type 2 can be seen: both types show
narrow emission lines from the NLR, but the main spectroscopic difference
(among others) is that Type 1 AGNs also have the presence of broad com-
ponents in some of these emission lines, coming from the BLR, with Hα and
Hβ usually being the most prominent ones (Khachikian & Weedman, 1974;
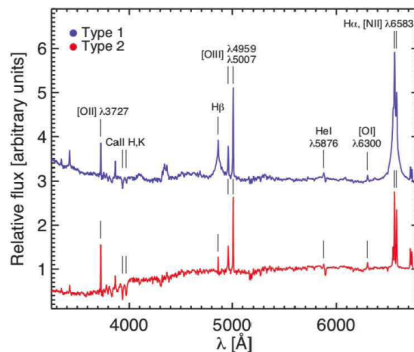Lawrence, 1987).

Figure 3.2: Visible spectra examples of Type 1 (blue) and Type 2 (red) AGNs from
the SDSS. The main differences are the presence of permitted broad emission lines and
a bluer nuclear continuum in Type 1 AGNs. Figure from DiPompeo *et al.* (2018).

The dynamical properties of these broad Balmer emission lines allow not
only the classification of the AGN, but also to obtain single epoch inferences of
M_{BH}, through Greene & Ho (2005)'s method, using their luminosities as well
as their FWHMs. In consequence, if one is seeking to obtain robust inferences
of M_{BH} through this indirect method, it is necessary to have correctly modeled
spectroscopic fits of the AGN's emission lines.[7]

---

[7]Inferences of M_{BH} can be obtained by using Equations 3.3 and 3.4, from the luminosities
and the FWHMs of Hα and Hβ broad lines:

$$M_{\mathrm{BH}} = \left(2.0^{+0.4}_{-0.3}\right) \times 10^6 \left(\frac{L_{\mathrm{H}\alpha}}{10^{42}\frac{\mathrm{erg}}{\mathrm{s}}}\right)^{0.55\pm0.02} \left(\frac{FWHM_{\mathrm{H}\alpha}}{10^3\frac{\mathrm{km}}{\mathrm{s}}}\right)^{2.06\pm0.06} \mathrm{M}_\odot \qquad (3.3)$$

$$M_{\mathrm{BH}} = (3.6 \pm 0.2) \times 10^6 \left(\frac{L_{\mathrm{H}\beta}}{10^{42}\frac{\mathrm{erg}}{\mathrm{s}}}\right)^{0.56\pm0.02} \left(\frac{FWHM_{\mathrm{H}\beta}}{10^3\frac{\mathrm{km}}{\mathrm{s}}}\right)^{2} \mathrm{M}_\odot \qquad (3.4)$$

If some of the broad lines are described by more than one Gaussian component, it is considered
the luminosity and the FWHM of the sum of all the broad components.

It is important to mention that currently for SED fitting tools based on SPS, it is not common to consider the contribution of the AGN. Instead, these type of galaxies are usually excluded from most SPS studies, discriminating by crossmatching with databases of known AGNs (like the one of Véron-Cetty & Véron, 2006) or through their location in diagnostic diagrams such as the "Baldwin, Phillips & Terlevich" (BPT, Baldwin *et al.*, 1981), the "WHAN" diagram (Cid Fernandes *et al.*, 2010, 2011) or other similar diagnostic diagrams (see Veilleux *et al.*, 1995; Kewley *et al.*, 2001, 2006; Kauffmann *et al.*, 2003; Schawinski *et al.*, 2007). These diagrams represent the first order of identification and/or classification of AGNs. A more detailed study on AGNs would be by separating their spectral contribution to the SED of their host galaxy.

A correct model for the AGN spectral contribution into the stellar SED, requires a very careful analysis, such as the one we are proposing here. This must be done with a model composed of a much larger number of free parameters than the usual SPS models, describing the fundamental properties of the SPS together with the AGN ionized gas emission lines and the continuum emitted from the accretion disk (whose contribution is quite significant in the visible region of the electromagnetic spectrum of some galaxies).

Fortunately, the overall SED for the continuum of an AGN, at least in the optical region where we are more interested, can be described by a power law $F_\nu \propto \nu^{\alpha_{AGN}}$. In this work we assume this form when it is necessary.

In this work, we exploit the Bayesian nature of BAGPIPES by modelling at the same time the stellar contribution from the stellar continuum, including nebular emissions and dust attenuation, and the contribution from the AGN. We assume the following emission lines from the NLR of the AGN:

1. Hα, Hβ, Hγ, Hδ,

2. [O$_{III}$]4363,4959,5007,

3. [N$_{II}$]6548,6583,

4. [S$_{II}$]4072,6717,6731,

5. [O$_I$]6300,6365.

From the BLR of the AGN we only assume the contribution of the ionized hydrogen lines Hα, Hβ, Hγ and Hδ, composed by one or two broad components, when necessary.

3.2.4   Priors of the Spectral Fitting

In this Section we describe the free parameters and priors for our spectral modelling. Notice that the number of parameters depends on the very nature of

each galaxy. In other words, it depends on how many components are necessary to model the spectrum of a galaxy.

The first part of our analysis consist on masking certain regions of the spectrum from the official reduced MaNGA datacubes (Law *et al.*, 2016). These regions are the ones affected by:

1. Strong and variable night sky emission line residuals;

2. Regions affected by instrumental signatures, whose effect was not completely removed during the data reduction process; and

3. Regions affected by telluric absorptions, not completely corrected during the flux calibration process, like 5550-5610 Å and 5800-6080 Å regions.

The masked regions for each galaxy are violet-shaded in the spectral fitting figures of the Results (see Chapter 4). Notice that this is a common practice and many pipelines have done something similar (e.g., Pipe3D, Sánchez *et al.*, 2016a,b, 2022).

The second part of our analysis is to perform a first analysis of the SED by masking all the emission lines and fitting only the stellar continuum. This step is important as it helps us to decide whether the galaxy has the contribution from other sources. We use these results as the priors for our next fit, in case it is necessary. The free parameters to fit in each galaxy are:

- α_{dpl} and β_{dpl}: The falling and the rising slope of the DPL-SFH (see Equation 3.2), to which we assign a logarithmic prior between 0.001 and 100.

- τ: The peak time of the DPL, to which we assign an uniform prior between 0.5 Gyr and the age of the universe at the redshift of the galaxy, $t_U(z_{\mathrm{obs}})[\mathrm{Gyr}]$.

- $M_{*,\mathrm{formed}}$: The total stellar mass formed, to which we assign an uniform prior of $\log_{10}(M_{*,\mathrm{formed}})$ between 6.0 to 14.0 $\log(\mathrm{M}_\odot)$, spanning the entire mass range of galaxies in MaNGA.

- Z_*: The stellar metallicity to which we assign a logarithmic uniform prior over the range $0.02 < Z_*/\mathrm{Z}_\odot < 2.5$, similar as Carnall *et al.* (2019b) does (and more free than the logarithmic prior over the range $0.2 < Z_*/\mathrm{Z}_\odot < 2.0$ of Carnall *et al.*, 2019a, or the uniform prior over the range of $0.2 < Z_*/\mathrm{Z}_\odot < 2.0$ of Carnall *et al.*, 2018)[8].;

- A_V: for Cardelli *et al.* (1989) dust attenuation law, to which we assign a uniform prior between 0.0 and 1.5 magnitudes.

---

[8]Notice that Carnall *et al.* (2019b) is the reference recommended by the author of the code, for spectroscopic fitting.

Once this first spectral analysis is done, we decide which galaxies require to be fitted again, but considering the contribution from the AGN, taking into account the emission lines from the NLR, the BLR and/or the AGN continuum. If a galaxy requires another fit, according to the observed residuals and the χ^2 (as a guideline of the merit of the fitting) of this first SED fitting results, we make the decision whether the galaxy will be fitted by adding nebular emissions only or if it is necessary to include a model for the AGN, based on the morphology of the emission lines and in its known AGN classification (Véron-Cetty & Véron, 2006). Notice that the best fitting models and their distributions from the previous step are used as new starting points and priors for our more detailed fitting model.

In the case that the galaxy host an AGN we use the following free parameters to fit each component:

- <u>NLR</u>: Each *narrow* emission line, Hα, Hβ, Hγ, Hδ, [O III]4363,4959,5007, [N II]6548,6583, [S II]4072,6717,6731 and [O I]6300,6365, are proportional to single Gaussians[9]. All of them were constrained to have the same width c, and their centroids are parameterized by the rest frame quantity b. The maximum intensities, a, of each lines are free parameters, but under the following constrains:
  $a_{[\text{O III}]5969} = \frac{1}{3} a_{[\text{O III}]5007}$, and $a_{[\text{N II}]6548} = \frac{1}{3} a_{[\text{N II}]6583}$.

- <u>BLR</u>: The Balmer emission lines, Hα, Hβ, Hγ and Hδ, are sometimes not well described by only one *narrow* line from the NLR. There are cases where some of this lines require to also model a *broad* line component coming from the BLR, and sometimes even a third *very broad* component, to successfully describe them. Each of these broad emission lines are described by the three free parameters of the Gaussian profile (a, b, c).

- <u>AGN accretion disk continuum</u>: The blue region of some AGNs spectrum is typically dominated by the AGN nuclear contribution. Sometimes it is necessary to consider a continuum described by a power law[10]. In this case we defined it to contribute over the entire analysed wavelength range, with $\lambda_0 = 3800$ Å, resulting in two free parameters: A_{AGN} and α_{AGN}.

---

[9]Explicitly, the form of the Gaussian function we are using is:

$$G(a, b, c; \lambda) = a \cdot \exp\left(\frac{(b - \lambda)^2}{2c^2}\right) \tag{3.5}$$

[10]The definition of a power law is Equation 3.6:

$$I(A_{\text{AGN}}, \alpha_{\text{AGN}}, \lambda_0; \lambda) = A_{\text{AGN}} \cdot \left(\frac{\lambda}{\lambda_0}\right)^{-\alpha_{\text{AGN}}} \tag{3.6}$$

3.2.5 Photometric Analysis

After carrying out the spectroscopic analysis described above, we decided to complement it by making a photometric analysis for the 8 galaxies of the sample, using the photometric data of the NSA described in Section 2.3. Another motivation for doing this exercise is that in most of the cases the seven-band surface brightness tabulated in the NSA catalog extend to radii beyond the FoV of MaNGA. Thus in order to understand not only how the central part of the galaxy formed but the stellar population in outer radii, the SED fitting results from the surface brightness will be key and complementary. This analysis is only a guideline to have a better understanding of the results obtained through the IFS analysis.

As we are interested in using only the cumulative profiles, particularly in the maximum aperture of the photometry, we did not interpolate the cumulative profile, following the method described in Stoughton *et al.* (2002). In order to get the cumulative profiles to analyze every filter, we simply integrated the μ within each aperture, then we converted them to Pogson magnitudes, and then considering the D_L, we got the absolute magnitudes and the integrated luminosities (L). To estimate the errors of the cumulative profiles (σ_L) we first calculate the uncertainty of the fluxes of each aperture, given by PROFMEAN_IVAR$^{-1/2}$ and then, similarly to the fluxes, we integrated them within each aperture, converted to Pogson magnitudes and finally to absolute magnitudes and to luminosity units. Corrections to the absolute magnitudes for galactic extinction and k-correction are performed to the final cumulative profiles which will are in units of $\text{erg} \cdot \text{s}^{-1} \cdot \text{cm}^{-2} \cdot \text{Å}^{-1}$, as BAGPIPES requires.

The mean surface brightness and the cumulative luminosity profiles of our sample are shown in Figures 3.3,3.4,3.5 and 3.6. Apertures where $\sigma_L^2 \geq L$ in three or more filters, were discarded from the analysis (this happens most of the time at the largest apertures).

We use BAGPIPES in order to infer the properties and evolution of the stellar population as a function of radius of the cumulative profiles in which there is available information in our data. Considering that the broad-band photometric data does not provide information about the emission lines from the NLR nor the BLR of the AGN, these components are not modeled in the SED broad-band fitting analysis. The priors of the SED broad-band fitting include the parameters of the SFH law defined by Equation 3.2 as well as the $M_{*,\text{formed}}$, the dust A_V described by Cardelli *et al.* (1989) and the ionisation parameter U of the nebular emission, and we use the priors for Z_* as in the IFS analysis. We did not performed any analysis for Mrk290 and ARP151 because these galaxies are heavily contaminated by their central AGN.
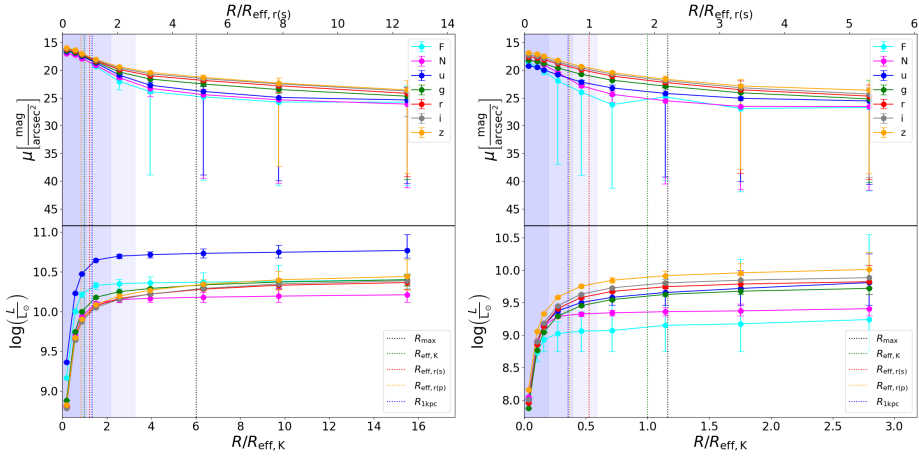
Figure 3.3: Surface brightness profiles of Mrk290 (left) and ARP151 (right) for *FUV* (cyan line), *NUV* (magenta line), u (blue line), g (green line), r (red line), i (gray line) and z (yellow line) filters. The top panels show the mean surface brightness while the bottom panels show the cumulative luminosity. Some apertures of interest in the IFS analysis are represented with a vertical dotted line by a different color (black: R_{max}, green: $R_{\mathrm{eff},K}$, red: $R_{\mathrm{eff},\mathrm{r(s)}}$, yellow: $R_{\mathrm{eff},\mathrm{r(p)}}$, blue: R_{1kpc}). The violet shaded areas represent 1PSF, 2PSF and 3PSF radius of the IFS data, distinguished by the opacity.
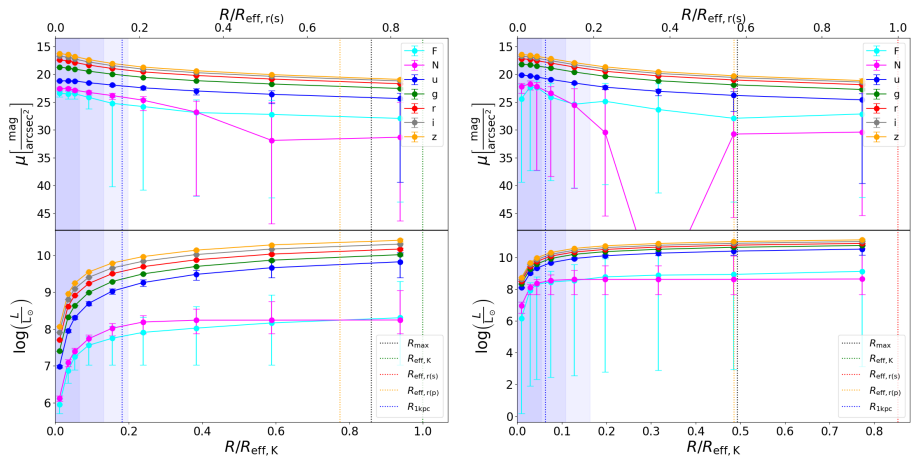

Figure 3.4: Surface brightness profiles of NGC1194 (left) and NGC6086 (right). The description is similar to Figure 3.3.
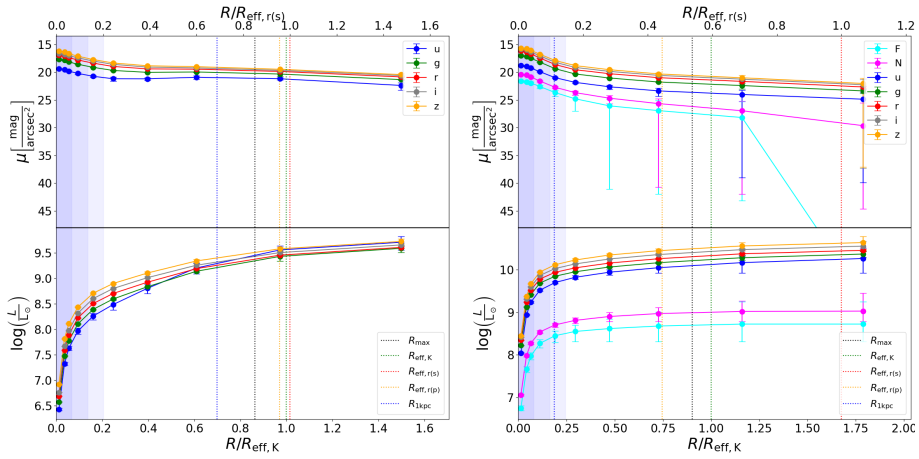
Figure 3.5: Surface brightness profiles of NGC3982 (left) and NGC2960 (right). The description is similar to Figure 3.3.
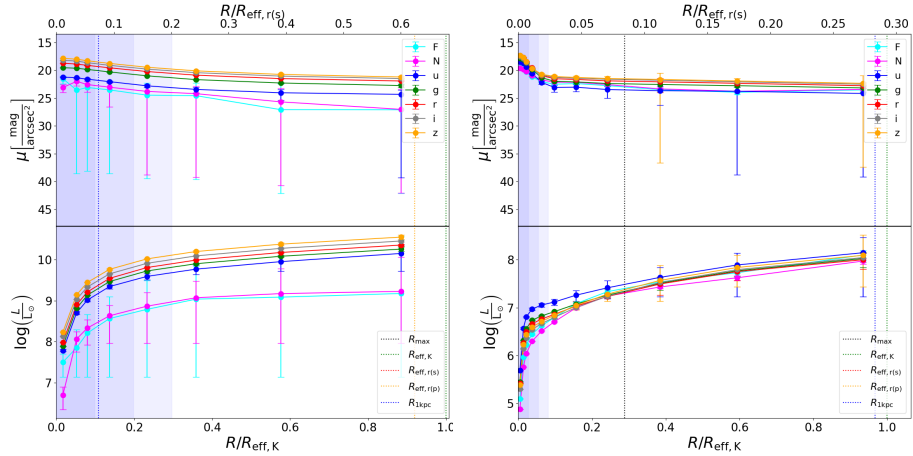

Figure 3.6: Surface brightness profiles of NGC6264 (left) and NGC4395 (right). The description is similar to Figure 3.3.

Chapter 4

Results

In this Chapter we present the results obtained for the spectral fitting at different radii for the IFS data of the galaxies in our sample, together with the results obtained by the broad-band SED fitting model. Our main goal for this section is to infer the stellar properties of the galaxies in order to understand the co-evolution between supermassive BHs and galaxies. Because of the *Bayesian* nature of BAGPIPES, the results of the spectral fitting (the intensities for each wavelength), as well as the physical parameters, are originally given in the form of probability distributions (see the 2D-posterior probability distribution function maps of the physical parameters in Appendix A); we report the quantities obtained by considering the 50th, 16th and 86th percentiles for each probability distribution, to get the mean values as well as the uncertainties.

In order to integrate the spectra at each aperture we use the axis ratio (b/a) and the pitch angle (PA) reported for the r-band in the NSA Catalogue. To facilitate our analysis we have defined 5 different spectroscopic apertures, characterized by their semi-major axes, for each galaxy in our sample, which are the following:

- **Maximum aperture** (R_{max}): It is defined as the maximum ellipsoid that fits within the MaNGA FoV. Notice that by construction this aperture maximizes the information of the MaNGA data cubes without introducing border effects. In order to cover a wide range of radial apertures in our analysis, we also considered the elliptical apertures corresponding to $0.25R_{\mathrm{max}}$, $0.5R_{\mathrm{max}}$ and $0.75R_{\mathrm{max}}$.

- **At 1 kpc** (R_{1kpc}): This aperture is measured within 1 kpc. In previous works this aperture has been used as a proxy to measure properties of the SMBHs since, the larger the SMBH is, the larger the value of the mass density within the aperture of 1 kpc $(M_{*,1})$ will be. In addition, the quantity $\Sigma_1 = M_{*,1}/\pi$ is a good proxy for dividing galaxy's samples into star forming and quiescent galaxies (Fang *et al.*, 2013).

- **Non parametric semi-major axis half light radius in the K-band** $(R_{\mathrm{eff},K})$: This is the aperture reported by van den Bosch (2016), which is measured on the the growth-curve at the radius by which the half of the light has been reached in the K-band.

- **Sérsic semi-major axis half light radius in the r-band** $(R_{\mathrm{eff,r(s)}})$: This is the aperture of the half light radius from the Sérsic fit in the r-band, taken from the NSA Catalogue.

- **Petrosian semi-major axis half light radius in the r-band** $(R_{\mathrm{eff,r(p)}})$: This is the aperture of the half light radius from the definition of an elliptical Petrosian magnitude in the r-band, taken from the NSA Catalogue.

Next, for each galaxy we present our best spectral fitting model to the IFS data (for simplicity and for the sake of the space, we only show here the results for $R_{\max}$ aperture, while in Appendix A we present the results for all the apertures defined above). Along with the fits, we also present the corresponding galaxy SF and mass assembly histories[1] for each aperture, together with the radial profiles of the stellar properties. If the presence of an AGN is detected, we also include a discussion on the radial dependence of the best fitting models for the emission lines and their locations on the BPT and WHAN diagrams.

For the broad-band fit to the photometric data, as described in Section 3.2.5, we make use of the seven-band (*FUV, NUV, u, g, r, i* and *z*) azimuthally-averaged radial surface brightness tabulated in the NSA catalog. We report the results of the SED fitting to the cumulative profiles for the seven photometric bands, with the main goal of testing and complementing the results of the stellar population properties, as a function of radius, obtained with the IFS analysis. In addition, we use the $g - i$ color profile and the mass-to-light ratios dependent on color to compute a photometric M_* and SFR[2]. It is important

---

[1]These evolution histories were obtained by an interpolation done by BAGPIPES which predicts some physical quantities at different epochs (higher redshifts). This function is a bit experimental and only works for models with a single SFH component described by the DPL. For more details see the documentation of BAGPIPES at `https://bagpipes.readthedocs.io/en/latest/`

[2]The SFR can be estimated by considering the integrated luminosity of FUV (L_{FUV}) in Equation 4.1 (Kennicutt, 1998):

$$SFR_{FUV} = \kappa \cdot L_{FUV} \tag{4.1}$$

where $\kappa = 1.701 \cdot 10^{-10} \, \frac{\mathrm{M_\odot}}{\mathrm{yr \cdot L_\odot}}$. And the M_* can be estimated by the relation described in Equation 4.2 (Taylor *et al.*, 2015):

$$\log\left(M_{*,i-band}\right) = -0.68 + 0.73(g - i) - 0.4(M_i - AB_i) \tag{4.2}$$

where M_i is the i-band absolute magnitude, and AB_i is the absolute magnitude of the sun in the i-band (obtained from `http://mips.as.arizona.edu/~cnaw/sun.html`; Willmer, 2018).

to note that the broad-band analysis is done only as a complementary guide to have a better understanding of the results of the main analysis (IFS). However it does not consider the contamination of the SED due the AGN in the broad bands, due to the complexity of describing its contribution. This means that these results might not be as robust and precise as the ones obtained by the spectral analysis.

We define that a galaxy is quenched according to the criteria used in BAG-PIPES. This criteria considers that a galaxy has quenched at a time t_{quench} since the Big Bang (BB), when the value of its $SFR(t_{quench})$, gets below the 10% of the mean SFR. In addition to that, we also consider the criteria used by (Pacifici $et~al.$, 2016) in which a galaxy is defined as quiescent when its $sSFR$ oscillates on frequency values corresponding to timescales greater than $\sim 0.4 - 0.5t_{\text{Hubble}}$, ($i.e.$ when $sSFR < 2.5H(z)$, where $H(z)$ is known as the Hubble Parameter, see more in Tacchella $et~al.$, 2016b)[3].

In the following sections (one per galaxy in our sample) we show our results, which include the spectral fitting to the IFS data and its associated SF and mass assembly histories, as well as the radial profiles of the stellar and AGN properties and the BPT and WHAN diagrams derived from the narrow lines properties. If broad components of Hα and Hβ were found, the results are followed by the inference of the M_{BH} from the single epoch method (Greene & Ho, 2005). Finally we also present a radial profile comparison between the results from the IFS analysis and the broad-band SED analysis.

For the IFS analysis we quantify the figure of merit of our fittings by using the chi-square (χ^2) estimator[4], which we emphasise that this it is only a guideline to the figure of merit to the fit. Notice that contrary to the intuition, we find that the reduced χ^2 decreases as we integrate more outer apertures. This is because the integrated error of the flux (σ) grows with aperture (we performed an uncertainty propagation error procedure by adding in quadrature the errors from all spaxels inside a given aperture), since the outer parts of the galaxies become fainter, their uncertainties increase and they become easier to fit.

In order to test the consistency of the results obtained through the IFS analysis, in Appendix B we present a comparison of the physical parameters

---

[3]This is equivalent to say that the $sSFR(z)$ is below $0.2/t_U(z)$.

[4]Recall that χ^2:

$$\chi^2 = \sum_\lambda \frac{f_{\text{obs}}(\lambda) - f_{\text{model}}(\lambda)}{\sigma(\lambda)^2} \qquad (4.3)$$

where f_{obs} and f_{model} are the observed and the modeled flux intensities at a certain wavelength λ, $\sigma^2(\lambda)$ is the variance of the flux intensity. The reduce χ^2 is given by $\chi^2/\text{d.o.f.}$ where

$$\text{d.o.f.} = N_{\text{SED}} - n_{\text{free}} \qquad (4.4)$$

N_{SED} is the number of points of the SED, and n_{free} is the degrees of freedom, considered in this case as the number of free parameters.

inferred for each galaxy, with the ones reported in the last version on pyPipe3D (Sánchez *et al.*, 2022).

4.1 Mrk290

Mrk290 is a well known broad line AGN classified as QSO and as an UFO with kinematic effects visible in the [OIII]5007 line profile. It has a significant nuclear emission in radio and UV, and as a Markarian galaxy its emission dominates the bluest part of the visible spectra. The apertures and their corresponding reduced χ^2 to best SED fitting models to the spectral data of Mrk290 are tabulated in Table 4.1.

Aperture	$R/R_{\mathrm{eff},K}$	χ^2/d.o.f.
R_{max}	6.023	5.60
$0.75R_{\mathrm{max}}$	4.517	8.41
$0.5R_{\mathrm{max}}$	3.012	17.19
$0.25R_{\mathrm{max}}$	1.506	38.98
R_{1kpc}*	1.340	44.30
$R_{\mathrm{eff,r(s)}}$	1.237	44.30
$R_{\mathrm{eff},K}$**	1.00	47.34
$R_{\mathrm{eff,r(p)}}$**	0.842	54.02

Table 4.1: Apertures of Mrk290 ranked in decreasing order of their size and their corresponding reduced χ^2. *We noticed that $R_{\mathrm{eff,r(s)}}$ and R_{1kpc} apertures enclose the same spectral information, in consequence R_{1kpc} is omitted for simplicity. **Results from $R_{\mathrm{eff},K}$ and $R_{\mathrm{eff,r(p)}}$ must be taken with caution because these apertures are within the PSF radius.

The upper panel of Figure 4.1 shows the observed spectrum of Mrk290 (black solid line) and our best fitting model using BAGPIPES (red solid line). The violet shaded areas show the masked lines and/or regions which were not included in the fits. We also present separately the contribution from the nebular emission, the NLR and BLR from the AGN as well as its continuum. In the bottom part of the same panel we plot the residuals of the best fitting model with respect to the observations[5]. Notice that our errors are of the order of less than $\sim 10\%$ for most of the spectrum. Similarly the lower three panels present a zoom-in into the regions where the contributions of the nebular lines, the NLR and the BLR are more relevant and it is evident that for this galaxy the fitted nebular lines are negligible in all but hydrogen.

---

[5]The format of this figure will be replicated for the rest of the galaxies in our sample, in the following sections.
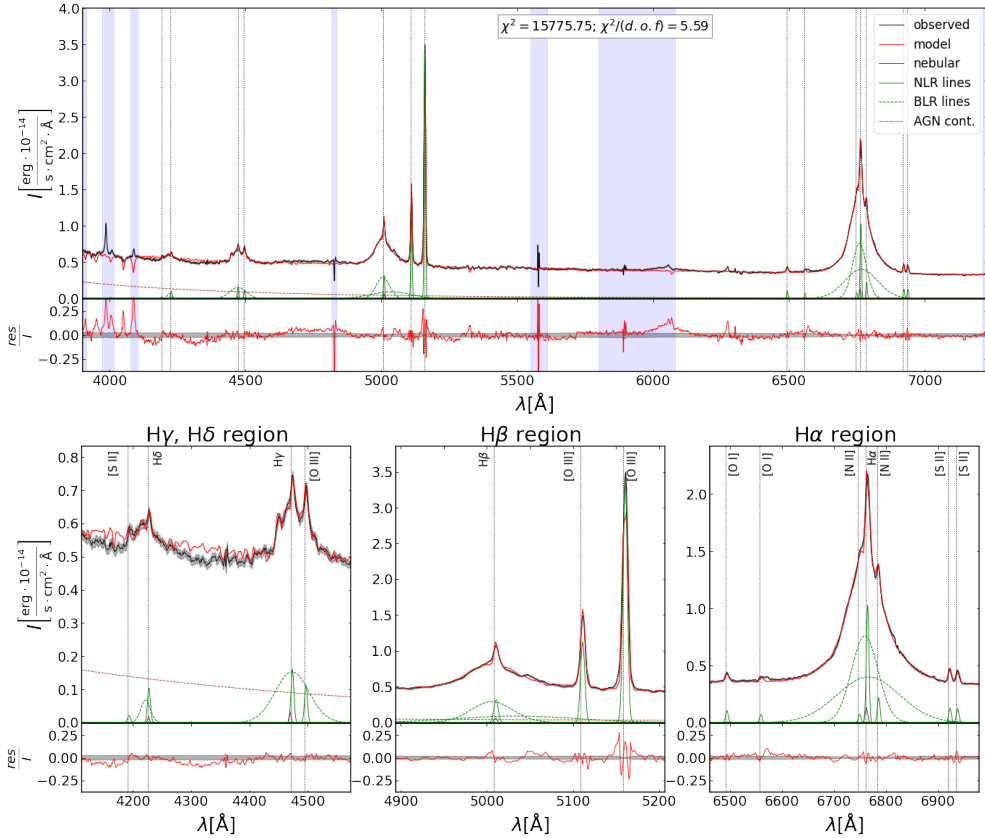
Figure 4.1: Spectral fit of Mrk290 at R_{max} aperture. The *upper* panel shows the entire wavelength range analyzed, while the *bottom* panel zooms in on the vicinity around the Hα, Hβ and Hγ regions. For both panels in their upper plots, the integrated spectrum (black continuum line) is plotted along with the fitted model (red continuum line), the emission lines from the NLR (green continuum lines), the BLR (green dashed lines) and the nebular contribution (purple continuum line), together with the AGN accretion disk continuum contribution (brown dashed line), while the lower plots show the percentage residuals of the fit (red continuum line), compared with the percentage noise of the observed spectrum (grey shaded area). The model of the spectrum considers a SFH described by a DPL, a dust attenuation law from Cardelli *et al.* (1989), nebular emission lines computed by CLOUDY and the contribution of the AGN (NLR, BLR and accretion disk continuum). The masked regions of the spectrum are violet-shaded. The gray vertical dotted lines represent the centroids of the emission lines listed in the methodology (see Section 5). The spectrum is at the observed frame ($z_{\mathrm{obs}} = 0.0302$).

By observing the residuals of the spectral fitting, in general we found that our best fitting models seem to reproduce the observations reasonably well,

despite the slightly large reduced χ^2s in the smaller apertures. Notice that computing the degrees of freedom from our models is not trivial particularly because the covariance matrix from the data cubes is not available. Due to this we chose to use the simplest definition which is to subtract the number of parameters to the number of points in the SED (see Equation 4.4). In that regard and considering that we are using a *Bayesian* method, our reduced χ^2s are just a *guideline* to the figure of merit to our fits.

Next we describe our results about the AGN emission line models:

- Three Gaussian components successfully describe the Hα and Hβ emission lines, one from the NLR and two from the BLR.

- Our results seem to over-predict the AGN continuum in the bluest part of the SED. Nonetheless, this happens only over a small region, between ~ 4100 to 4400 Angstroms.

- Assuming same widths for all emission lines of the NLR, our models reproduce reasonably well their line profiles. We only notice that [OIII]5007 line profile is not very well fitted (see the residuals around this emission line). This may be caused by the effects of an outflow in the [OIII]5007 profile.

Figure 4.2 shows the SFH and the stellar mass formation history (SMFH) for Mrk290 at different apertures, obtained by BAGPIPES's interpolation. Since the SFH and SMFH may be not very reliable for populations older than 9 Gyr (see e.g., Conroy, 2013), we gray shaded the areas that represent times older than 9 Gyr. From this figure we found that:

- The aperture $R_{\mathrm{eff,r(s)}}(=R_{1\mathrm{kpc}})$ is between 2PSF and 3PSF. The peak of its SFH and formation time (t_{form})[6] are around $z \sim 0.7 - 0.8$ (~ 7 Gyr ago) and it became quiescent around $z \sim 0.5$ (~ 5 Gyr ago) according to Pacifici *et al.* (2016) and around $z \sim 0.25$ (~ 3 Gyr ago) according to the BAGPIPES criteria. For $R_{\mathrm{eff,}K}$ the evolution has a similar behaviour and time scales as $R_{\mathrm{eff,r(s)}}$, but it must not be forgotten that $R_{\mathrm{eff,}K}$ is within the PSF radius and its results should be taken with caution.

- The aperture corresponding to $0.25R_{\mathrm{max}}$ is between 1PSF and 2PSF and has undergone an evolution similar to that of $R_{\mathrm{eff,r(s)}}$, accumulating a little more M_* but with a little advance (<0.5 Gyr) in the characteristic times.

---

[6]BAGPIPES criteria defines the formation time t_{form} as the subtraction of the age of the universe $t_U(z_{\mathrm{obs}})$ minus the mass weighted age of the galaxy.
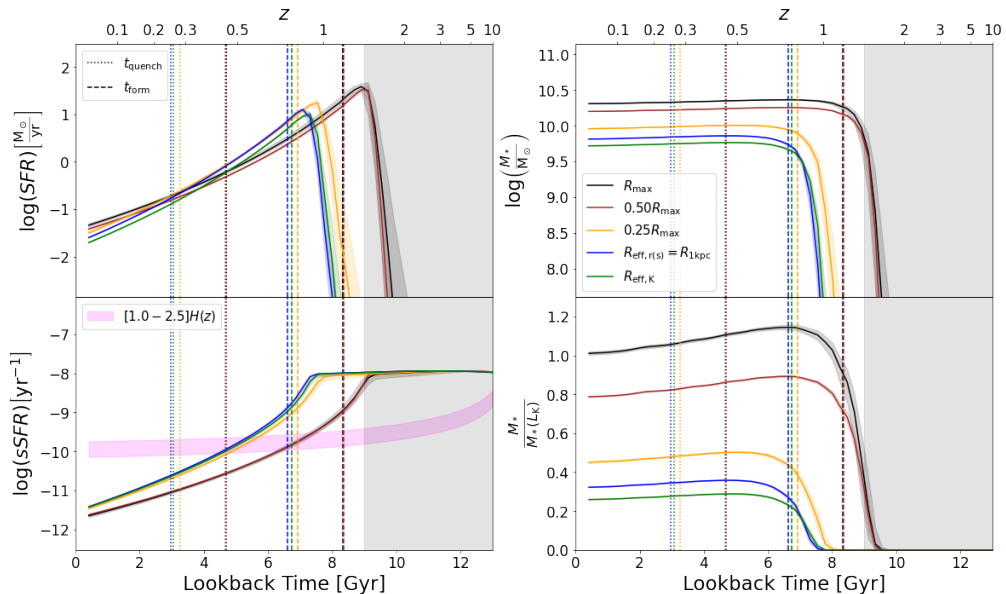
Figure 4.2: Evolution of Mrk290 as a function of the lookback time and the redshift. Each aperture is represented by a different color (black: R_{max}, red: $0.50R_{\mathrm{max}}$, yellow: $0.75R_{\mathrm{max}}$, blue: $R_{\mathrm{eff,r(s)}}=R_{1\mathrm{kpc}}$, and green: $R_{\mathrm{eff},K}$). The t_{form} and t_{quench} from BAGPIPES criteria are showed with vertical dashed and dotted lines, respectively. The *upper-left* panel shows the $SFR(t(z))$. The *bottom-left* panel shows the $sSFR(t(z))$ together with the Pacifici *et al.* (2016) quenching criteria, established by $2.5H(z)$ (magenta band with values between $1.0 - 2.5H(z)$). The *upper-right* panel shows the logarithm of the $M_*(t(z))$. The *bottom-right* panel shows the quotient between $M_*(t(z))$ and the total stellar mass inferred by L_K, $M_{*,K}$ (see Equation 2.1). The SFH was modelled using a DPL model (see Equation 3.2). The evolution of these parameters was obtained by using an interpolation done by BAGPIPES to predict the physical quantities for redshifts from $z_{\mathrm{obs}} \approx 0.0302$ to $z = 10$. Ages larger than 9 Gyr are gray-shaded, to highlight that the ages of older stellar populations may not be very reliable (see e.g., Conroy, 2013).

- The maximum aperture R_{max} is well beyond 3PSF and corresponds to $\sim 6 \times R_{\mathrm{eff},K}$, so it displays the most robust measurements of all the used apertures. We found that the peak of SFH and t_{form} for this aperture were around $z \sim 1.1 - 1.5$ ($\sim 8 - 9$ Gyr ago) and it became quiescent around $z \sim 0.7 - 0.9$ (~ 7 Gyr ago) according to the Pacifici *et al.* (2016) criteria and at $z \sim 0.4$ (~ 4.5 Gyr ago) according to BAGPIPES. The $0.50R_{\mathrm{max}}$ aperture, which is between 2PSF and 3PSF radius, describes a very similar evolution.

Figure 4.3 shows the radial dependence of the SFR, $sSFR$, M_*, Z_*, A_V, t_{form}, the quenching time (t_{quench}, from BAGPIPES criteria) and the quenching scale ($\tau_{\mathrm{quench}} = t_{\mathrm{quench}} - t_{\mathrm{form}}$). The mentioned scale times are represented since the BB. For all the apertures we found that the metallicity is subsolar (<0.1 $Z_\odot$) and the amount of attenuation due to dust is small (practically 0.0 magnitudes).

In general, our results above 1PSF show that Mrk290 has slightly a positive gradient in its SFR profile (in other words, the SFR at the centre is lower than in the outskirts) but a slightly higher $sSFR$ at the centre and a rising subsolar metallicity gradient (from 0.02 to 0.1 $Z_\odot$). We also found that there are younger stars towards the centre of the galaxy, perhaps due the slightly higher $sSFR$, than in the outskirts. We speculate that the origin for the high luminosity AGN and the negative gradients of $sSFR$ and stellar population ages could be related to the accretion of gas with low angular momentum. We will discuss more about this in Chapter 5.

The series of panels on Figure 4.4 show the integrated luminosities of the narrow lines that will be later used in the BPT diagrams (Hα, Hβ, [NII]6583, [OIII]5007, [OI]6300, [SII]6717,6731). The dashed and dotted lines show the contribution from the NLR and Nebular emission inferred by BAGPIPES, respectively. In all the panels, total luminosities (solid lines) increase as we move away from the centre. Notice that the NLR tends to dominate the emission of the narrow lines above the nebular contribution, this is consistent with the fact that the AGN is dominating the emission. Also, using the relevant ratios of the total narrow line luminosities, we found that Mrk290 is located in the AGN region of the BPT diagrams (Figure 4.5). In the other hand, Mrk290 is located in the SF region of the WHAN diagram due to the low value of the quotient $L_{\mathrm{[NII]}}/L_{\mathrm{H\alpha}}$ (see Figure 4.6), but this classification does not considers the information of [OIII] and Hβ (which is the main reason for the Seyfert identification of this galaxy in the BPT diagrams). Considering the above and the fact that this galaxy has been identified as a UFO, it can be concluded that Mrk290 is indeed a Seyfert type AGN.

The panels of Figure 4.7 show the integrated luminosities for the broad Balmer lines coming from the BLR (Hα_{b}, Hα_{vb}, Hβ_{b}, Hβ_{vb}, Hγ_{b}, Hδ_{b}), where
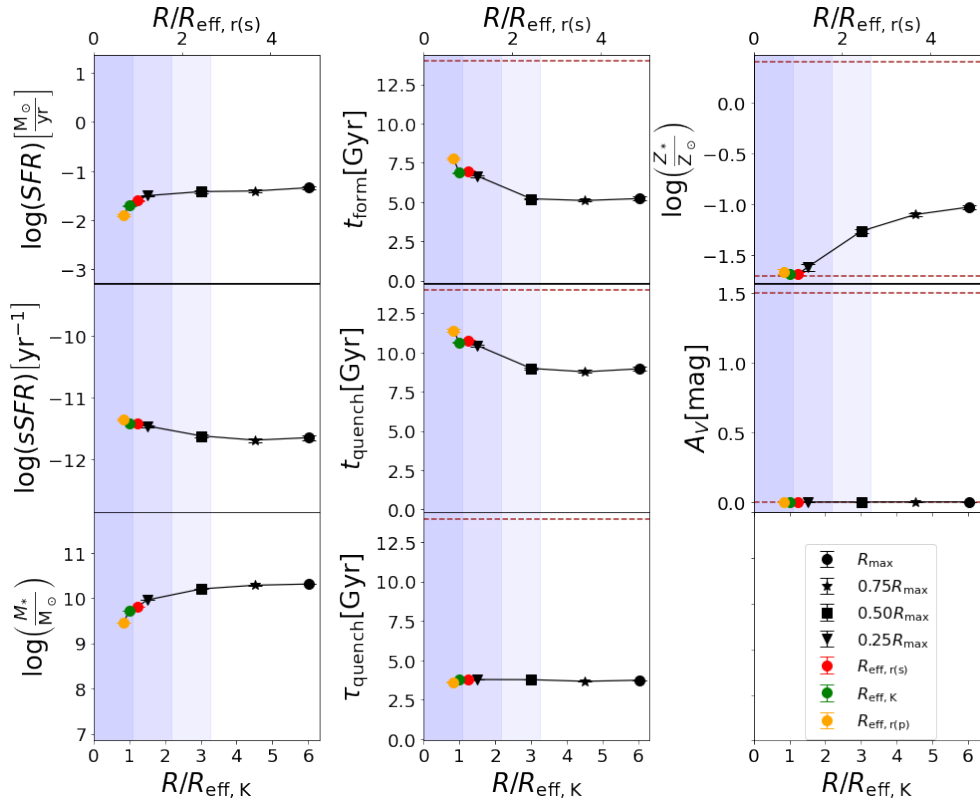
Figure 4.3: Mrk290 parameter radial profiles. The *upper-left* panel shows the SFR. The *middle-left* panel shows the $sSFR$. The *bottom-left* panel shows the logarithm of the M_*. The *upper-central* panel shows the $t_{\rm form}$. The *middle-central* panel shows the $t_{\rm quench}$. The *bottom-central* panel shows the $\tau_{\rm quench}$. The *upper-right* panel shows the logarithm of the Z_*, pointing out the borders of the logarithmic uniform prior (from 0.02 to 2.5 $Z_\odot$) with a brown dashed line. The *middle-right* panel shows the A_V from the dust in magnitudes, pointing out the borders of the uniform prior (from 0.0 to 1.5 mag). The *bottom-right* panel shows the markers assigned to each aperture. The mentioned scale times are represented since the BB, pointing out $t_U(z_{obs})$ with a brown dashed line as the maximum possible value. The inferred values at the different apertures of each physical parameter are plotted with their errors (remember that the best fitting values and the uncertainties where obtained by considering the 50th, 16th and 84th percentiles of the posterior distributions). In this case, the uncertainties of all the parameters are very small, in consequence their error bars are negligible. Each aperture is represented by a different marker (black circle: $R_{\rm max}$, black star: $0.75R_{\rm max}$, black square: $0.50R_{\rm max}$, black triangle: $0.25R_{\rm max}$, red circle: $R_{\rm eff,r(s)}=R_{\rm 1kpc}$, green circle: $R_{\rm eff,K}$, and yellow circle: $R_{\rm eff,r(p)}$). The violet shaded areas represent 1PSF, 2PSF and 3PSF radius, distinguished by the opacity.
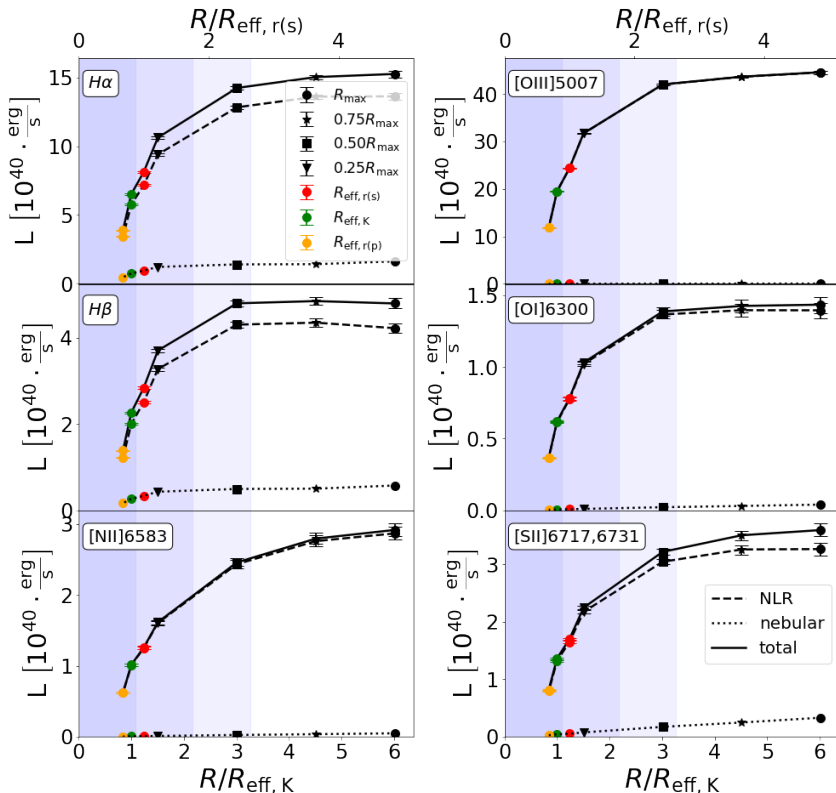
Figure 4.4: Mrk290 narrow lines luminosity profiles. Narrow lines from the NLR (dashed line), the nebular emission (dotted line) and the sum (solid line). Each aperture is represented by a different marker (black circle: R_{max}, black star: $0.75R_{max}$, black square: $0.50R_{max}$, black triangle: $0.25R_{max}$, red circle: $R_{eff,r(s)}=R_{1kpc}$, green circle: $R_{eff,K}$, and yellow circle: $R_{eff,r(p)}$). The violet shaded areas represent 1PSF, 2PSF and 3PSF radius, distinguished by the opacity.

the dashed and dotted lines show the contribution from the broad and the very broad components (for Hα and Hβ lines) respectively.

Analyzing the broad emission lines from the BLR we can infer several properties of the AGNs, such as their mass, luminosity, and accretion rate. Here we use the BLR and the single epoch spectroscopy method to infer M_{BH} (Greene & Ho, 2005) both for the Hα and Hβ lines (considering the sum of the *broad* and the *very broad* components). Since the integrated emission from the BLR has been obtained at different apertures, we estimate the M_{BH} at different radii[7] as shown in Figure 4.8. We notice that our results converge to the same BH

---

[7]It was made at the different apertures expecting the inferences to be the same for all, because the SMBH is located in the very centre of the galaxy.
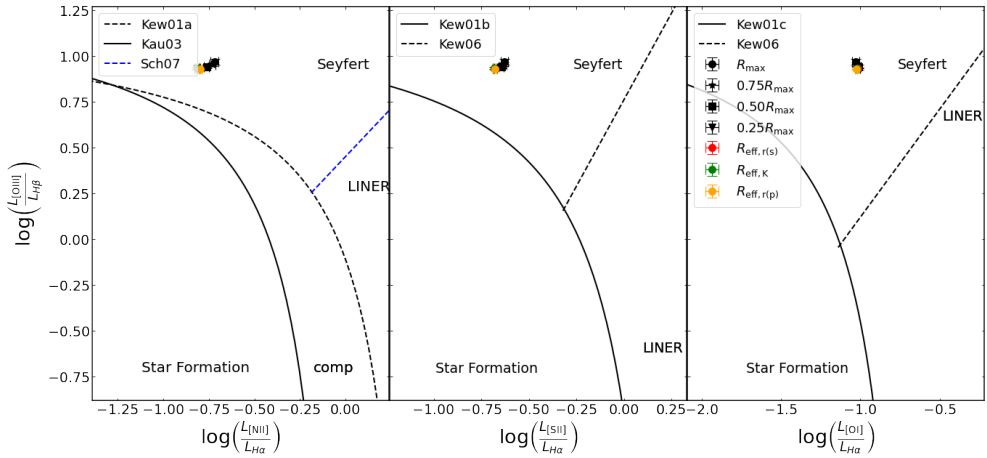
Figure 4.5: Mrk290 in BPT diagram. Each aperture is represented by a different marker (black circle: R_{max}, black star: $0.75R_{\mathrm{max}}$, black square: $0.50R_{\mathrm{max}}$, black triangle: $0.25R_{\mathrm{max}}$, red circle: $R_{\mathrm{eff,r(s)}}=R_{\mathrm{1kpc}}$, green circle: $R_{\mathrm{eff},K}$, and yellow circle: $R_{\mathrm{eff,r(p)}}$). All the analyzed apertures were located in the Seyfert region of the three diagrams.

mass value of $M_{\mathrm{BH}} \sim 2 \times 10^7$ $\mathrm{M}_\odot$, just after surpassing the PSF dominated measurements. This value is consistent with the more complex measurement based on the reverberation mapping $M_{\mathrm{BH}} \sim 1.8 \times 10^7$ $\mathrm{M}_\odot$ (blue dotted line in the figure; see Denney *et al.*, 2010). This is reassuring since it means that our *phenomenological* AGN model seems to be *realistic* enough to even predict the SMBH mass of Mrk290.

Finally, Figure 4.9 shows the radial profiles of the inferred M_*, SFR, t_{form}, t_{quench} and τ_{quench}, where the mentioned scale times are represented since the BB. For this galaxy we only show the profiles obtained through the spectral fitting of the IFS data. We omitted the broad band SED fitting results since they are not reliable due to the complexity of correctly modeling the AGN contribution at the ultraviolet part of the spectrum. Even so the fitted profiles of M_* and SFR are compared to the empirical profiles obtained through the photometric surface brightness profile information (see Equations 4.1 and 4.2). From this analysis it is evident that the empirically inferred SFRs are over-estimated approximately by 2 orders of magnitude, while M_* is slightly under-estimated for ~ 0.5 dex for apertures beyond 1PSF. The above is not surprising as this result points-out to the need of correctly subtract the contribution of the AGN.
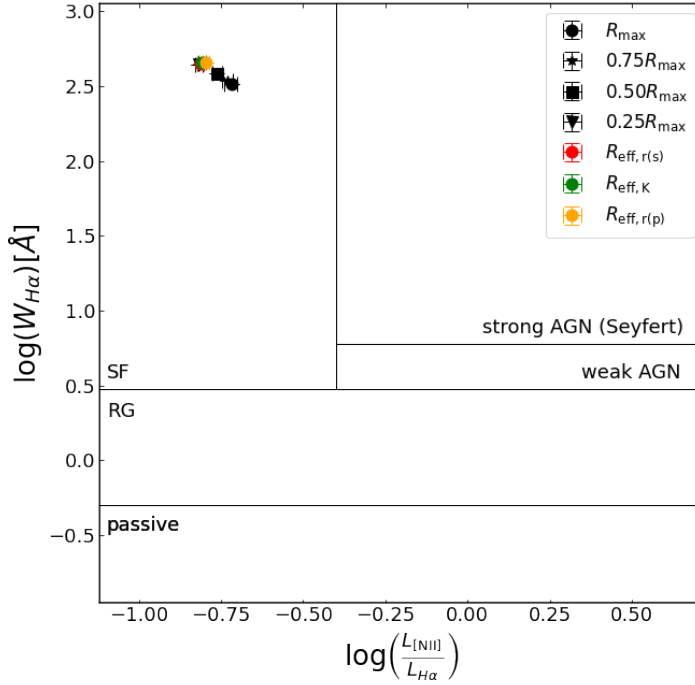
Figure 4.6: Mrk290 in the WHAN diagram. Each aperture is represented by a differ-ent marker (black circle: R_{max}, black star: $0.75R_{\mathrm{max}}$, black square: $0.50R_{\mathrm{max}}$, black triangle: $0.25R_{\mathrm{max}}$, red circle: $R_{\mathrm{eff,r(s)}}{=}R_{\mathrm{1kpc}}$, green circle: $R_{\mathrm{eff,K}}$, and yellow circle: $R_{\mathrm{eff,r(p)}}$). All the analyzed apertures were located in the SF region.
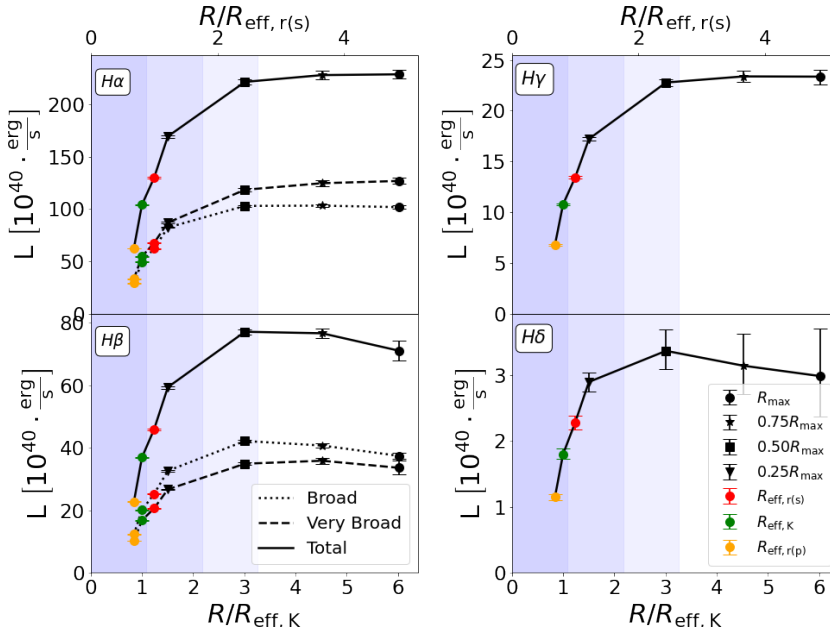
Figure 4.7: Mrk290 broad lines luminosity profiles. In the case of Hα and Hβ the total profile (solid line) is the result of the sum of two components: the *broad* (dotted line) and the *very broad* (dashed line). Each aperture is represented by a different marker (black circle: R_{max}, black star: $0.75R_{max}$, black square: $0.50R_{max}$, black triangle: $0.25R_{max}$, red circle: $R_{eff,r(s)}=R_{1kpc}$, green circle: $R_{eff,K}$, and yellow circle: $R_{eff,r(p)}$). The violet shaded areas represent 1PSF, 2PSF and 3PSF radius, distinguished by the opacity.
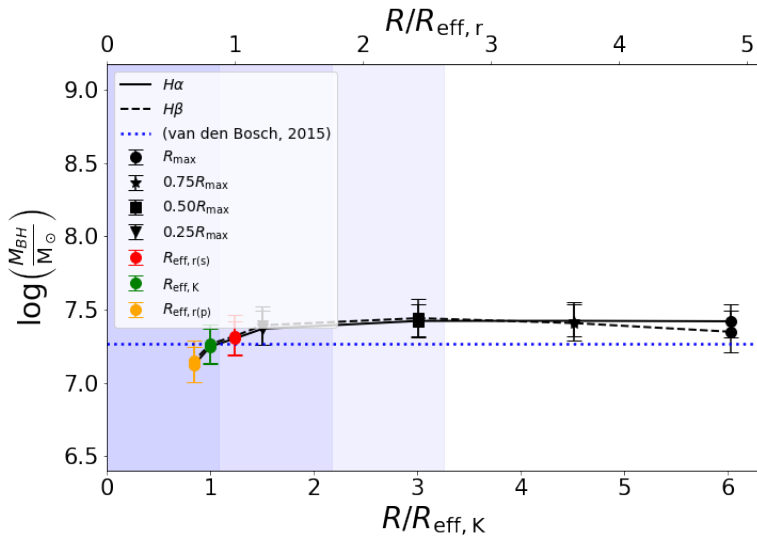
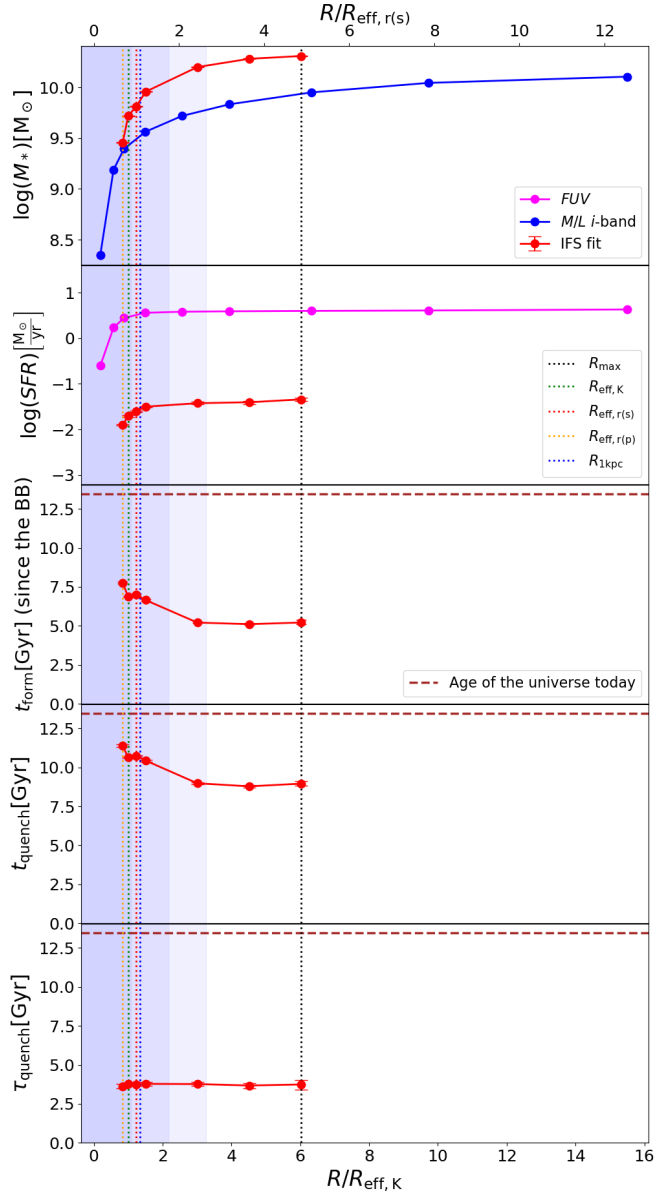Figure 4.8: Mrk290 M_{BH} inferred at different apertures. Each aperture is represented by a different marker (black circle: R_{max}, black star: $0.75R_{\mathrm{max}}$, black square: $0.50R_{\mathrm{max}}$, black triangle: $0.25R_{\mathrm{max}}$, red circle: $R_{\mathrm{eff,r(s)}}{=}R_{\mathrm{1kpc}}$, green circle: $R_{\mathrm{eff},K}$, and yellow circle: $R_{\mathrm{eff,r(p)}}$). The violet shaded areas represent 1PSF, 2PSF and 3PSF radius, distinguished by the opacity.

Figure 4.9: Mrk290 parameter radial profiles. From top to bottom, the panels are: the stellar mass, the star formation rate, the formation time, the quenching time and the quenching scale. The times scales are considered since the BB. The spectroscopic profile (red line) is shown together with the empirical profiles of the stellar mass (blue line; Taylor *et al.*, 2015) and the SFR (magenta line; Kennicutt, 1998). The photometric profile is not shown for this galaxy. The violet shaded areas represent 1PSF, 2PSF and 3PSF radius of the IFS data, distinguished by the opacity.

4.2   ARP151

ARP151 is a well known broad line AGN, it has a significant nuclear emission in radio and UV, and as a Markarian galaxy its emission dominates the bluest part of the visible spectra. It is an interacting galaxy with tidal tails (much more evident in the central region of the UV image) and a second galaxy near the FoV with no emission lines but Balmer absorption. The apertures and their corresponding reduced χ^2 of the best spectral fitting models to the IFS data of ARP151 are tabulated in Table 4.2.

Aperture	$R/R_{\text{eff},K}$	χ^2/d.o.f.
R_{max}	1.164	2.71
$R_{\text{eff},K}$	1.00	3.28
$0.75R_{\text{max}}$	0.873	4.41
$0.5R_{\text{max}}$	0.582	10.11
$R_{\text{eff,r(s)}}$	0.527	11.91
$R_{\text{eff,r(p)}}$	0.367	22.01
R_{1kpc}	0.356	22.54
$0.25R_{\text{max}}$	0.291	28.3

Table 4.2: Apertures of ARP151 ranked in decreasing order of their size and their corresponding reduced χ^2.

Figure 4.10 shows the observed spectrum of ARP151 and our best fitting model, together with the separated contribution from nebular emissions, the NLR and BLR from the AGN, as well as the AGN continuum, similarly to Figure 4.1 for Mrk290. Notice that our errors are of the order of less than $\sim 10\%$ for most of the spectrum. In addition, note that it is evident that for this galaxy all the fitted nebular lines are negligible.

In general we found that our best fitting models reproduce the observations reasonably well. Inner apertures seem to have slightly larger values of reduced χ^2 as the apertures decrease in size. Our results with respect to the AGN emission line models are:

- Similarly to Mrk290, three Gaussian components were necessary to successfully describe the Hα and Hβ emission lines, one from the NLR and two from the BLR.

- It was necessary to model the AGN continuum in the bluest part of the SED by a power law. Even when the fitted power law index was very negative at all apertures (< -6.0; see O'Dell, 1986; O'Dell *et al.*, 1987, for more information about the AGN continuum models), our model seems to describe slightly well the observed SED.
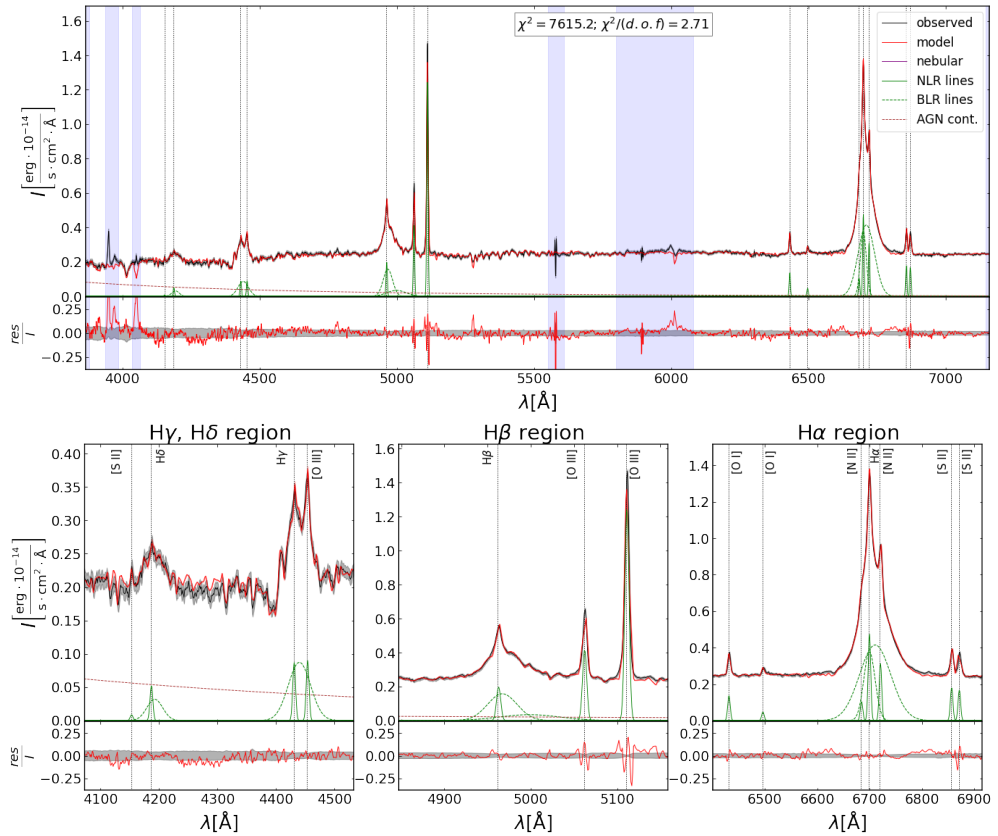
Figure 4.10: Spectral fit of ARP151 at R_{max} aperture. The description is similar to Figure 4.1. The spectrum is at the observed frame ($z_{obs} = 0.0207$).

- Assuming the same widths for all emission lines of the NLR, our models reproduce reasonably well the line profiles. We only notice that [OIII]5007 line profile is not very well fitted (see the residuals around this emission line). Nonetheless, the error around this line is less than $\sim 5\%$.

Figure 4.11 shows the SFH and the SMFH for ARP151. The inner aperture measured for ARP151 is $0.25R_{max}$ and it is located between 1PSF and 2PSF, as well as R_{1kpc} and $R_{eff,r(p)}$. Apertures $R_{eff,r(s)}$ and $0.50R_{max}$ are located between 2PSF and 3PSF while the outer apertures $0.75R_{max}$, $R_{eff,K}$ and R_{max} are well beyond 3PSF. Within all the apertures the peak of the SFH and the t_{form} are at $z \sim 7 - 9$ (~ 12.5 Gyr ago) and became quiescent at $z \sim 4 - 5$ (~ 12 Gyr ago) according to the Pacifici and the BAGPIPES criteria. We caution that this galaxy is dominated by old, > 9 Gyr, stellar population. However we will continue discussing its results because this galaxy seems to be quenched since
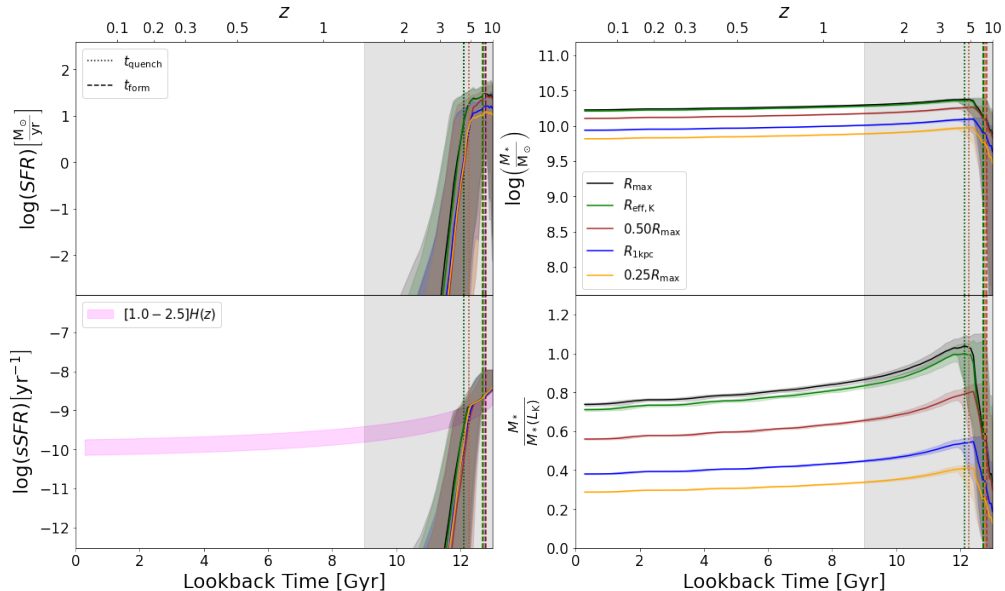
a long time ago.

Figure 4.11: Evolution of ARP151. The description is similar to Figure 4.2.. Each aperture is represented by a different color (black: R_{max}, green: $R_{eff,K}$, red: $0.50R_{max}$, blue: R_{1kpc}, and yellow: $0.25R_{max}$). The evolution of these parameters was obtained by using an interpolation done by Bagpipes to predict the physical quantities for redshifts from $z_{obs} \approx 0.0207$ to $z = 10$.

Figure 4.12 shows the radial dependence of the physical parameters of the galaxy, it is similar to Figure 4.3. We found that within all apertures, Z_* has a flat gradient around a subsolar value ($\sim 0.25\ Z_\odot$) and a slightly negative gradient in its dust A_V (from 0.6 to 0.5 magnitudes approximately). However, notice that for these apertures the SFRs are too low since this is a very quenched galaxy and the SFR and the $sSFR$ profiles are out of the canonical values for the ranges of this figure. We also found flat gradients of the scale times, having very old stellar populations at all apertures.

All the evidences point out that ARP151 formed from a very intense burst of star formation that started at $z \sim 10$ and by $z \sim 5$ it was in decline already. In other words, ARP151 seems to have formed over a period of ~ 300 Myr from an intense burst of star formation. The low metallicity of the stars reflect the fact that ARP151 should have formed from primordial gas. Also, this galaxy quenched already $\lesssim 1$ Gyr after the BB and kept like that. The burst of star formation followed by the sudden quenching of star formation makes ARP151 an interesting object to compare with high redshift galaxies that quenched at $z > 3$ Carnall $et\ al.$ (2023a,b).
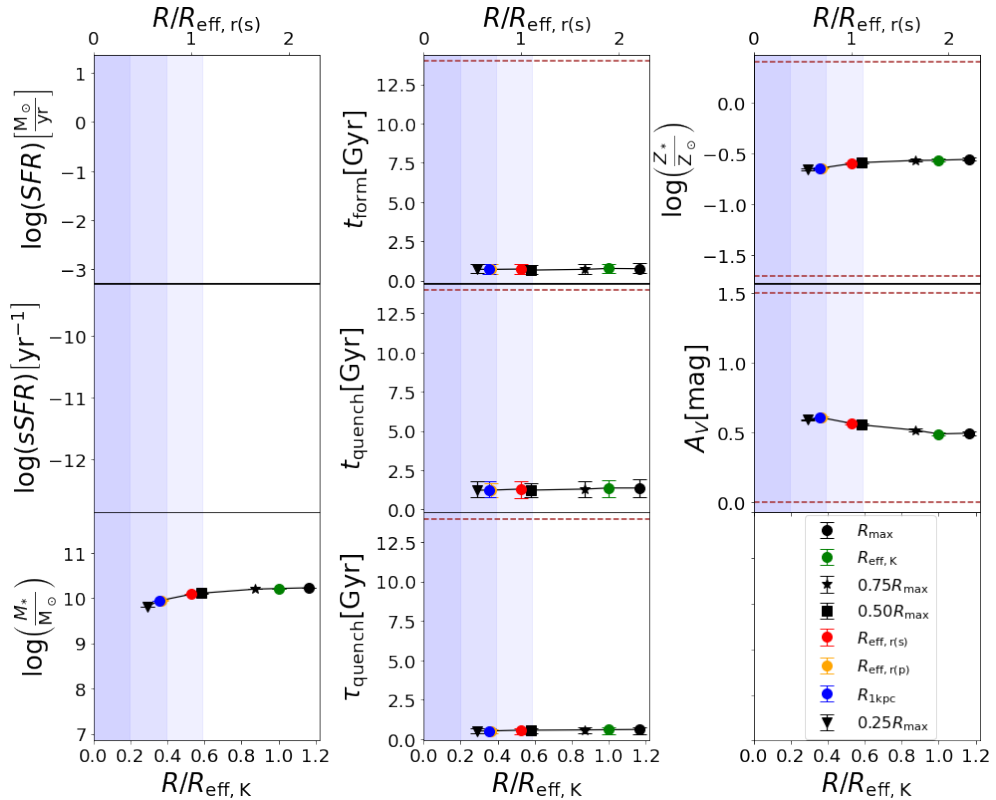
Figure 4.12: ARP151 parameter radial profiles. The description is similar to Figure 4.3. Each aperture is represented by a different marker (black circle: R_{max}, green circle: $R_{eff,K}$, black star: $0.75R_{max}$, black square: $0.50R_{max}$, red circle: $R_{eff,r(s)}$, yellow circle: $R_{eff,r(p)}$, blue circle: R_{1kpc}, and black triangle: $0.25R_{max}$). In this case, the uncertainties of all the parameters except t_{form} and τ_{form} are very small, in consequence the error bars are negligible. The fit converged to a very quenched galaxy, so the inferred SFR and $sSFR$ profiles are too low to appear in their respective panels.

Figure 4.13 presents the radial profiles of the integrated luminosities of the narrow lines, similar to Figure 4.4, but this time for ARP151. Notice how the luminosity of the AGN narrow emission lines dominates the emission over the negligible nebular ones and how the total luminosity of every line increases as we move away from the centre. Figure 4.14 shows the three different BPT diagrams, and all of them confirm that the emission comes from an AGN, as it is consistent with the region designated for Seyfert galaxies (see Khachikian & Weedman, 1974). The WHAN diagram of Figure 4.15 also confirms that ARP151 is a Seyfert galaxy.

We use our best fit model for the BLR parameters (see the integrated lu-
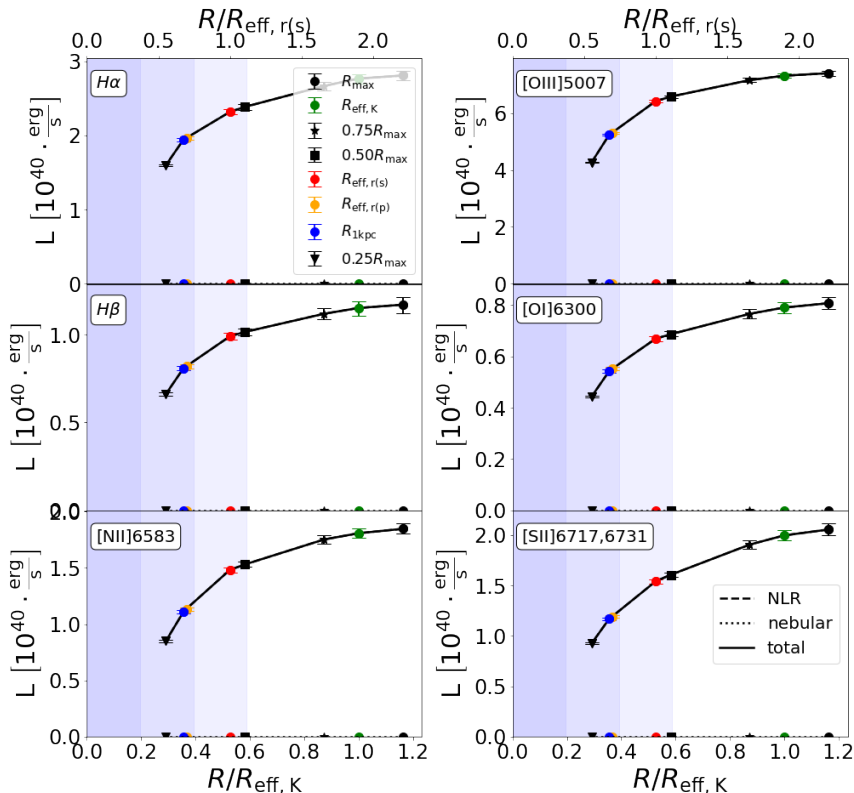
Figure 4.13: ARP151 narrow lines luminosity profiles. The description is similar to Figure 4.4. Each aperture is represented by a different marker (black circle: R_{max}, green circle: $R_{\mathrm{eff},K}$, black star: $0.75R_{\mathrm{max}}$, black square: $0.50R_{\mathrm{max}}$, red circle: $R_{\mathrm{eff,r(s)}}$, yellow circle: $R_{\mathrm{eff,r(p)}}$, blue circle: R_{1kpc}, and black triangle: $0.25R_{\mathrm{max}}$).

minosities profiles of the broad Balmer lines coming from the BLR in Figure 4.16) to infer the BH mass from ARP151 based on a single epoch spectroscopy technique (Greene & Ho, 2005). We use Hα and Hβ broad lines which result in masses of 2×10^6 M$_\odot$ and 3×10^6 M$_\odot$ respectively (see Figure 4.17). Both are consistent, with the mass of $\sim 4.5 \times 10^6$ M$_\odot$ based on the reverberation mapping technique (see Bentz *et al.*, 2010).

Finally, Figure 4.18 shows the radial profiles of M_*, SFR and the scale times, similar to Figure 4.9, but for ARP151. Like Mrk290, for this galaxy we only show the profiles obtained from the spectral fit to the IFS data. We are omitting the broad-band fitting results since they are not reliable due to the presence of the AGN contribution. Despite that, the fitted profiles of M_* and SFR are compared with the empirical profiles from the integrated FUV profile and the $g - i$ color profile obtained through the surface brightness profile infor-
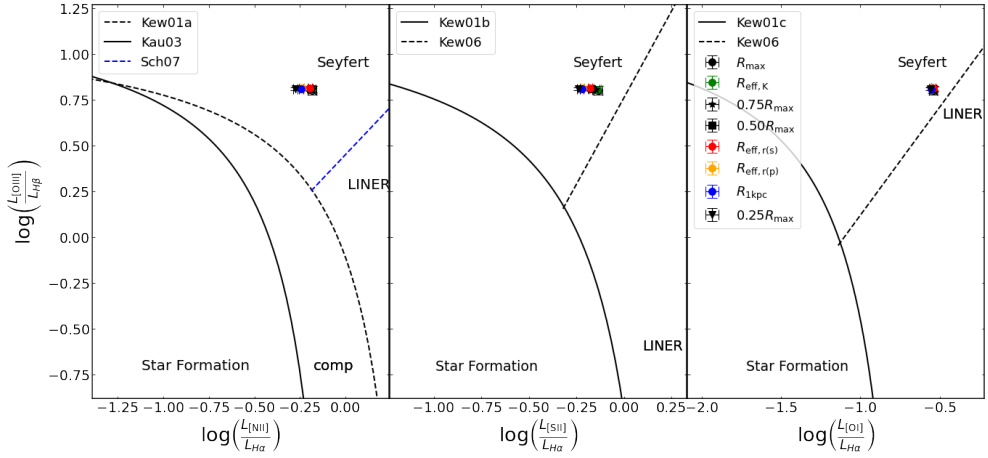
Figure 4.14: ARP151 in BPT diagram. The description is similar to Figure 4.5. Each aperture is represented by a different marker (black circle: R_{max}, green circle: $R_{\mathrm{eff},K}$, black star: $0.75R_{\mathrm{max}}$, black square: $0.50R_{\mathrm{max}}$, red circle: $R_{\mathrm{eff,r(s)}}$, yellow circle: $R_{\mathrm{eff,r(p)}}$, blue circle: R_{1kpc}, and black triangle: $0.25R_{\mathrm{max}}$). All the analyzed apertures were located in the Seyfert region of the three diagrams.

mation: from this it is evident that the empirically inferred SFR is extremely overestimated while M_* is under-estimated for ~ 0.5 dex.
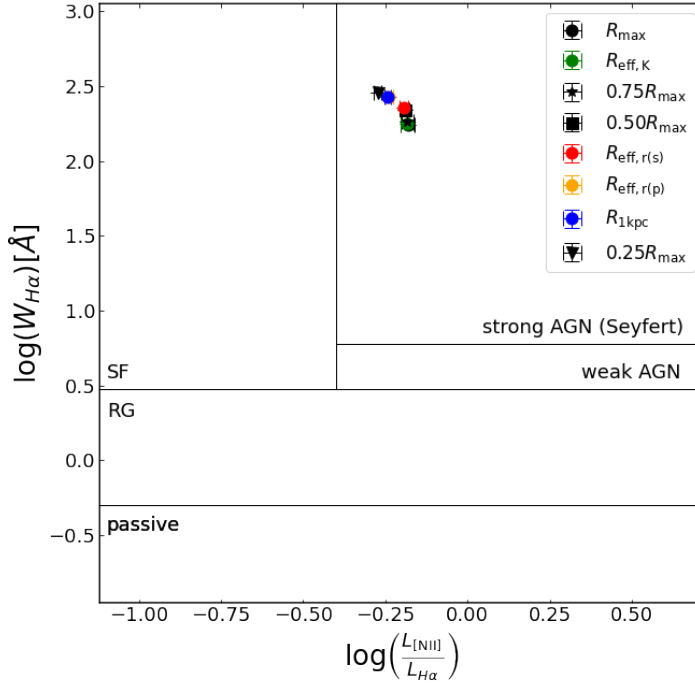
Figure 4.15: ARP151 in the WHAN diagram. The description is similar to Figure 4.6. Each aperture is represented by a different marker (black circle: R_{max}, green circle: $R_{eff,K}$, black star: $0.75R_{max}$, black square: $0.50R_{max}$, red circle: $R_{eff,r(s)}$, yellow circle: $R_{eff,r(p)}$, blue circle: R_{1kpc}, and black triangle: $0.25R_{max}$). All the analyzed apertures were located in the Seyfert region.
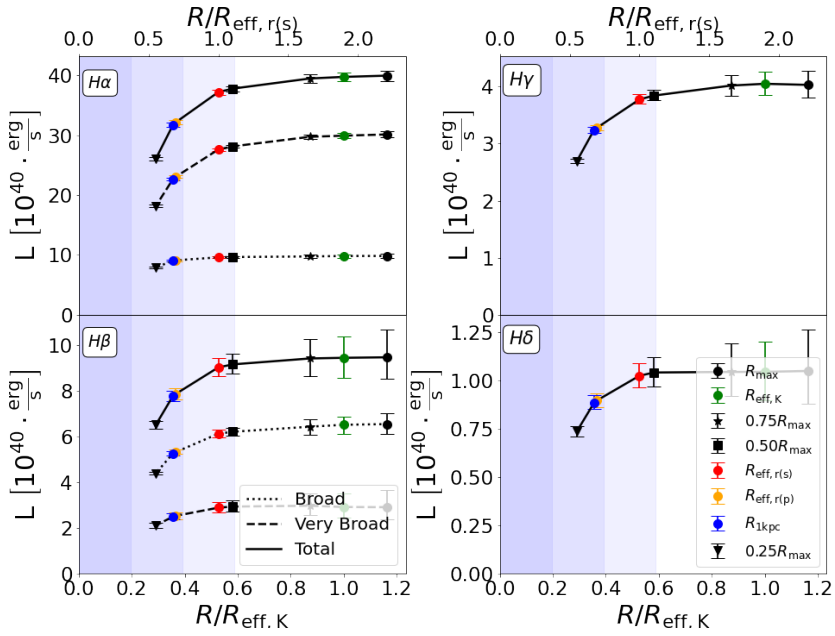
Figure 4.16: ARP151 broad lines luminosity profiles. The description is similar to Figure 4.7. Each aperture is represented by a different marker (black circle: R_{max}, green circle: $R_{\mathrm{eff},K}$, black star: $0.75R_{\mathrm{max}}$, black square: $0.50R_{\mathrm{max}}$, red circle: $R_{\mathrm{eff,r(s)}}$, yellow circle: $R_{\mathrm{eff,r(p)}}$, blue circle: R_{1kpc}, and black triangle: $0.25R_{\mathrm{max}}$).
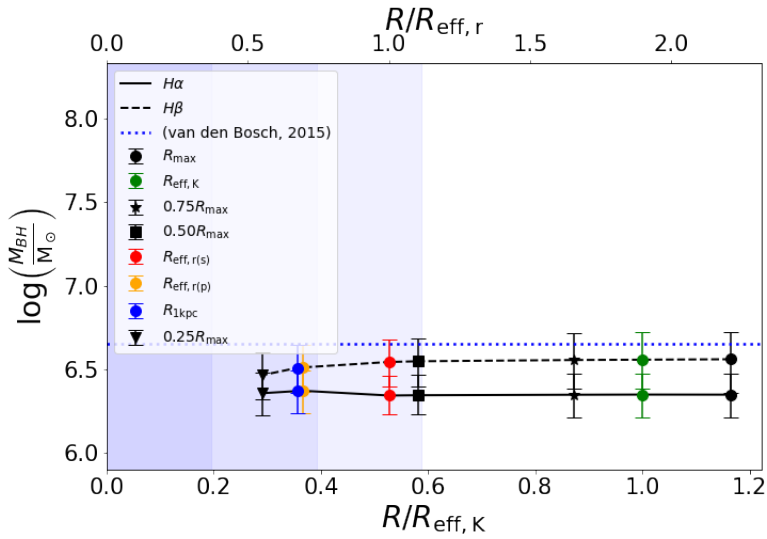
Figure 4.17: ARP151 M_{BH} inferred at different apertures. The description is similar to Figure 4.8. Each aperture is represented by a different marker (black circle: R_{max}, green circle: $R_{\mathrm{eff},K}$, black star: $0.75R_{\mathrm{max}}$, black square: $0.50R_{\mathrm{max}}$, red circle: $R_{\mathrm{eff},\mathrm{r}(\mathrm{s})}$, yellow circle: $R_{\mathrm{eff},\mathrm{r}(\mathrm{p})}$, blue circle: R_{1kpc}, and black triangle: $0.25R_{\mathrm{max}}$).
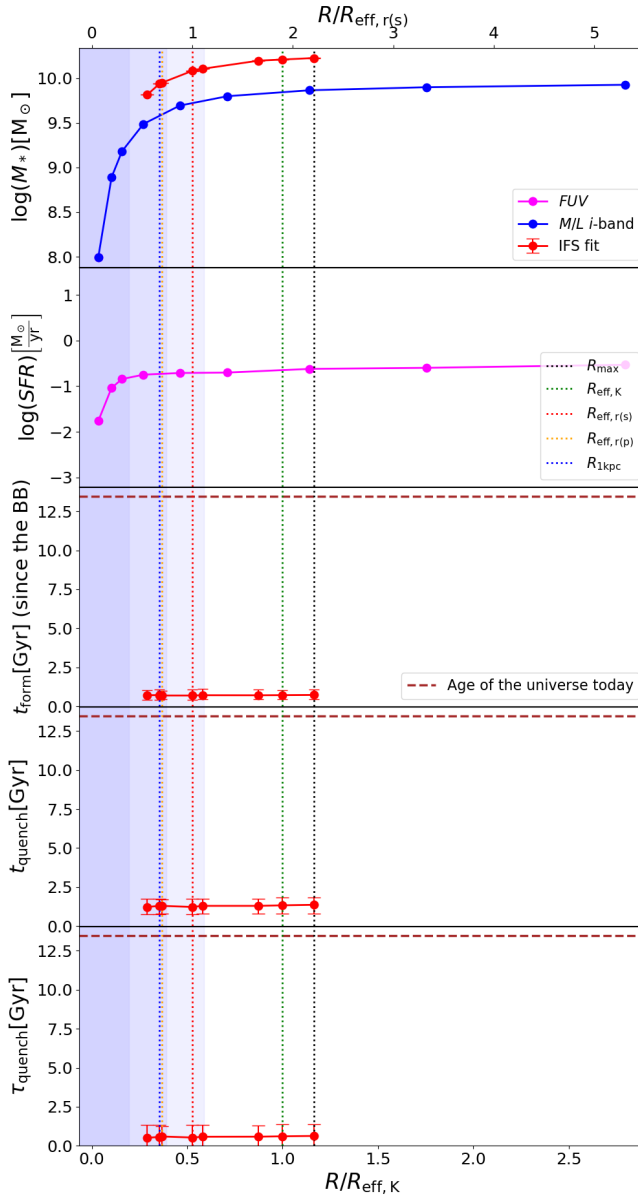
Figure 4.18: ARP151 parameter radial profiles. The description is similar to Figure 4.9. The photometric profile is not shown for this galaxy

4.3   NGC1194

NGC1194 is a well known AGN with prominent narrow emission lines and a significant nuclear emission in radio, together with a faint UV emission. The apertures and their corresponding reduced χ^2 of the best SED fitting models to the IFS data of NGC1194 are tabulated in Table 4.3. The best SED fit and its comparison to the IFS data of galaxy NGC1194 is shown in Figure 4.19 for the maximum aperture.

Aperture	$R/R_{\mathrm{eff},K}$	$\chi^2/$d.o.f.	$\chi^2/$d.o.f.$_{\mathrm{No-ANG}}$
$R_{\max}$	0.860	0.66	1.15
$R_{\mathrm{eff,r(p)}}$	0.775	0.78	1.40
$0.75R_{\max}$	0.645	1.07	2.03
$0.5R_{\max}$	0.430	2.05	4.31
$0.25R_{\max}$	0.215	5.22	13.57
R_{1kpc}	0.182	6.36	21.26

Table 4.3: Apertures of NGC1194 ranked in decreasing order of their size and their corresponding reduced χ^2.

Some apertures display very low reduced χ^2 which are below 1.00; while this could point out that our model is likely to be over-fitting the data presumably because the presence of an AGN, this is disputable. We have redone all our calculations but this time removing the presence of the AGN. We find that the new χ^2 increase by a factor of $\sim 70 - 230\%$ rejecting the above idea. We thus conclude that an AGN is required in addition, as we will see further in this Section, since the emission of those lines is consistent with being emitted by an AGN as shown by the BPT diagrams. Moreover, this AGN has been previously classified as a Seyfert (Véron-Cetty & Véron, 2006).

Figure 4.20 shows the SFH and the SMFH for NGC1194. We found that:

- The inner aperture that we have analysed is $R_{\mathrm{1kpc}} \sim 0.2 \times R_{\mathrm{eff},K}$. For this aperture, the peak of SF occurs at early epochs, it has a formation time of $z \sim 6 - 7$ (~ 12.5 Gyr ago), and then declines slowly with time. Within the aperture of R_{1kpc}, NGC1194 became quiescent early after its formation according to Pacifici criteria and at $z \sim 3$ (~ 11 Gyr ago) according to BAGPIPES. Notice, however, that this should be taken with caution because R_{1kpc} is between 1PSF and 3PSF.

- Aperture $0.25R_{\max}$ has a similar evolutionary history than R_{1kpc}.

- We found that the apertures between $0.4 - 0.9 \times R_{\mathrm{eff},K}$ produce similar SFHs and SMFHs. Within those apertures, the mass increased due to
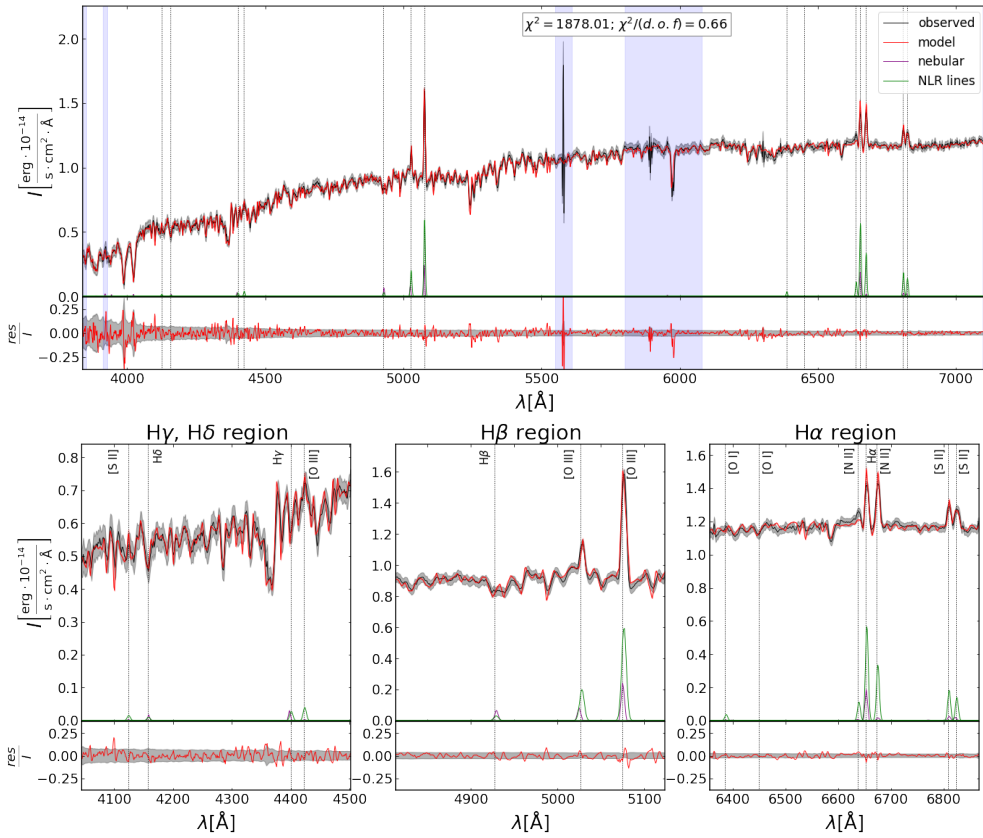
Figure 4.19: Spectral fit of NGC1194 at the maximum aperture. The description is similar to Figure 4.1. The spectrum is at the observed frame ($z_{\mathrm{obs}} = 0.0136$).

the extended period of star formation in the galaxy having a formation time at $z \gtrsim 1$ (~ 9 Gyr ago). Indeed, NGC1194 was still a star forming galaxy just very recently until it became quenched at $z \sim 0.5$ (~ 5 Gyr ago) according to Pacifici criteria and at $z \sim 0.2$ (~ 3 Gyr ago).

Figure 4.21 shows the the radial parameters of the stellar population of NGC1194. The radial properties of NGC1194 fits into the canonical picture of galaxy formation: NGC1194 formed from the inside-out, older central regions and young outskirts, and also quenched from the inside-out most likely due to the activity of its AGN (see Chapter 5 for a discussion).

Figure 4.22 shows luminosities for the the fitted narrow lines of NGC1194. When analysing the BPT diagram (Figure 4.23) our results confirm that the central emission comes from a source that is consistent with a Type 2 AGN similar to what has been discussed in the literature (Véron-Cetty & Véron,
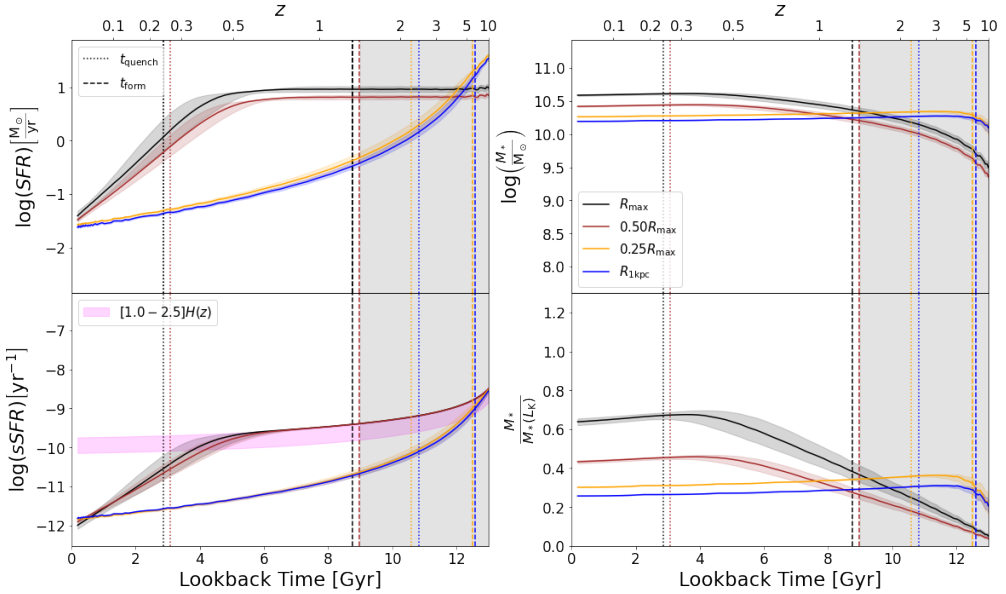
Figure 4.20: Evolution of NGC1194. The description is similar to Figure 4.2. Each aperture is represented by a different color (black: R_{max}, red: $0.50R_{\mathrm{max}}$, yellow: $0.25R_{\mathrm{max}}$, and blue: R_{1kpc}). The evolution of these parameters was obtained by using an interpolation done by BAGPIPES to predict the physical quantities for redshifts from $z_{\mathrm{obs}} \approx 0.0136$ to $z = 10$.

2006). When analysing the WHAN diagram (Figure 4.24 our results are consistent with a Seyfert AGN for the inner apertures, while the outer apertures are located in the "weak AGN" region.

Finally, Figure 4.25 shows the radial profiles of the M_*, SFR, t_{form}, t_{quench} and τ_{quench}. In this figure we present data from the broad-band SED fitting method (black symbols) and the SED fitting of the IFS (red symbols) data. Also, for the M_* and SFR we show the empirical results based on the $g - i$ color mass-to-light ratio profile and the FUV surface brightness profile. These are our main results:

- The M_* profile from the IFS analysis matches pretty well the empirical profile obtained through the Taylor *et al.* (2015) method. However, it disagrees with the broad-band fitting results which is above by ~ 0.5 dex.

- The resulting SFR profile from the IFS analysis matches pretty well the empirical profile obtained from Kennicutt (1998), both display a nearly flat profile. Similarly as above, the broad-band fitting has a more complex shape than the other two: it increases from the initial aperture until it
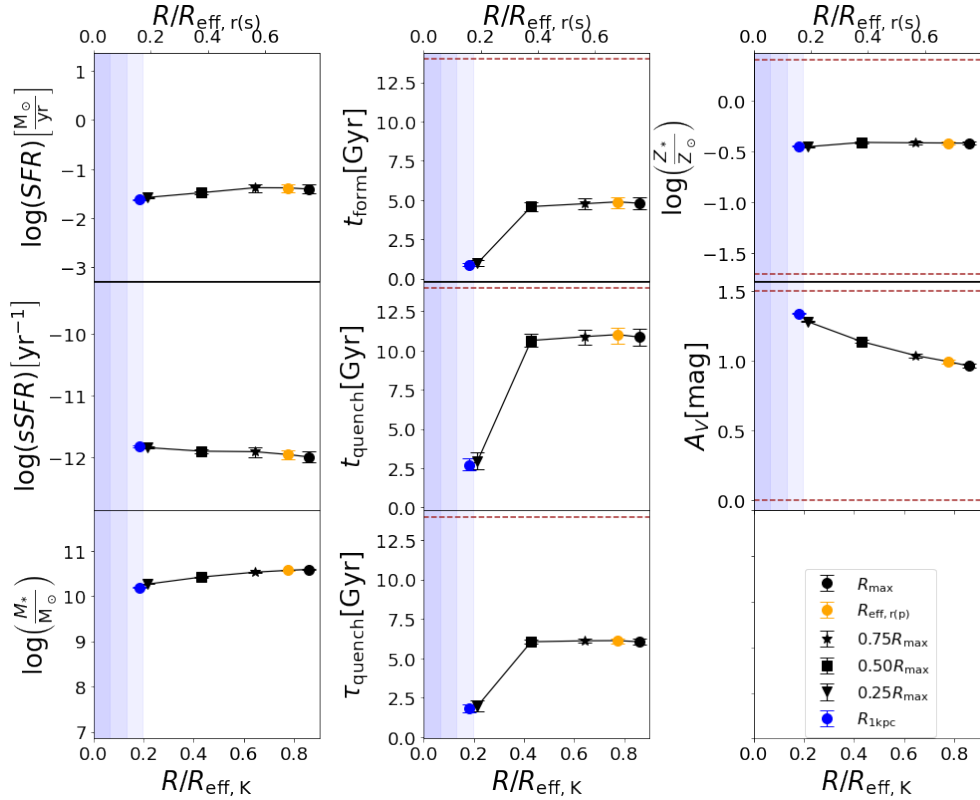
Figure 4.21: NGC1194 parameter radial profiles. The description is similar to Figure 4.3. Each aperture is represented by a different marker (black circle: R_{max}, yellow circle: $R_{eff,r(p)}$, black star: $0.75R_{max}$, black square: $0.50R_{max}$, black triangle: $0.25R_{max}$, and blue circle: R_{1kpc}). In this case, the uncertainties of most of the parameters are very small, in consequence their error bars are negligible.

reaches a maximum value of ~ 1 $M_\odot/yr$ at an aperture of $\sim 0.4 \times R_{eff,K}$; then for outer apertures, it decreases to values less than 10^{-3} $M_\odot/yr$.

- The time scales obtained from the IFS analysis tends at large radii to a value of $t_{form} \approx 5$ Gyr, $t_{quench} \approx 11$ Gyr and $\tau_{quench} \approx 6$ Gyr. These results are in apparent tension with the broad band fittings. While in principle our SED fitting to the IFS data should be obviously a far superior analysis than the broad-band SED fitting one, both results are in general consistent between each other and within the errors (in particular the formation time, quenching time and quenching time scale).
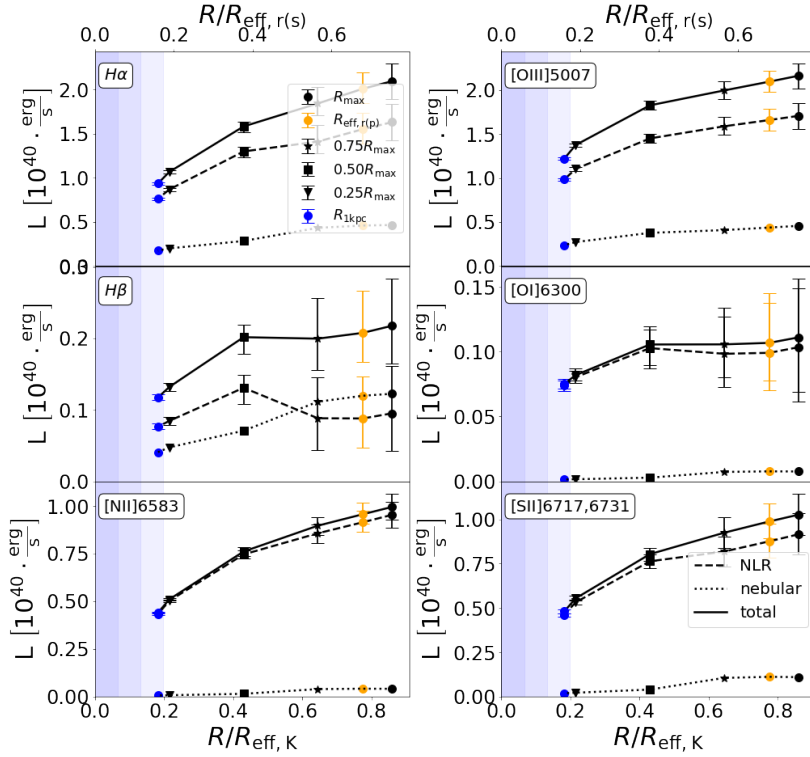
Figure 4.22: NGC1194 emission line luminosity profiles. The description is similar to Figure 4.4. Each aperture is represented by a different marker (black circle: R_{max}, yellow circle: $R_{\mathrm{eff,r(p)}}$, black star: $0.75R_{\mathrm{max}}$, black square: $0.50R_{\mathrm{max}}$, black triangle: $0.25R_{\mathrm{max}}$, and blue circle: R_{1kpc}).
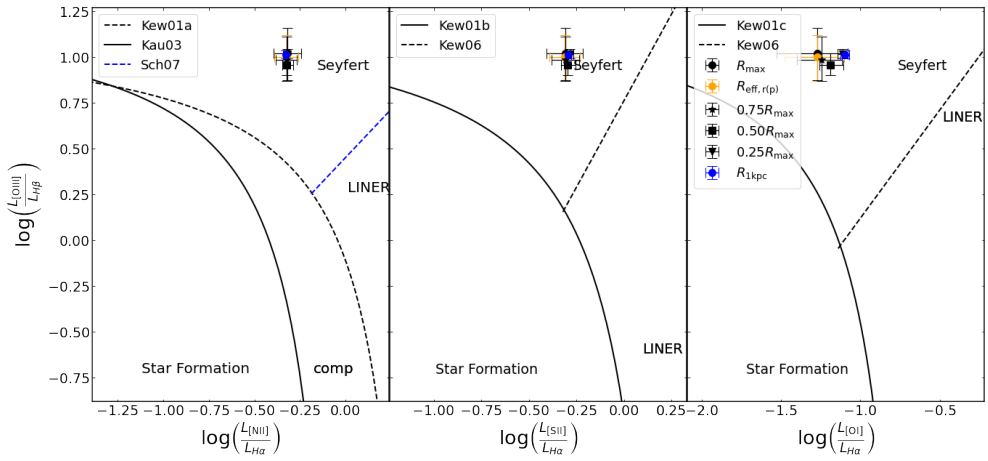
Figure 4.23: NGC1194 in BPT diagram. The description is similar to Figure 4.5. Each aperture is represented by a different marker (black circle: R_{max}, yellow circle: $R_{eff,r(p)}$, black star: $0.75R_{max}$, black square: $0.50R_{max}$, black triangle: $0.25R_{max}$, and blue circle: R_{1kpc}). All the analyzed apertures were located in the Seyfert region of the three diagrams.
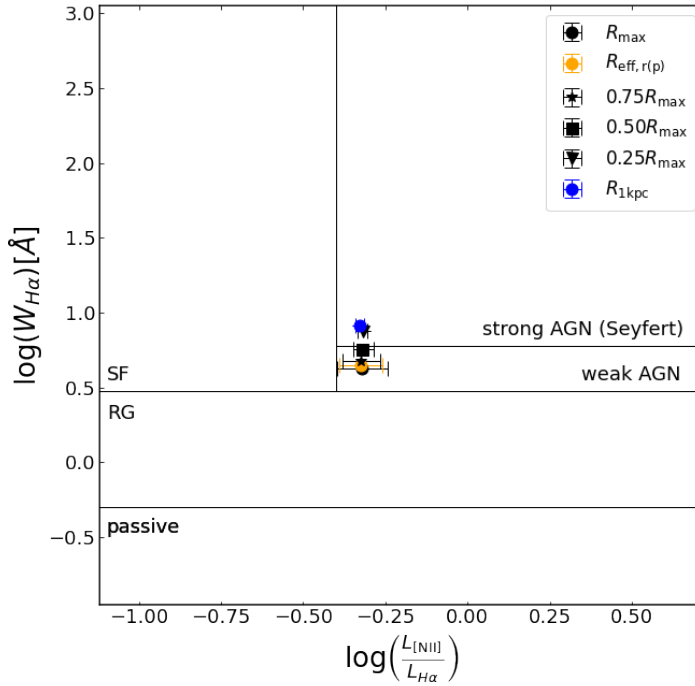
Figure 4.24: NGC1194 in the WHAN diagram. The description is similar to Figure 4.6. Each aperture is represented by a different marker (black circle: R_{max}, yellow circle: $R_{\mathrm{eff,r(p)}}$, black star: $0.75R_{\mathrm{max}}$, black square: $0.50R_{\mathrm{max}}$, black triangle: $0.25R_{\mathrm{max}}$, and blue circle: R_{1kpc}). The inner apertures, R_{1kpc} and $0.25R_{\mathrm{max}}$, were located in the Seyfert region, while the outer apertures were located in the "weak AGN" region.

Figure 4.25: NGC1194 parameter radial profiles. The description is similar to Figure 4.9, but for this galaxy the photometric profile (black line) is shown.

4.4   NGC6086

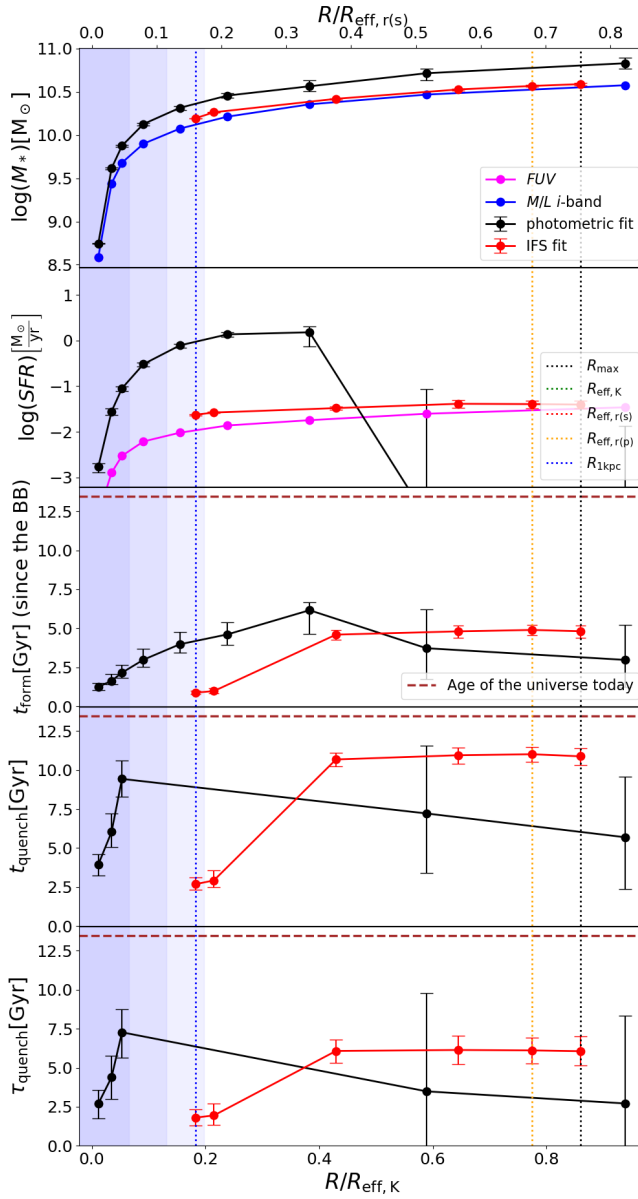NGC6086 is the only galaxy in our sample that is not reported as hosting an AGN and it does not exhibit emission lines nor radio emission, but it has a faint UV nuclear emission. It is the most *massive galaxy*, in stellar mass terms and at the same time is the host of the *largest* SMBH from our sample ($M_{\mathrm{BH}} \sim 3.7 \times 10^9$ M$_\odot$), in addition NGC6086 is the Brightest Cluster Galaxy (BCG) in the Abell 2162 cluster. These facts make NGC6086 an interesting laboratory for studying how massive BCGs and SMBH co-evolved over a long period of time by looking into the assembly history of the galaxy. Table 4.4 shows the different apertures where we performed the SED fitting to the IFS data, with their corresponding reduced χ^2.

Aperture	$R/R_{\mathrm{eff},K}$	$\chi^2/$d.o.f.
R_{max}	0.494	2.00
$R_{\mathrm{eff,r(p)}}$	0.486	2.05
$0.75R_{\mathrm{max}}$	0.371	3.17
$0.5R_{\mathrm{max}}$	0.247	5.84
$0.25R_{\mathrm{max}}$	0.124	12.69
R_{1kpc}	0.063	19.43

Table 4.4: Apertures of NGC6086 ranked in decreasing order of their size and their corresponding reduced χ^2.

Similarly to Figure 4.1, Figure 4.26 shows the observed SED fitting to the IFS data of NGC6086 for the maximum aperture. We notice that NGC6068 does not show any obvious contribution from an AGN to the SED. Indeed, the SED of this galaxy fits into the prototype of a classical BCG. In addition, there are no reports about this galaxy related to an AGN activity. In general, by observing the residuals, we found that our best fitting models reproduce the observations reasonably well, despite the slightly large reduced χ^2s in the smallest apertures R_{1kpc} and $0.25R_{\mathrm{max}}$.

Figure 4.27 shows the SFH and the SMFH while Figure 4.28 shows the radial parameters of the stellar population for NGC6086. All the analyzed apertures have a formation time of $z \sim 7 - 9$ ($\sim$13 Gyr ago) and a quenching redshift of $z \gtrsim 5$ according to the Pacifici criteria and at $z \gtrsim 3$ according to BAGPIPES. From this figure, we notice that NGC6086 formed from the inside-out in a less than 1 Gyr after the BB, and also got quenched relatively quickly, in less than 1.5 Gyr.

This massive early-type galaxy seems to be also an interesting candidate for a descendent of quiescent galaxies at $z > 3$ (Carnall *et al.*, 2023a). As discussed in Chapter 5 it seems unlikely that its SMBH was the reason this
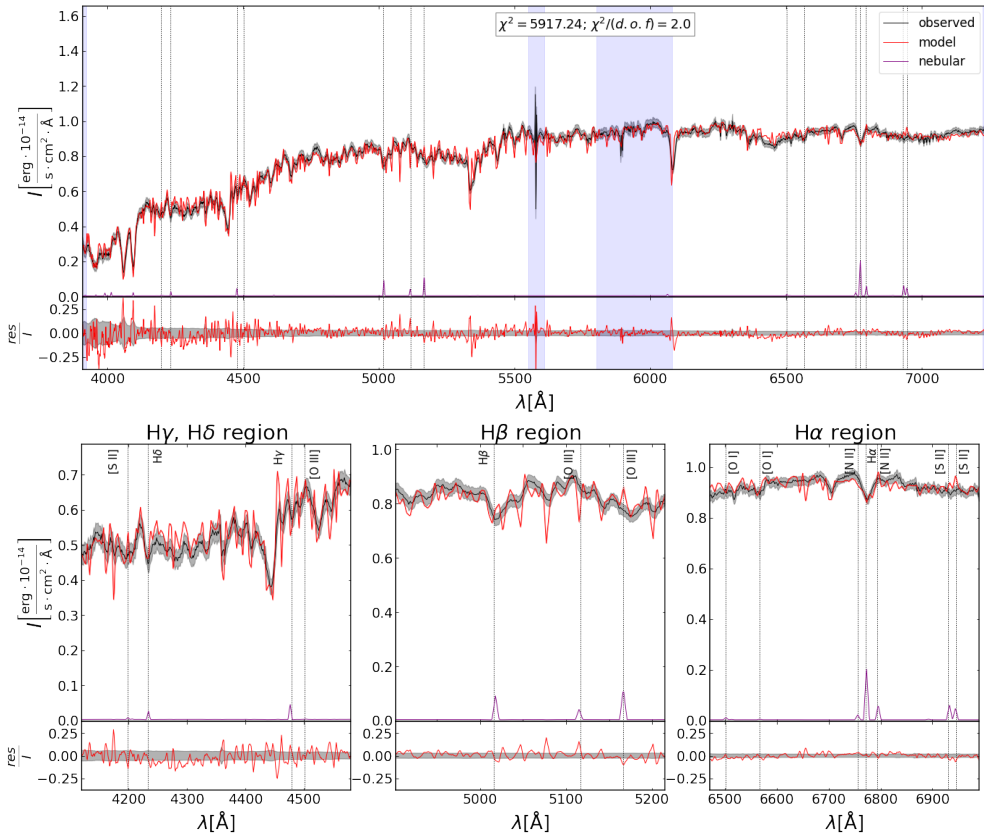
Figure 4.26: Spectral fit of NGC6086 at the maximum aperture. The description is similar to Figure 4.1. The spectrum is at the observed frame ($z_{\mathrm{obs}} = 0.0319$).

galaxy quenched $\sim$2 Gyr after the BB in the first place. This time-scale is too early and before the appearance of the most powerful QSOs/AGNs. Most likely, NGC6068's BH feedback has been the mechanism that has kept the galaxy quenched.

Finally, Figure 4.29 shows and compares both, the profiles obtained through the SED fitting to the IFS data and the SED broad-band fitting. In addition, similarly to the previous galaxies we use the $g - i$ color profile and the mass-to-light ratios dependency on color to compute a photometric mass as well as the SFR from the FUV integrated profile. When comparing these different estimations we found that:

- The M_* inferred from the SED fitting to the IFS data for the apertures larger than 3PSF (R_{max} and $R_{\mathrm{eff,r(p)}}$), is in good agreement with the one obtained from the broad-band fitting analysis as well as with the empirical
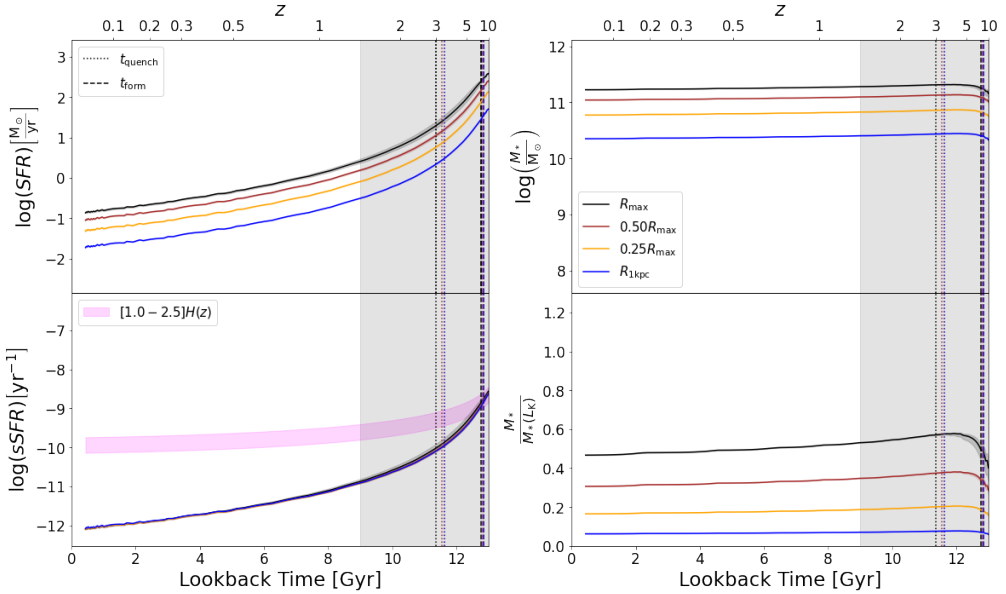
Figure 4.27: Evolution of NGC6086. The description is similar to Figure 4.2. Each aperture is represented by a different color (black: R_{max}, red: $0.50R_{max}$, yellow: $0.25R_{max}$, and blue: R_{1kpc}). The evolution of these parameters was obtained by using an interpolation done by BAGPIPES to predict the physical quantities for redshifts from $z_{obs} \approx 0.0319$ to $z = 10$.

one obtained through the Taylor *et al.* (2015) method.

- The SFR inferred from the SED fitting to the IFS data is consistent with the empirical one obtained through the Kennicutt (1998) empirical method. Both SFR profiles are consistent with a nearly constant SFR profile. In contrast the broad-band fitting results increase from the initial aperture until a maximum value of ~ 10 M$_\odot$/yr is reached, at an aperture of $\sim 0.2 \times R_{eff,K}$ (outer than 3PSF); then it decreases to values less than 10^{-3} M$_\odot$/yr. The above tension could be the result of hot evolved stellar types as we discuss below.

- The time-scales obtained through the IFS analysis have the following values for the outer apertures: $t_{form} \approx 0.5$ Gyr, $t_{quench} \approx 2.0$ Gyr and $\tau_{quench} \approx 1.5$ Gyr. As discussed above, this implies that NGC6068 formed early in the universe but also quenched early. On the other hand, the broad-band fitting analysis shows that NGC6068 is young in the centre and older in the outskirts. Moreover, the broad-band fitting analysis also points out that this galaxy is still star forming in the centre but quenched in the outskirts. Recall that in quiescent galaxies, which are
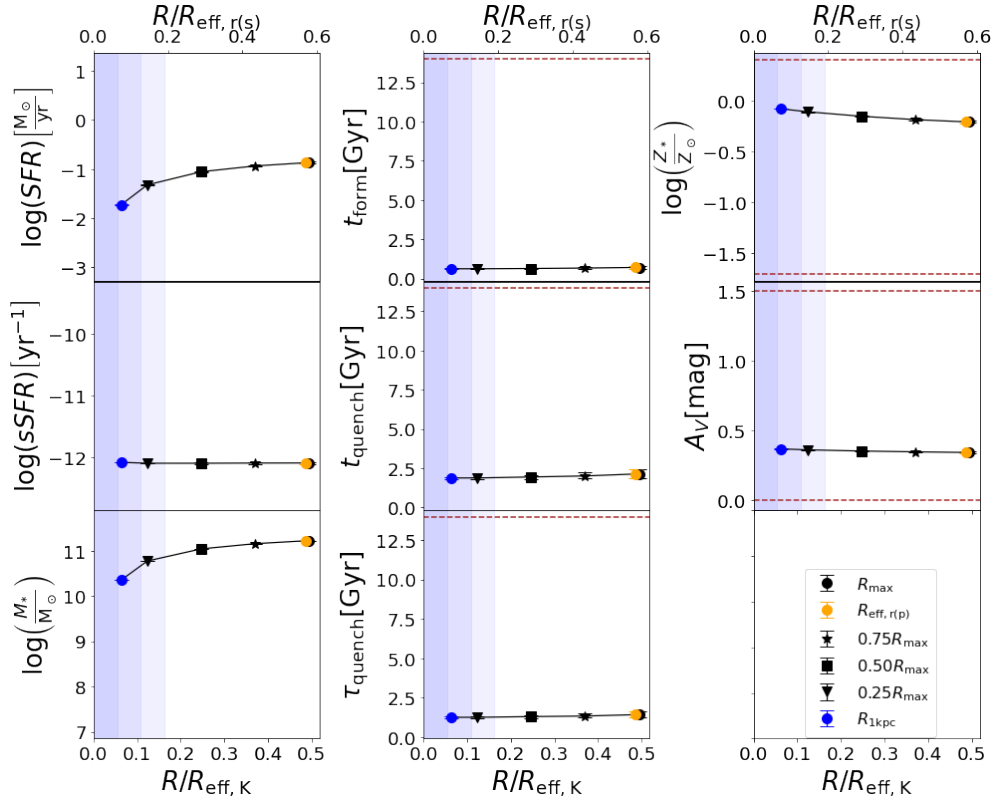
Figure 4.28: NGC6086 parameter radial profiles. The description is similar to Figure 4.3. Each aperture is represented by a different marker (black circle: R_{max}, yellow circle: $R_{\mathrm{eff,r(p)}}$, black star: $0.75R_{\mathrm{max}}$, black square: $0.50R_{\mathrm{max}}$, black triangle: $0.25R_{\mathrm{max}}$, and blue circle: R_{1kpc}). In this case, the uncertainties of all the parameters are very small, in consequence their error bars are negligible.

composed mostly by old stellar populations, UV emission can be due to hot evolved stellar types, such as post–asymptotic giant branch (AGB) and extreme horizontal branch (HB) stars (see the reviews by O'Connell, 1999; Conroy, 2013). Most likely, due to the limitations of the broad-band fitting analysis, this method may confuses the UV emission coming from young hot massive stars.
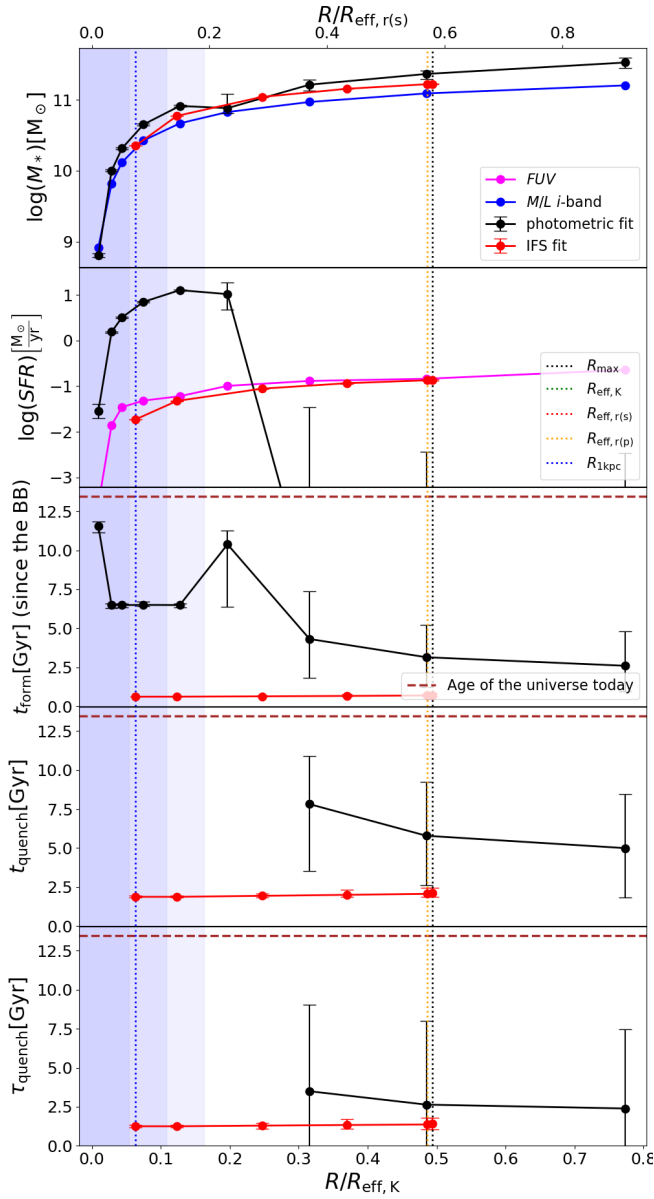
Figure 4.29: NGC6086 parameter radial profiles. The description is similar to Figure 4.9, but for this galaxy the photometric profile (black line) is shown.

4.5 NGC3982

NGC3982 is a member of a nearby group of galaxies, with an excess UV emission in all the spiral structure of its disk and a significant nuclear radio emission. It has been classified as a Seyfert 2 according to the Véron-Cetty & Véron (2006) catalog and there are not hints of a BLR for this AGN, for this reason we only model the NLR from the AGN. The Figure 4.30 shows the observed SED fitting to the IFS data of NGC3982 for the $R_{\max}$ aperture, which was particularly challenging; observe the relative large reduced chi-squares for each aperture (see Table 4.5 and Appendix A). Nonetheless, we notice that errors in the best model fitting are lower than $\sim 10\%$ for most of the spectrum.

Aperture	$R/R_{\mathrm{eff},K}$	χ^2/d.o.f.
$R_{\max}$	0.863	11.52
$R_{1\mathrm{kpc}}$	0.698	11.50
$0.75R_{\max}$	0.647	10.99
$0.5R_{\max}$	0.432	8.24
$0.25R_{\max}$	0.216	14.58

Table 4.5: Apertures of NGC3982 ranked in decreasing order of their size and their corresponding reduced χ^2.

Our results regarding the AGN emission line models show that that when assuming the same width for every emission line of the NLR, our models reproduce moderately well their line profiles. The above might be because the width of these lines are at the limit of the spectral resolution of MaNGA and are thus not well resolved.

NGC3982 is an interesting case because it hosts a massive SMBH for its mass and velocity dispersion and it is also extremely compact (see Figure 2.2). Figure 4.31 shows that the above peculiarities contrast with the observed extended period over which NGC3982 has remained as a star forming galaxy in its central part. We speculate more about the evolution of NGC3982 and its relation with the AGN in the Discussion (Chapter 5). Briefly, we mention that similarly to Mrk290, it is likely that NGC3982 AGN is being fed by gas of low angular momentum.

Figure 4.32 shows the the radial parameters of the stellar population of NGC3982. From the parameters of the fitted narrow lines we derive their fluxes (see figure 4.33). Then, by using the ratio of these fluxes, we were able to locate the radiation from the different apertures of the galaxy, in the BPT and the WHAN diagrams, as shown in Figures 4.34 and 4.35. We can not confirm that NGC3982 is a Seyfert AGN, since the radiation at the outer apertures ($R_{\max}$, $R_{1\mathrm{kpc}}$ and $0.75R_{\max}$) has been located out of the Seyfert region of the three
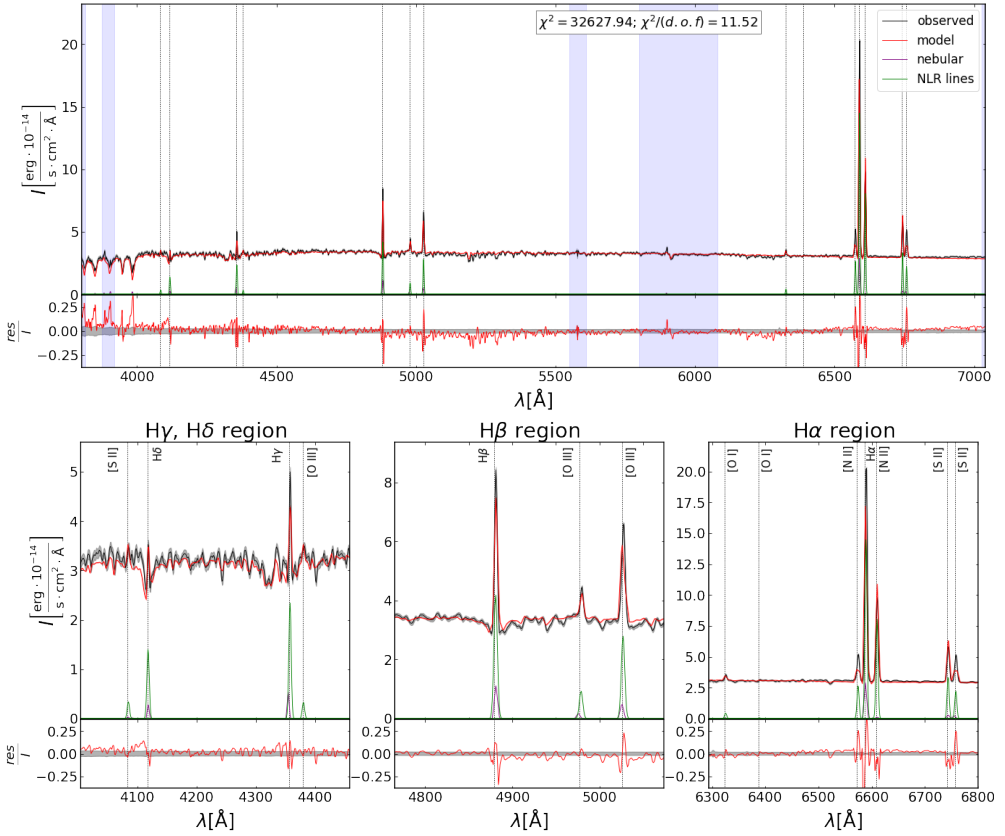
Figure 4.30: Spectral fit of NGC3982 at the maximum aperture. The description is similar to Figure 4.1. The spectrum is at the observed frame ($z_{\mathrm{obs}} = 0.0037$).

BPT diagrams: in the [NII] one the ratios of the different apertures are located in the composite region, while in [SII] and [OI] diagrams the ratios are in the SF region. In the other hand, the radiation of the inner apertures ($0.5R_{\mathrm{max}}$ and $0.25R_{\mathrm{max}}$) is located in the Seyfert region of the BPT diagrams, and actually the radiation of all the apertures is located in the Seyfert region of the WHAN diagram. We must take this with caution, considering that the emission lines were not very well fitted because of the spectral resolution.

Finally, in Figure 4.36 the profiles obtained from the SED fitting to the IFS data and the SED broad-band fitting are shown by the black and red solid lines, similar to Figure 4.9, but for NGC3982. For this galaxy it was not possible to obtain the empirical profile of SFR through Kennicutt (1998) method, due to the the lack of data for the UV surface brightness profiles. We thus caution that the results from the broad-band fitting obtained for this galaxy should be taken with care. The general results for this galaxy are:
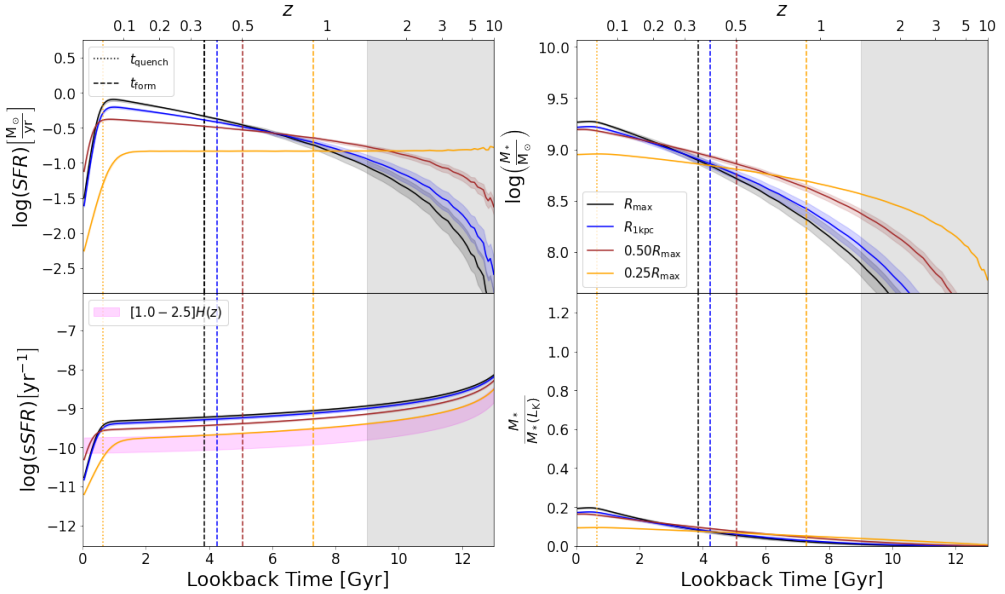
Figure 4.31: Evolution of NGC3982. The description is similar to Figure 4.2. Each aperture is represented by a different color (black: R_{max}, blue: R_{1kpc}, red: $0.50R_{max}$, and yellow: $0.25R_{max}$). The evolution of these parameters was obtained by using an interpolation done by BAGPIPES to predict the physical quantities for redshifts from $z_{obs} \approx 0.0037$ to $z = 10$.

- The M_* inferred from the IFS analysis is consistent with the empirical profile. The profile obtained from the SED broad-band analysis is larger by ~ 0.2 dex.

- The SFR profiles disagree between each other. The the broad-band fitting result is above the IFS results for more than ~ 1 dex.

- The formation time obtained through the IFS analysis is $t_{form} \approx 10$ Gyr for the R_{max} aperture while the broad-band results tends to an older formation time of $t_{form} \approx 7$ Gyr. Recall that we did not include ultraviolet light in our broad-band fitting analysis which could explain why we obtained older populations compared to the spectroscopic results.

Figure 4.32: NGC3982 parameter radial profiles. The description is similar to Figure 4.3. Each aperture is represented by a different marker (black circle: R_{max}, blue circle: R_{1kpc}, black star: $0.75R_{\mathrm{max}}$, black square: $0.50R_{\mathrm{max}}$, and black triangle: $0.25R_{\mathrm{max}}$). In this case, the uncertainties of all the parameters are very small, in consequence their error bars are negligible.
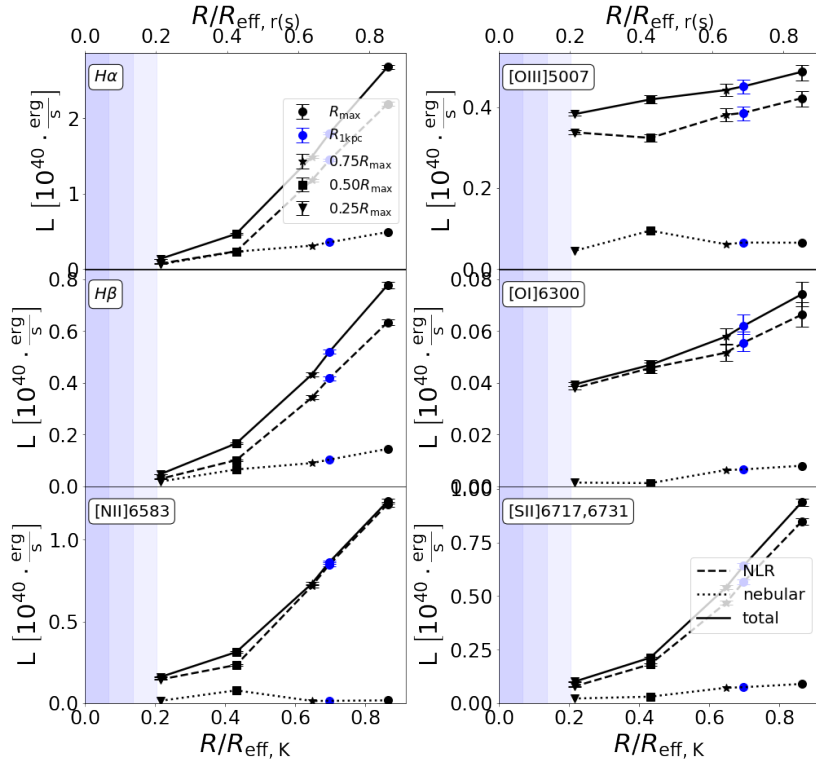
Figure 4.33: NGC3982 emission line luminosity profiles. The description is similar to Figure 4.4. Each aperture is represented by a different marker (black circle: R_{max}, blue circle: R_{1kpc}, black star: $0.75R_{max}$, black square: $0.50R_{max}$, and black triangle: $0.25R_{max}$).
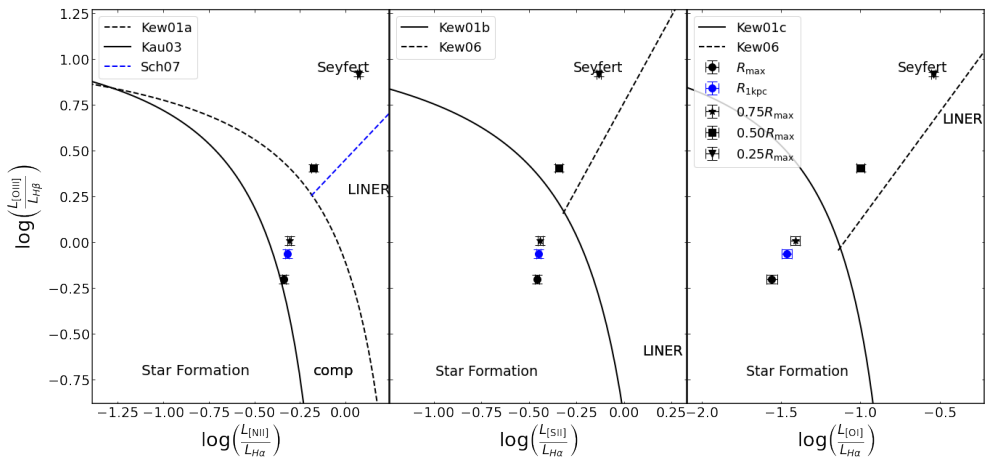
Figure 4.34: NGC3982 in BPT diagram. The description is similar to Figure 4.5. Each aperture is represented by a different marker (black circle: R_{max}, blue circle: R_{1kpc}, black star: $0.75R_{max}$, black square: $0.50R_{max}$, and black triangle: $0.25R_{max}$). The inner apertures, $0.25R_{max}$ and $0.50R_{max}$, were located in the Seyfert region.
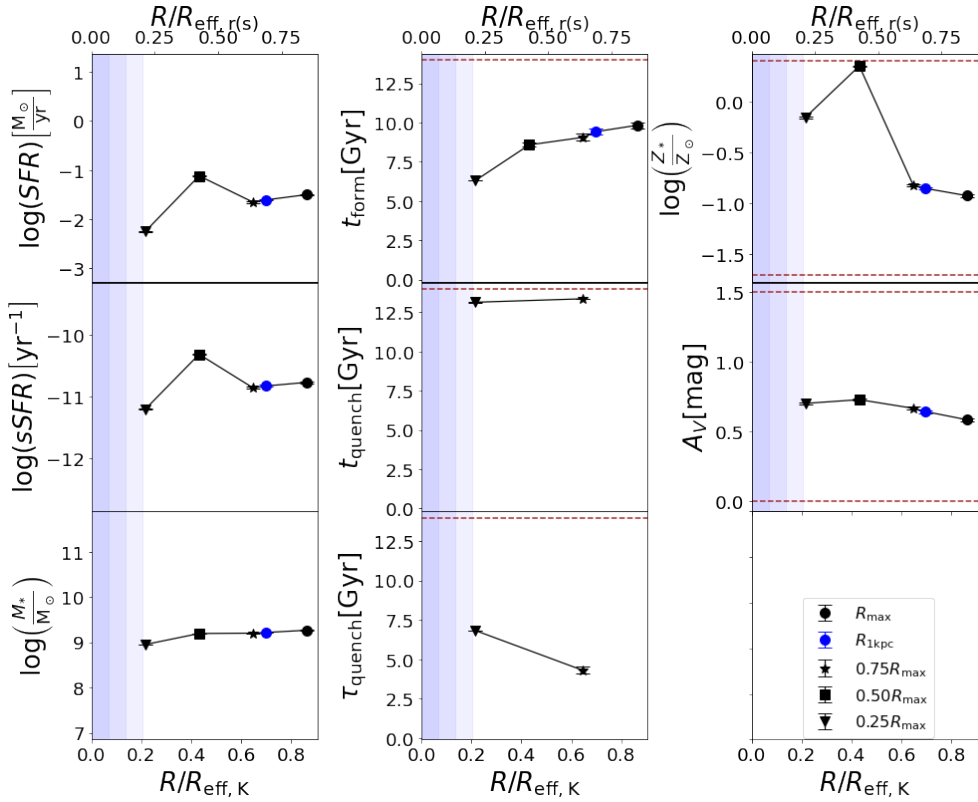
Figure 4.35: NGC3982 in the WHAN diagram. The description is similar to Figure 4.6. Each aperture is represented by a different marker (black circle: R_{max}, blue circle: R_{1kpc}, black star: $0.75R_{max}$, black square: $0.50R_{max}$, and black triangle: $0.25R_{max}$). All the analyzed apertures were located in the Seyfert region.

Figure 4.36: NGC3982 parameter radial profiles. The description is similar to Figure 4.9, but for this galaxy the photometric profile (black line) is shown, while the empirical profile of the SFR obtained from the FUV is not shown, due to the lack of the UV data.

4.6   NGC2960

This galaxy is a well known LINER (Véron-Cetty & Véron, 2006) and there are not hints of a BLR for this AGN. It exhibits a significant nuclear emission in radio, together with a faint UV emission, consistent with its Markarian classification. Figure 4.37 show the observed SED of NGC2960 and our best fitting model, together with the separated contribution from nebular emissions, and the NLR from the AGN. Even, when modelling the nebular and the NLR contribution Hβ, Hγ and Hδ show absorption profiles at every aperture. Our SED fittings to the IFS data resulted in very acceptable values for the reduced χ^2, except for the inner aperture $R = R_{1\mathrm{kpc}}$ (see Table 4.6).
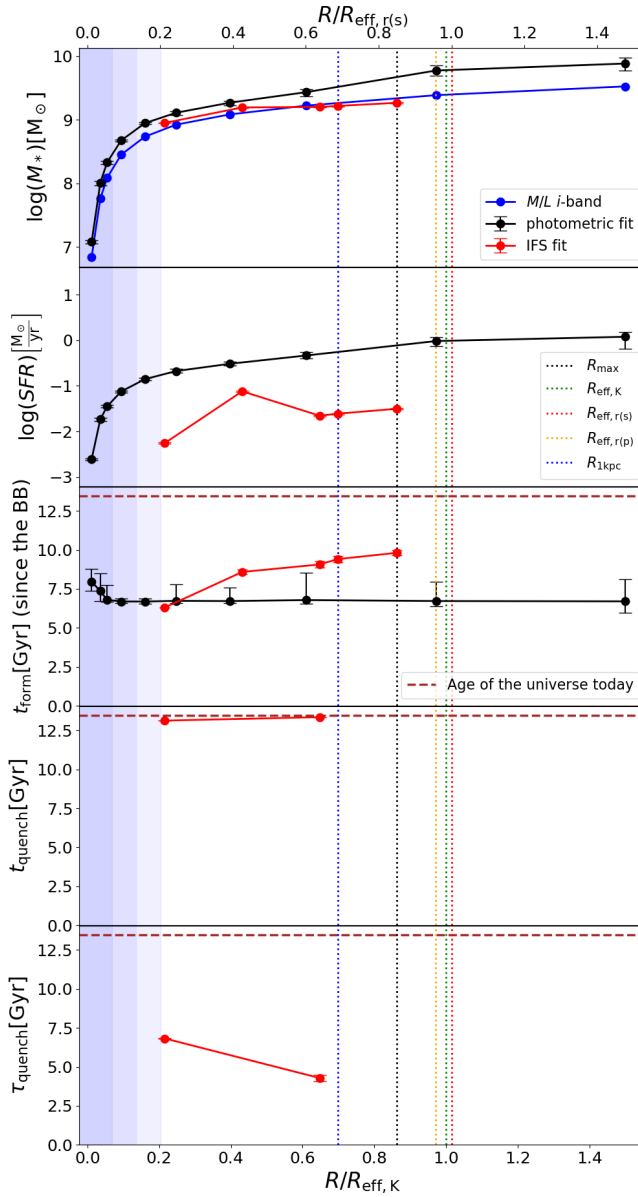
Aperture	$R/R_{\mathrm{eff},K}$	χ^2/d.o.f.
$R_{\max}$	0.901	1.19
$R_{\mathrm{eff,r(p)}}$	0.746	1.56
$0.75R_{\max}$	0.676	2.01
$0.5R_{\max}$	0.451	3.92
$0.25R_{\max}$	0.225	9.75
$R_{1\mathrm{kpc}}$	0.186	11.47

Table 4.6: Apertures of NGC2960 ranked in decreasing order of their size and their corresponding reduced χ^2.

Figure 4.38 shows the SFH and the SMFH for NGC2960. $R_{1\mathrm{kpc}}$ is the innermost aperture of all and its SFH peaks at a very recent epoch of $z \lesssim 0.1$ ($\lesssim 1$ Gyr ago), and it also formed very recently at $z \sim 0.3$ (~ 3.5 Gyr ago). We also found that the star formation decreases abruptly after the peak of SF, and according to the Pacifici criteria and BAGPIPES, it has quenched, recently, ~ 0.5 Gyr ago. As for the outer apertures, the stellar populations have even a more recent formation time and quenching time according to the Pacifici criteria. We notice however that for the BAGPIPES criteria these apertures remain as star forming. More discussion and speculations about NGC2960 evolution and the effects of the AGN on its SFH by feedback process, are in Chapter 5.

Figure 4.39 shows the radial parameter profiles and it can be noticed that this galaxy has slightly suppressed its central part and it is more metallic at the outskirts. In addition, it looks like NGC2960 has assembled from the inside-out, and the inner aperture is the only one that has been quenched very recently.

From the parameters of the fitted narrow lines we derive their luminosities (see Figure 4.40). Then, by using the ratio of these luminosities, we were able to locate the radiation from the different apertures of the galaxy, in the BPT diagrams, as shown in figure 4.41. We can not completely conclude that NGC2960 is a Seyfert AGN, since the only apertures located in the Seyfert
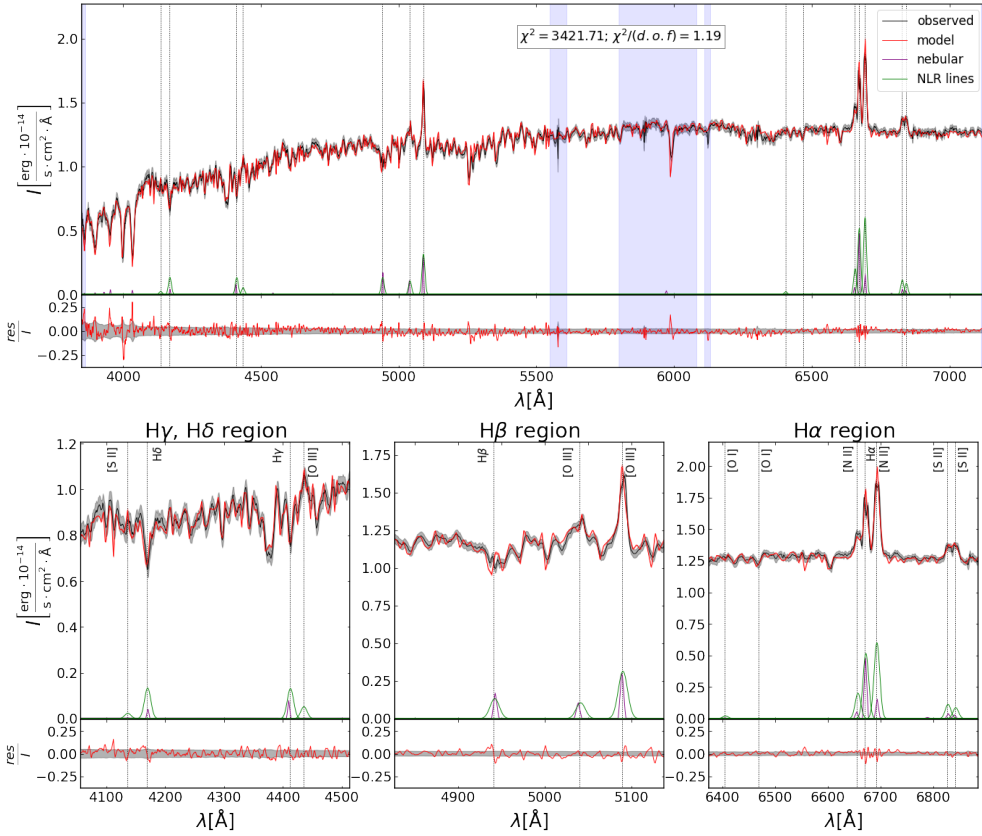
Figure 4.37: Spectral fit of NGC2960 at the maximum aperture. The description is similar to Figure 4.1. The spectrum is at the observed frame ($z_{\mathrm{obs}} = 0.0165$).

region of the three BPT diagrams are the innermost ones, R_{1kpc}, $0.25R_{\mathrm{max}}$ and $0.50R_{\mathrm{max}}$, the other ones are in the LINER region for the [NII] diagram, and in the SF region for the [SII] and [OI] diagrams. Our LINER classification is consistent with the Véron-Cetty & Véron (2006) AGN catalog classification. In the other hand, all the apertures are located in the Seyfert region of the WHAN diagram, very close to the 'weak AGN' region (see Figure 4.42).

Finally, Figure 4.43 shows and compares both, the profiles obtained through the SED fitting to the IFS data and the broad-band SED fitting, similar to Figure 4.9, but for NGC2960. The fitted profiles of M_* and SFR are also compared with the empirical profiles obtained through the surface brightness profile information. From this analysis we found that:

- The M_* inferred from the IFS analysis is in general consistent with both for the broad-band analysis results and the photometric mass from the
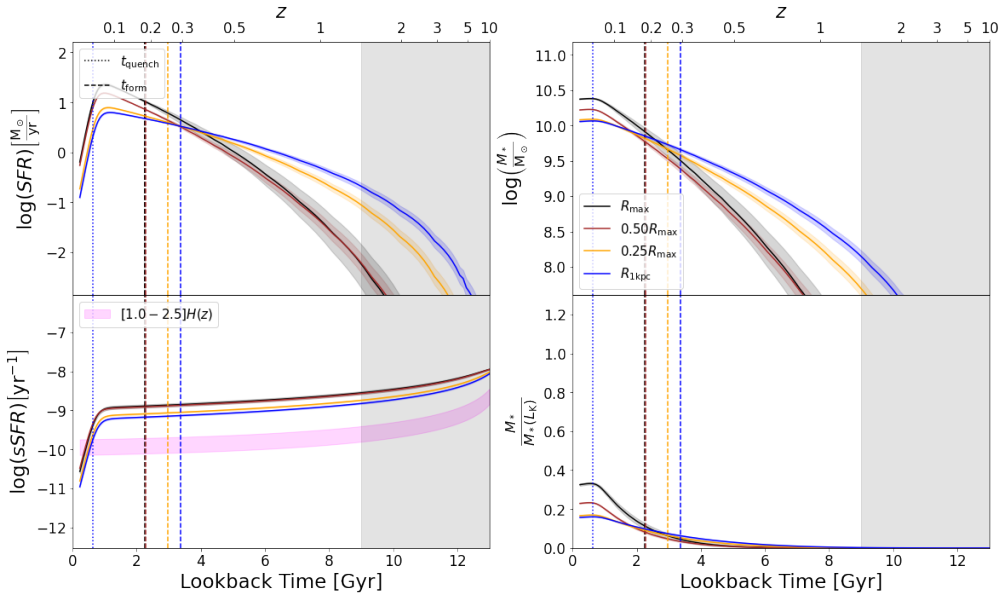
Figure 4.38: Evolution of NGC2960. The description is similar to Figure 4.2. Each aperture is represented by a different color (black: R_{max}, red: $0.50R_{\mathrm{max}}$, yellow: $0.25R_{\mathrm{max}}$, and blue: R_{1kpc}). The evolution of these parameters was obtained by using an interpolation done by Bagpipes to predict the physical quantities for redshifts from $z_{\mathrm{obs}} \approx 0.0165$ to $z = 10$.

color dependent mass-to-light ratios. At larger apertures we find that the broad-band results tend to predict more M_*.

- The SFR inferred from the IFS analysis is consistent with the broad band fitting results below $R_{\mathrm{eff,r(p)}}$; also the empirical method is below the other two determinations. Above that radius the broad-band fitting results tend to be by a couple of orders of magnitude below the IFS results.

- We find that for both, the spectroscopic analysis and the photometric analysis yield consistent values for t_{form} below $R_{\mathrm{eff,r(p)}}$. Notice that the spectroscopic analysis shows that the galaxy is older in the centre but younger in the outskirts. On the contrary, the photometric analysis shows a younger centre but older outskirts. It is interesting that the photometric analysis points out to a larger effect of the AGN if we interpret the strong suppression of SFR in the most inner parts. Indeed, the central part seems to have quenched just recently (less than 0.5 Gyr ago) with a quenching time-scale of ~ 2.5 Gyr as suggested by the bottom panel.
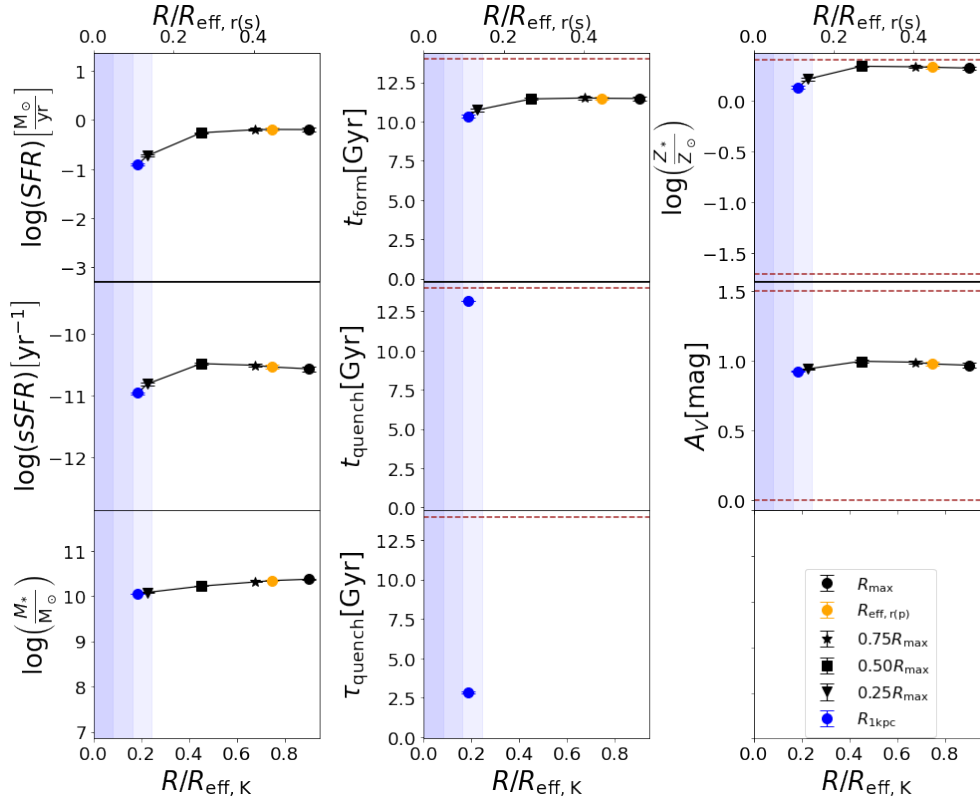
Figure 4.39: NGC2960 parameter radial profiles. The description is similar to Figure 4.3. Each aperture is represented by a different marker (black circle: R_{max}, yellow circle: $R_{eff,r(p)}$, black star: $0.75R_{max}$, black square: $0.50R_{max}$, black triangle: $0.25R_{max}$, and blue circle: R_{1kpc}). In this case, the uncertainties of all the parameters are very small, in consequence their error bars are negligible, also the only aperture that has been quenched is R_{1kpc} so it is the only one with t_{quench} reported.
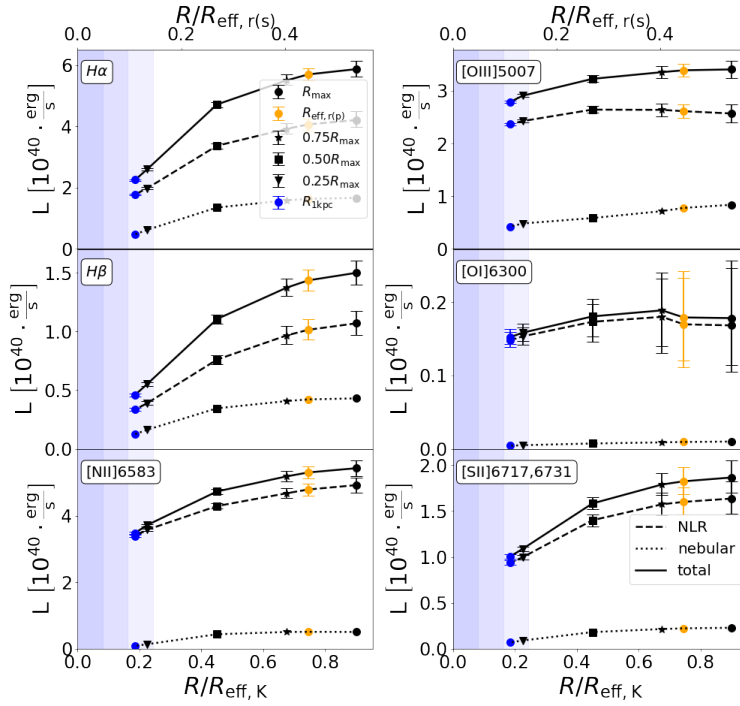
Figure 4.40: NGC2960 emission line luminosity profiles. The description is similar to Figure 4.4. Each aperture is represented by a different marker (black circle: R_{max}, yellow circle: $R_{eff,r(p)}$, black star: $0.75R_{max}$, black square: $0.50R_{max}$, black triangle: $0.25R_{max}$, and blue circle: R_{1kpc}).
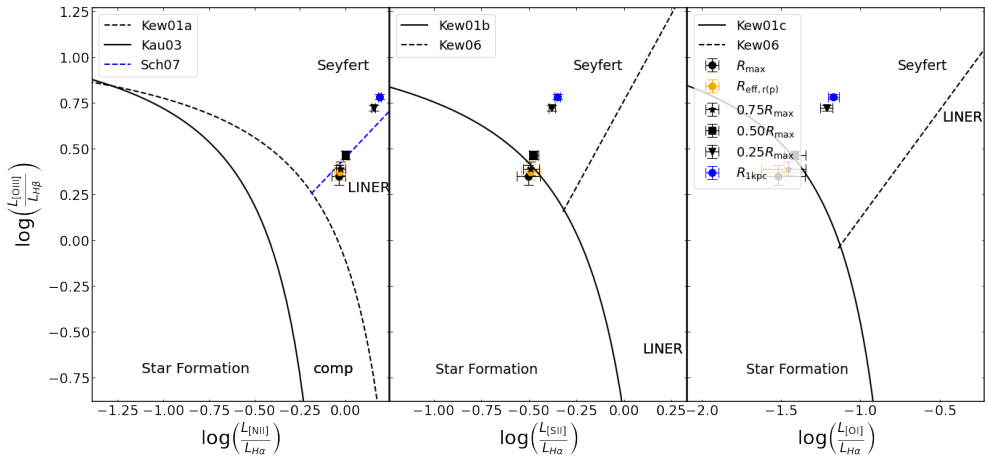
Figure 4.41: NGC2960 in BPT diagram. The description is similar to Figure 4.5. Each aperture is represented by a different marker (black circle: R_{max}, yellow circle: $R_{eff,r(p)}$, black star: $0.75R_{max}$, black square: $0.50R_{max}$, black triangle: $0.25R_{max}$, and blue circle: R_{1kpc}). The radiation coming from the innermost apertures, R_{1kpc}, $0.25R_{max}$ and $0.50R_{max}$, is located in the Seyfert region of the three diagrams, while the other ones are in the LINER region of the [NII] diagram and in the SF region of the [SII] and [OI] diagrams.
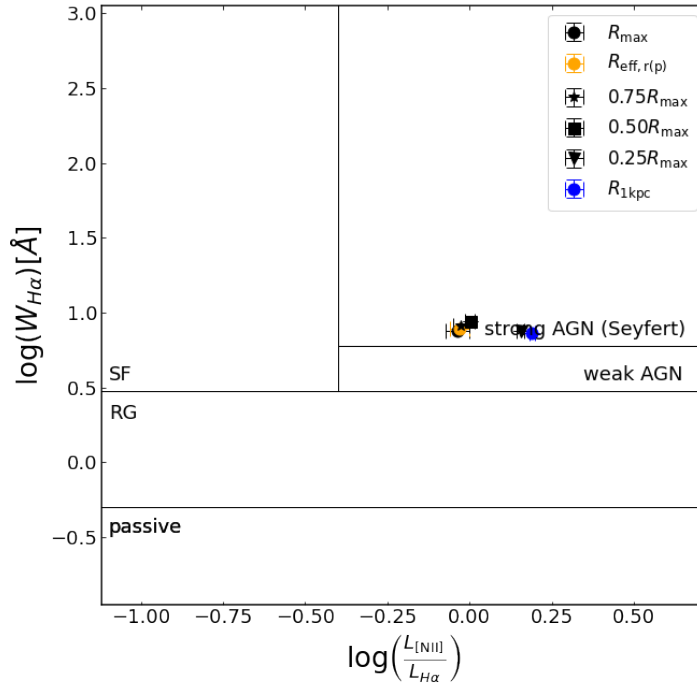
Figure 4.42: NGC2960 in the WHAN diagram. The description is similar to Figure 4.6. Each aperture is represented by a different marker (black circle: R_{max}, yellow circle: $R_{\mathrm{eff,r(p)}}$, black star: $0.75R_{\mathrm{max}}$, black square: $0.50R_{\mathrm{max}}$, black triangle: $0.25R_{\mathrm{max}}$, and blue circle: R_{1kpc}). All the analyzed apertures were located in the Seyfert region, very close to the 'weak AGN' region.
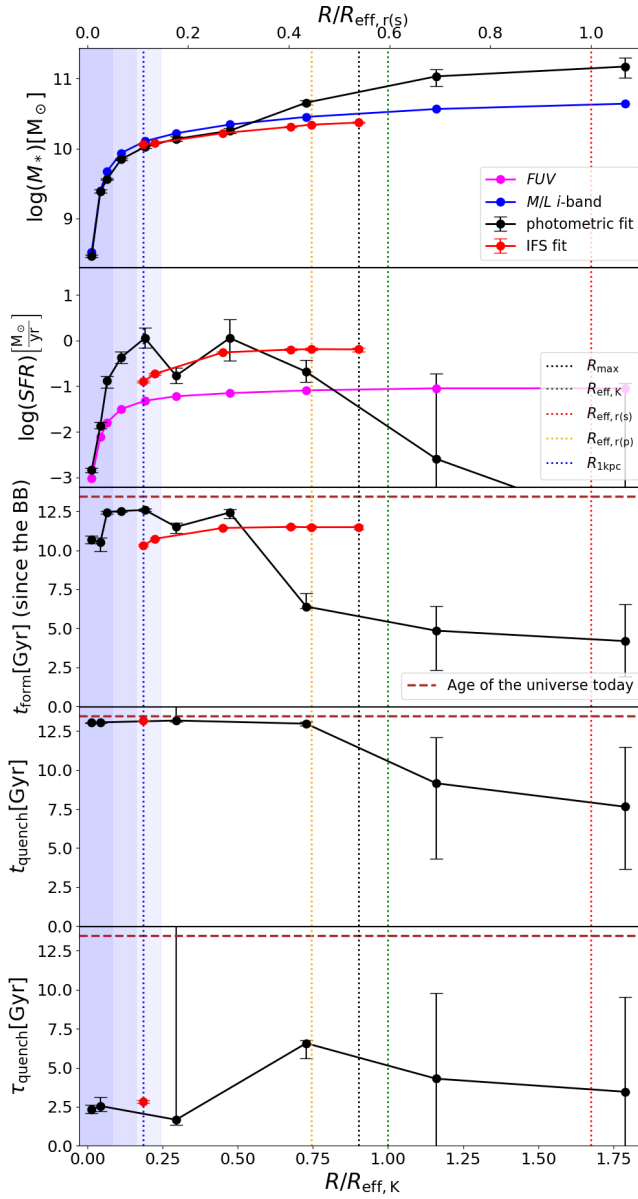
Figure 4.43: NGC2960 parameter profiles. The description is similar to Figure 4.9, but for this galaxy the photometric profile (black line) is shown.

4.7 NGC6264

NGC6264 is a Seyfert 2 galaxy, with no hints of a BLR. It has been identified as a member of a WBL nearby poor cluster of galaxies and it exhibits a faint UV nuclear emission but it does not have radio emission. Figure 4.44 presents the SED fitting to the IFS data for the maximum aperture that could fit inside the FoV, R_{max}. As in the previous cases, we decomposed our theoretical SED into the different components that we included, in particular, the bottom panels show a zoom-in into the regions where the emission from the AGN and nebular lines are comparable. We found that our best fitting models reproduce the observed SED reasonably well for most of the apertures. The smallest aperture R_{1kpc}, which is near the PSF radii, has the largest reduced χ^2, see Table 4.7.

Aperture	$R/R_{\mathrm{eff},K}$	χ^2/d.o.f.
R_{max}	1.292	1.58
$R_{\mathrm{eff},K}$	1.00	2.47
$0.75R_{\mathrm{max}}$	0.969	2.83
$R_{\mathrm{eff,r(p)}}$	0.919	2.94
$0.5R_{\mathrm{max}}$	0.646	5.88
$0.25R_{\mathrm{max}}$	0.323	9.43
R_{1kpc}	0.109	16.96

Table 4.7: Apertures of NGC6264 ranked in decreasing order of their size and their corresponding reduced χ^2.

Figure 4.45 shows the SFH and the SMFH for NGC6264. The inner apertures are R_{1kpc}, $0.25R_{\mathrm{max}}$ and $0.50R_{\mathrm{max}}$, and their SFHs peaks at very early epochs ($z > 10$). Their formation times occurred at $z \sim 4 - 6$ ($\sim 12.0 - 12.5$ Gyr ago), and have been quenched almost since the beginning of their evolutionary histories according to the Pacifici criteria, but at $z \sim 1 - 2$ ($\sim 8.0 - 10.5$ Gyr ago) according to BAGPIPES. Recall that the results of R_{1kpc} should be taken carefully since it is near 1PSF. In the other hand, the outer apertures seem to point out that the galaxy is quenching from the inside-out, the above will be more evident by studying the stellar properties as a function to their galactocentric distance.

NGC6264 is the prototype galaxy which has a very typical size and BH mass for it stellar mass. It assembled from the inside-out but also quenched from the inside-out, as discussed above. Figure 4.46 present the stellar population properties of NGC6264 as a function of the galactocentric distance. We notice that there is an abrupt change below $\sim R_{\mathrm{eff},K}$ in all of its stellar parameters; the SFR drops, the galaxy is older and got quenched $\sim 2.5 - 4.5$ Gyr after these apertures formed. Since NGC6264 has an AGN, it is not clear if it is responsible
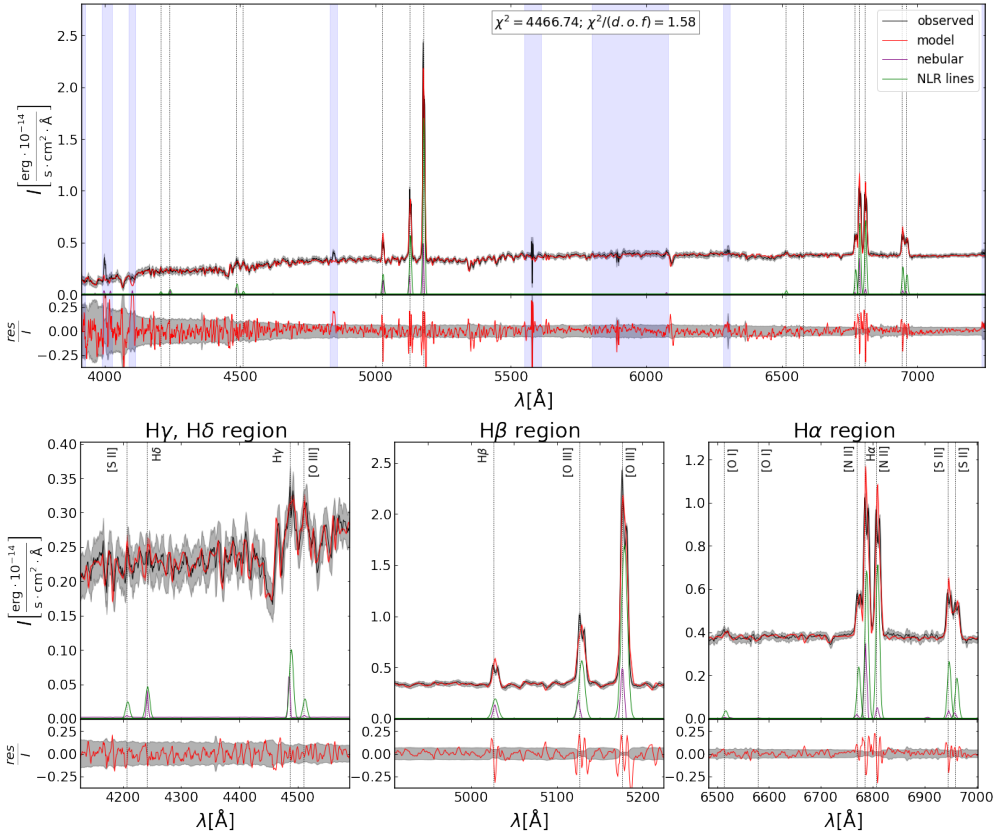
Figure 4.44: Spectral fit of NGC6264 at the maximum aperture. The description is similar to Figure 4.1. The spectrum is at the observed frame ($z_{\mathrm{obs}} = 0.0338$).

for the central shut-off of the galaxy since the galaxy properties and the BH mass are not different from those of a late-type galaxy. More details and some speculation about the processes around the evolution of NGC6264 are discussed in Chapter 5.

From the parameters of the fitted narrow lines we derive their luminosities (see figure 4.47). Then, by using the ratio of these luminosities, we were able to locate the radiation from the different apertures of the galaxy, in the BPT diagrams, as shown in Figure 4.48, and in the WHAN diagram, as shown in Figure 4.49. We confirm that NGC6264 is a Seyfert AGN, since the radiation at all apertures has been located on the Seyfert region of the three BPT diagrams and of the WHAN diagram.

Finally, Figure 4.50 shows the results for the broad-band fits and compares to the spectroscopic analysis, in addition, the fitted profiles of M_* and SFR are also compared with the empirical profiles (FUV and M/L $i\text{-}band$) obtained
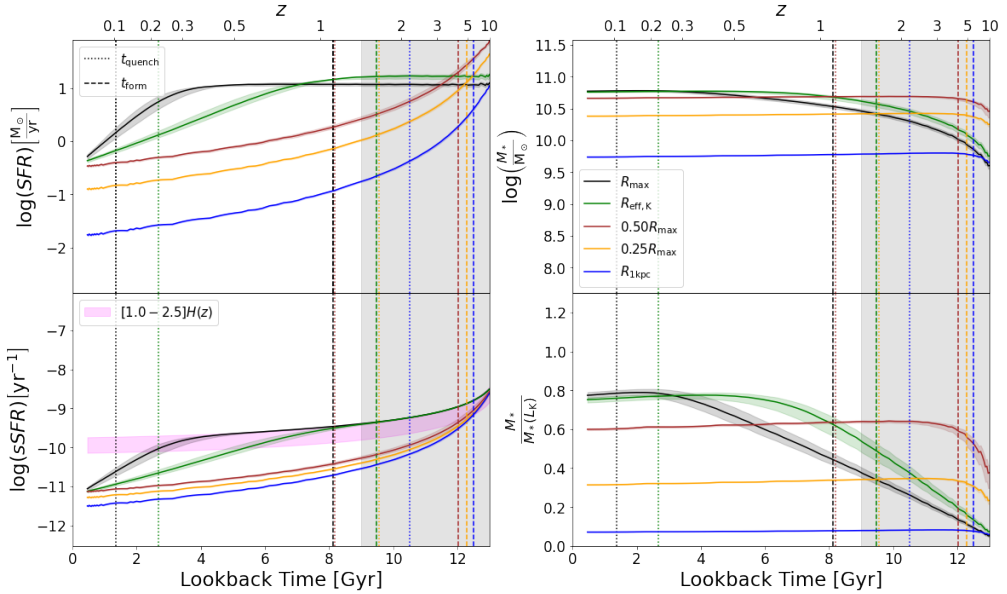
Figure 4.45: Evolution of NGC6264. The description is similar to Figure 4.2. Each aperture is represented by a different color (black: R_{max}, green: $R_{eff,K}$, red: $0.50R_{max}$, yellow: $0.25R_{max}$, and blue: R_{1kpc}). The evolution of these parameters was obtained by using an interpolation done by BAGPIPES to predict the physical quantities for redshifts from $z_{obs} \approx 0.0338$ to $z = 10$.

through the surface brightness profile information. From this analysis we notice that the IFS apertures are larger than the photometrical ones. The main results we highlight are:

- Our results show that the various stellar mass profiles that we derived are consistent between each other. The stellar mass profile derived from the mass-to-light ratio seems to be the one underestimating the mass at large radii.

- The empirical and the SED fitting to the IFS data derived SFR profiles that are in good agreement. The broad-band derived SFR profile is almost an order of magnitude larger than the other two. Recall that in quiescent galaxies, UV radiation from evolved stars can be confused as a trace of star formation. This may be the case for our broad-band fitting analysis.

- The broad band fitting results in formation times show that the stellar population of NGC6264 is younger in the centre and older in the out-skirts and star forming. In contrast, the spectroscopic analysis is more
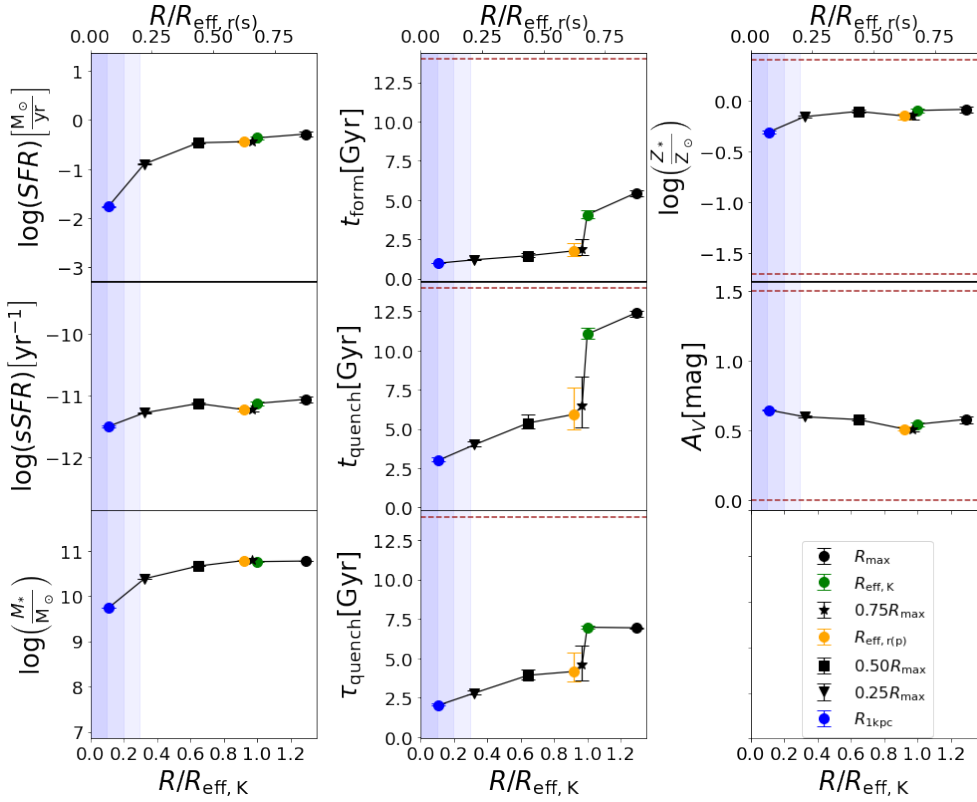
Figure 4.46: NGC6264 parameter radial profiles. The description is similar to Figure 4.3. Each aperture is represented by a different marker (black circle: R_{max}, green circle: $R_{eff,K}$, black star: $0.75R_{max}$, yellow circle: $R_{eff,r(p)}$, black square: $0.50R_{max}$, black triangle: $0.25R_{max}$, and blue circle: R_{1kpc}). In this case, the uncertainties of most of the parameters are very small, in consequence their error bars are negligible.

consistent with an inside-out growth and inside-out quenching. The above might be the result of the UV radiation confusion problem from evolved stars.
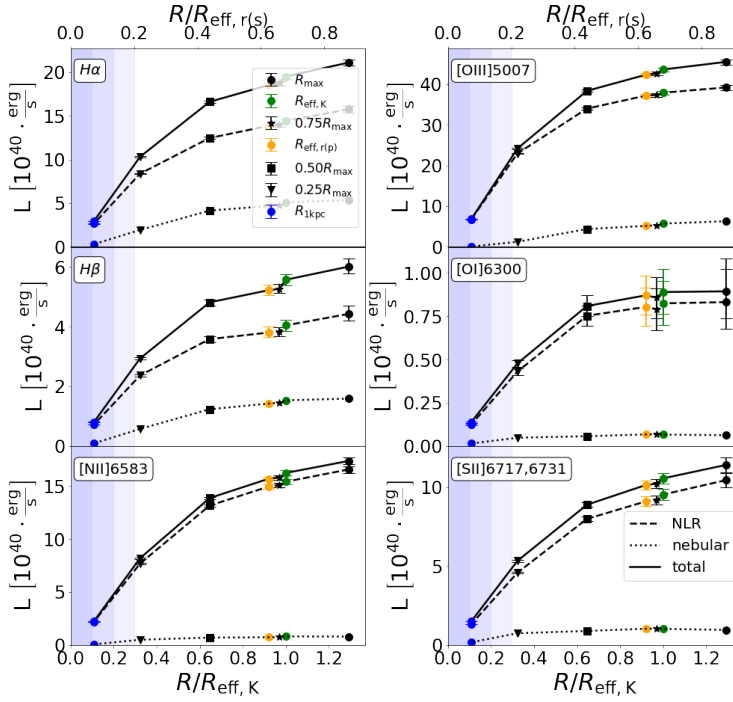
Figure 4.47: NGC6264 emission line luminosity profiles. The description is similar to Figure 4.4. Each aperture is represented by a different marker (black circle: R_{max}, green circle: $R_{\mathrm{eff},K}$, black star: $0.75R_{\mathrm{max}}$, yellow circle: $R_{\mathrm{eff,r(p)}}$, black square: $0.50R_{\mathrm{max}}$, black triangle: $0.25R_{\mathrm{max}}$, and blue circle: R_{1kpc}).
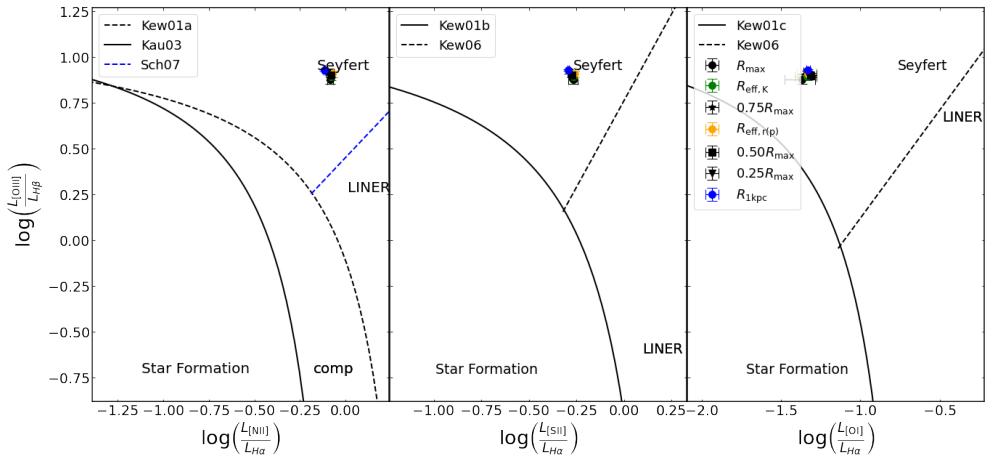
Figure 4.48: NGC6264 in BPT diagram. The description is similar to Figure 4.5. Each aperture is represented by a different marker (black circle: R_{max}, green circle: $R_{eff,K}$, black star: $0.75R_{max}$, yellow circle: $R_{eff,r(p)}$, black square: $0.50R_{max}$, black triangle: $0.25R_{max}$, and blue circle: R_{1kpc}). All the analyzed apertures were located in the Seyfert region of the three diagrams.
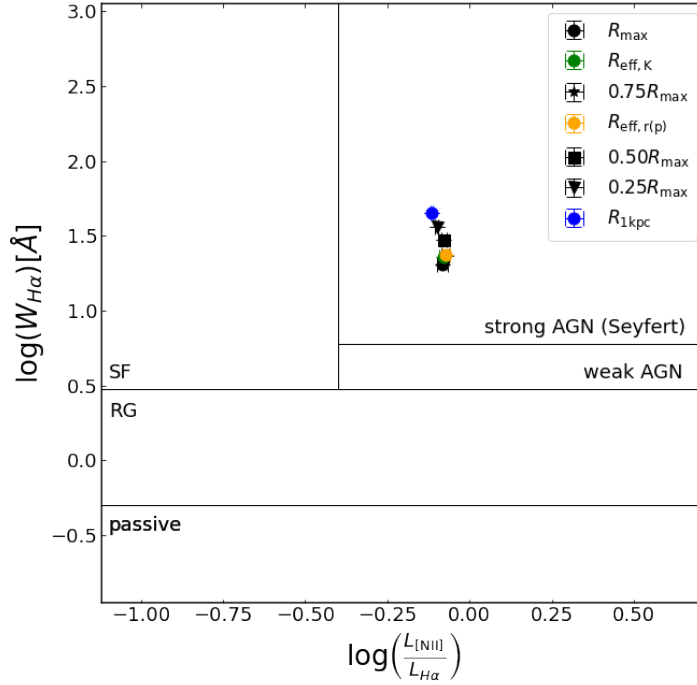
Figure 4.49: NGC6264 in the WHAN diagram. The description is similar to Figure 4.6. Each aperture is represented by a different marker (black circle: R_{max}, green circle: $R_{\mathrm{eff},K}$, black star: $0.75R_{\mathrm{max}}$, yellow circle: $R_{\mathrm{eff},r(p)}$, black square: $0.50R_{\mathrm{max}}$, black triangle: $0.25R_{\mathrm{max}}$, and blue circle: R_{1kpc}). All the analyzed apertures were located in the Seyfert region.
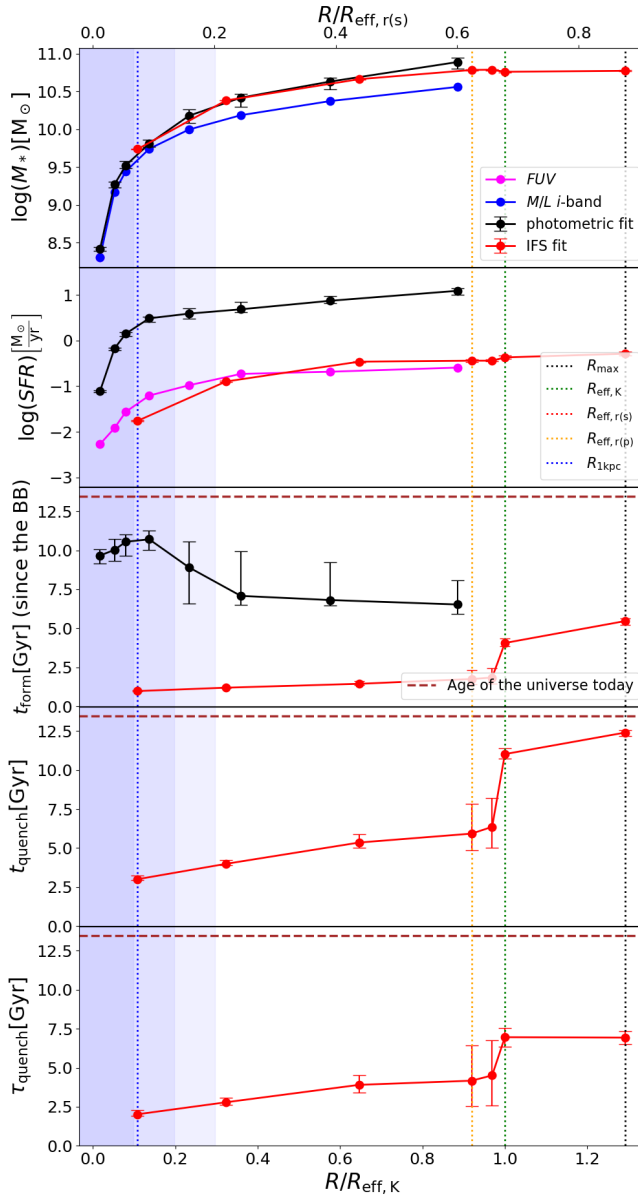
Figure 4.50: NGC6264 parameter radial profiles. The description is similar to Figure 4.9, but for this galaxy the photometric profile (black line) is shown.

4.8 NGC4395

This galaxy is nearest ($z \approx 0.0011$) and the less massive galaxy in our sample, both in terms of M_* and M_{BH}. It is a well known narrow line AGN with no evident hints of a BLR, having an excess of UV nuclear emission, but no radio emission. NGC4395 has been identified as a member of a nearby group of galaxies, and it has been noticed that the FoV of MaNGA encloses only a central star cluster, instead of the majority of the galaxy. There are only four apertures analyzed for NGC4395; these are R_{max}, $0.75R_{max}$, $0.50R_{max}$ and $0.25R_{max}$, with reduced chi-squares enlisted in Table 4.8. Figure 4.44 shows the observed SED and the separated contribution from nebular emissions and the NLR from the AGN. The bottom panels are a zoom-in into the regions of interest for the BLR and nebular emissions.

Aperture	$R/R_{\mathrm{eff},K}$	χ^2/d.o.f.
$R_{\max}$	0.289	14.77
$0.75R_{\max}$	0.216	27.59
$0.5R_{\max}$	0.144	58.17
$0.25R_{\max}$	0.072	154.29

Table 4.8: Apertures of NGC6264 ranked in decreasing order of their size and their corresponding reduced χ^2.

Our best fitting model reproduces the observed SED reasonably well, despite the slightly large reduced chi-square. Note, however, that the largest errors are of the order of 50% or less. We notice that our models poorly reproduce the profiles of the emission lines (see the residuals). They are very narrow, reaching the limit of MaNGA spectral resolution, and in consequence it is difficult to correctly model them.

Figure 4.52 shows the SFH and the SMFH for NGC4395. For all the apertures the peak of the SFH takes place at very early epochs. Their formation times were around $z \sim 1$. We also found that it has been a star forming galaxy based on both the Pacifici and BAGPIPES criteria, but only little above the threshold. This galaxy has a low BH mass for its stellar mass but a normal BH for its velocity dispersion. Also, we notice that this galaxy is small in size compared to its mass (see Figure 2.2).

Figure 4.53 present the stellar population properties of NGC4395 as a function of the galactocentric distance, where a positive gradient in the SFR is evident, while the $sSFR$ profile is almost flat. This galaxy has a high metallicity, converging to the maximum value of the prior distribution ($2.5\ Z_\odot$) for the innermost aperture and having a negative gradient until it reaches $\sim 1\ Z_\odot$ at the outermost aperture.
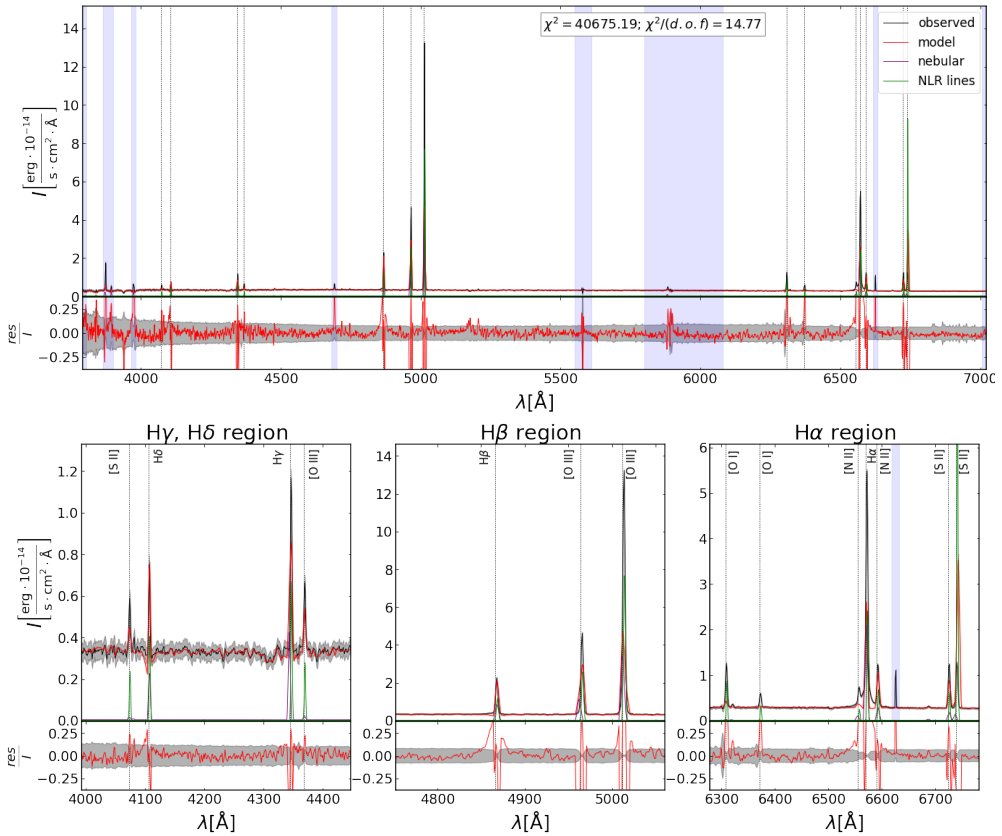
Figure 4.51: Spectral fit of NGC4395 at the maximum aperture. The description is similar to Figure 4.1. The spectrum is at the observed frame ($z_{\mathrm{obs}} = 0.0011$).

From the parameters of the fitted narrow lines we derive their luminosities (see Figure 4.54) and we were able to locate the radiation from the fitted apertures of the galaxy, in the BPT diagrams as shown in Figure 4.55, and in the WHAN diagram as shown in Figure 4.56. We cannot confirm that NGC4395 is a Seyfert AGN, since the radiation of the fitted apertures has been located on the Seyfert region of the [NII] and [OI] diagrams, while for the [SII] diagram the outermost aperture, R_{max}, gets in to the LINER region; even most, all the analyzed apertures get into the SF region of the WHAN diagram; this must be taken with caution, since the emission lines were not successfully fitted due to the spectral resolution, as mentioned above. Nonetheless, the AGN of this galaxy has been catalogued as Seyfert, see Véron-Cetty & Véron (2006).

Finally, Figure 4.57 present the derived photometric profiles for the M_*, SFR, t_{form}, t_{quench} and τ_{quench}. The profiles of M_* and SFR are also compared with the empirical profiles (FUV and M/L i-band) obtained through the surface
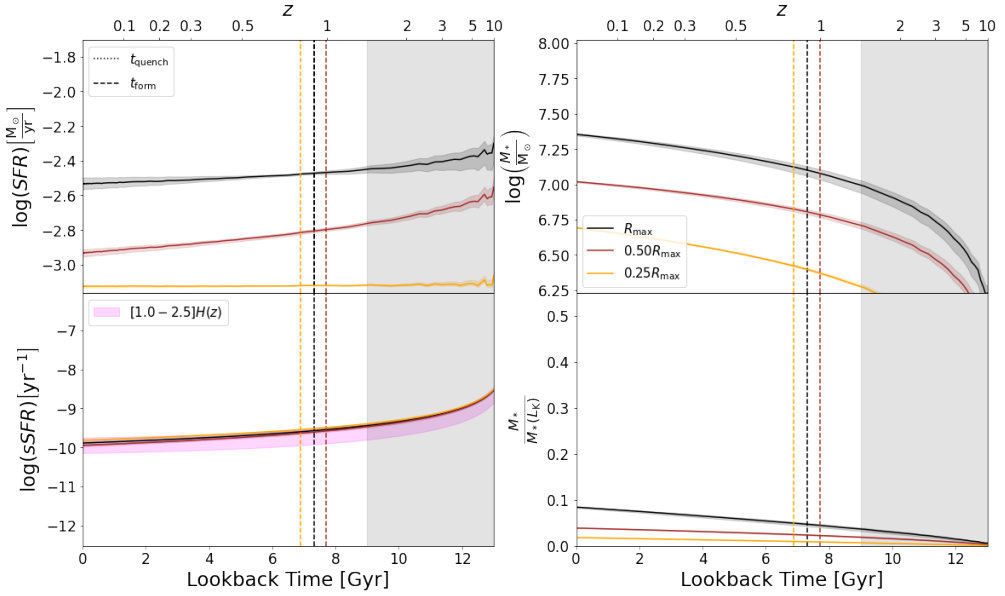
Figure 4.52: Evolution of NGC4395. The description is similar to Figure 4.2.Each aperture is represented by a different color (black: $R_{\max}$, red: $0.50R_{\max}$, and yellow: $0.25R_{\max}$). The evolution of these parameters was obtained by using an interpolation done by BAGPIPES to predict the physical quantities for redshifts from $z_{\rm obs} \approx 0.0011$ to $z = 10$.

brightness profile information. We found that the empirical, the IFS and the fitted broad-band M_* and SFR profiles of NGC4395 are in excellent agreement. For the broad-band results, Figure 4.57 shows that the central part is actively forming stars, which perhaps is not surprising given that the central SMBH is among the smallest reported in the literature; as a consequence of the SF activity in the centre, the galaxy is younger in the centre than in the outskirts. Perhaps, this galaxy is on the way to build a core and thus in the future will trigger the growth of its SMBH.

In Tables 4.9, 4.10 & 4.11 we provide a summary of the main results reported in the previous sections for the individual galaxies.
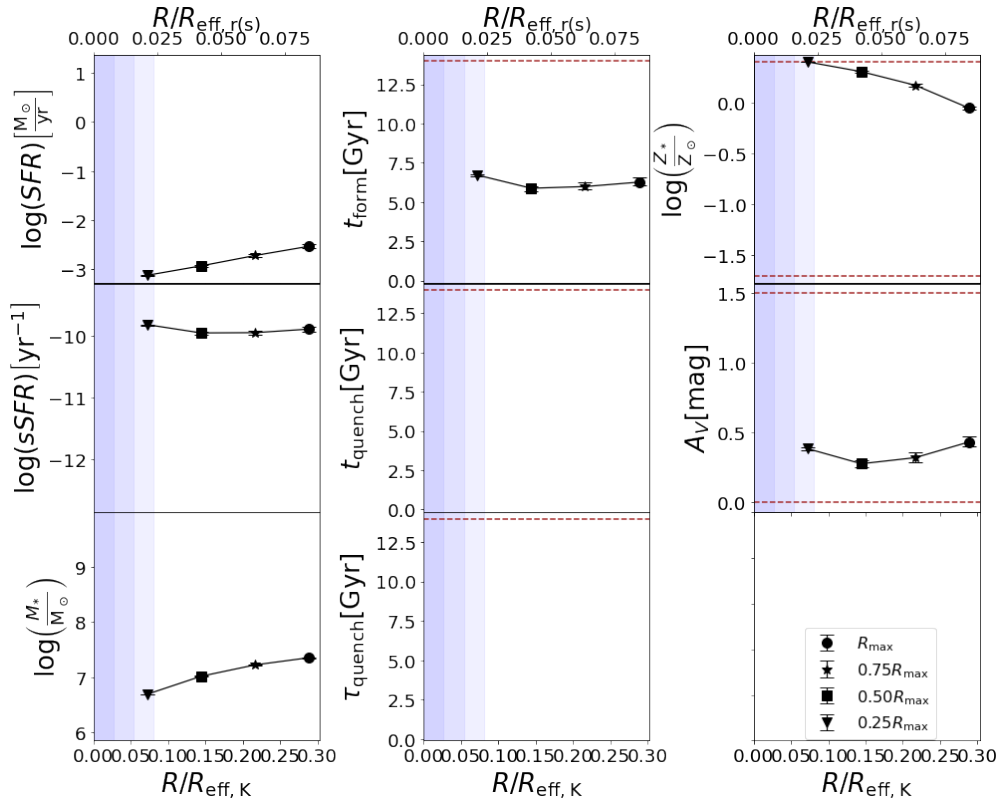
Figure 4.53: NGC4395 parameter radial profiles. The description is similar to Figure 4.3. Each aperture is represented by a different marker (black circle: R_{max}, black star: $0.75R_{\mathrm{max}}$, black square: $0.50R_{\mathrm{max}}$, and black triangle: $0.25R_{\mathrm{max}}$). In this case, the uncertainties of most of the parameters are very small, in consequence their error bars are negligible. There is no t_{quench} reported because the galaxy has not quenched yet, according to BAGPIPES criteria.
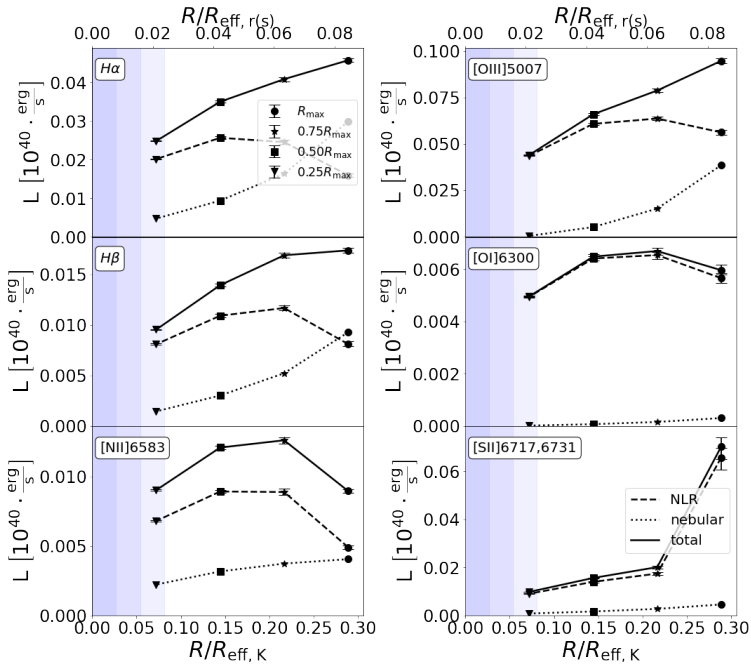
Figure 4.54: NGC4395 emission line luminosity profiles. The description is similar to Figure 4.4. Each aperture is represented by a different marker (black circle: R_{max}, black star: $0.75R_{max}$, black square: $0.50R_{max}$, and black triangle: $0.25R_{max}$).

Figure 4.55: NGC4395 in BPT diagram. The description is similar to Figure 4.5. Each aperture is represented by a different marker (black circle: R_{max}, black star: $0.75R_{max}$, black square: $0.50R_{max}$, and black triangle: $0.25R_{max}$). All the analyzed apertures get in to the Seyfert region for [N II] and [O I] diagrams, while for the [S II] diagram the outermost aperture, R_{max}, gets in to the LINER region. This must be taken with careful as the narrow emission lines were not well fitted due to the spectral resolution.
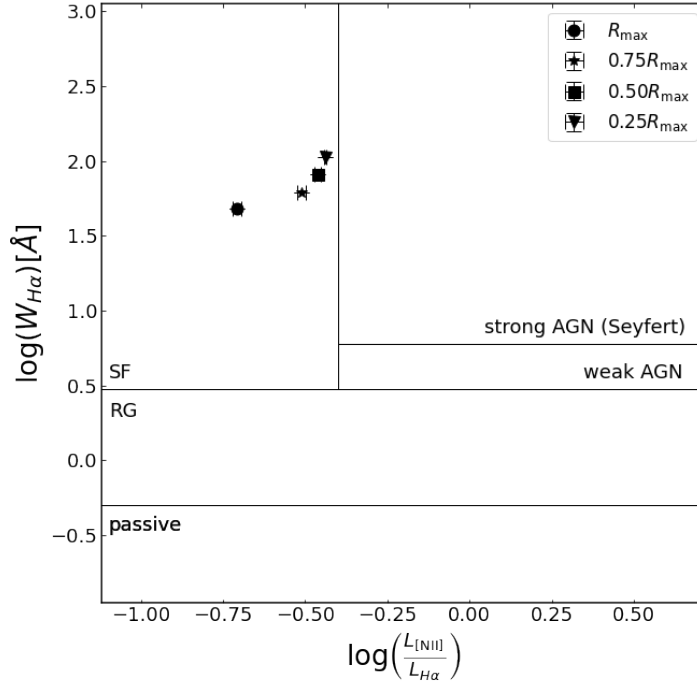
Figure 4.56: NGC4395 in the WHAN diagram. The description is similar to Figure 4.6. Each aperture is represented by a different marker (black circle: $R_{\max}$, black star: $0.75R_{\max}$, black square: $0.50R_{\max}$, and black triangle: $0.25R_{\max}$). All the analyzed apertures were located in the SF region. This must be taken with careful as the narrow emission lines were not well fitted due to the spectral resolution.
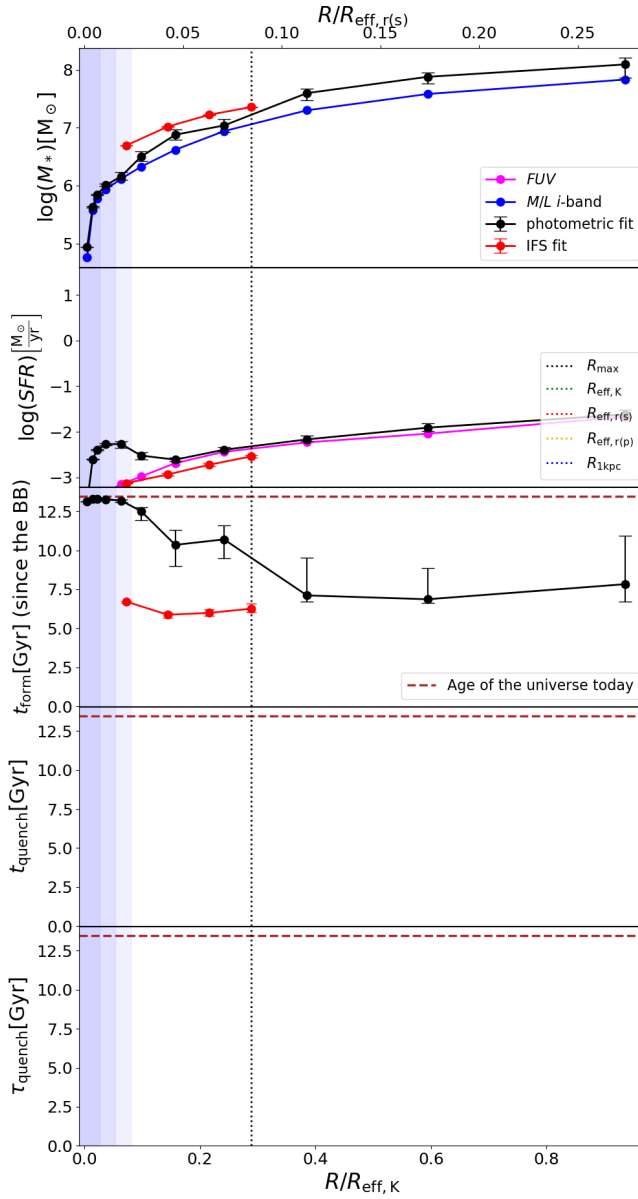
Figure 4.57: NGC4395 parameter radial profiles. The description is similar to Figure 4.9.

Name	log(M_{BH})		log(M_*)				log($sSFR$)		
	VB16	R_{1kpc}	VB16	R_{1kpc}	$0.50R_{max}$	R_{max}	R_{1kpc}	$0.50R_{max}$	R_{max}
Mrk-290	7.26 ± 0.17		10.30	9.81 ± 0.00	10.20 ± 0.00	10.31 ± 0.00	$-11.41^{+0.02}_{-0.01}$	$-11.62^{+0.02}_{-0.03}$	$-11.65^{+0.03}_{-0.04}$
ARP151	6.65 ± 0.16		10.36 ± 0.08	9.94 ± 0.00	10.11 ± 0.00	10.23 ± 0.00	<-13.00	<-13.00	<-13.00
NGC1194	7.85 ± 0.05		10.78 ± 0.08	10.19 ± 0.00	10.42 ± 0.01	10.59 ± 0.01	$-11.82^{+0.02}_{-0.01}$	$-11.90^{+0.03}_{-0.04}$	$-11.99^{+0.09}_{-0.10}$
NGC6086	9.57 ± 0.17		11.55 ± 0.07	10.35 ± 0.00	11.04 ± 0.00	11.22 ± 0.00	-12.08 ± 0.01	-12.10 ± 0.01	-12.10 ± 0.02
NGC3982	$6.95^{+0.26}_{-6.95}$		9.98 ± 0.09	9.22 ± 0.01	9.19 ± 0.01	9.27 ± 0.01	-10.83 ± 0.02	-10.31 ± 0.01	-10.77 ± 0.02
NGC2960	7.03 ± 0.05		10.86 ± 0.09	$10.06^{+0.1}_{-0.00}$	$10.22^{+0.00}_{-0.01}$	10.37 ± 0.01	-10.95 ± 0.02	$-10.48^{+0.01}_{-0.02}$	$-10.56^{+0.04}_{-0.05}$
NGC6264	7.49 ± 0.05		10.88	9.74 ± 0.00	10.66 ± 0.00	10.77 ± 0.01	-11.50 ± 0.01	-11.13 ± 0.01	-11.06 ± 0.05
NGC4395**	$4.00^{\ddagger}$		8.43	n. a.	7.02 ± 0.00	7.35 ± 0.01	n. a.	-9.95 ± 0.03	$-9.89^{+0.05}_{-0.04}$

Table 4.9: Summary of the results described in the current Section. Units for M_{BH} and M_* are given in $M_\odot$, and for $sSFR$ in yr^{-1}. VB16 stands for van den Bosch (2016). ‡ M_{BH} taken from Woo et al. (2019). **For this galaxy the R_{1kpc} aperture is out of the FoV.

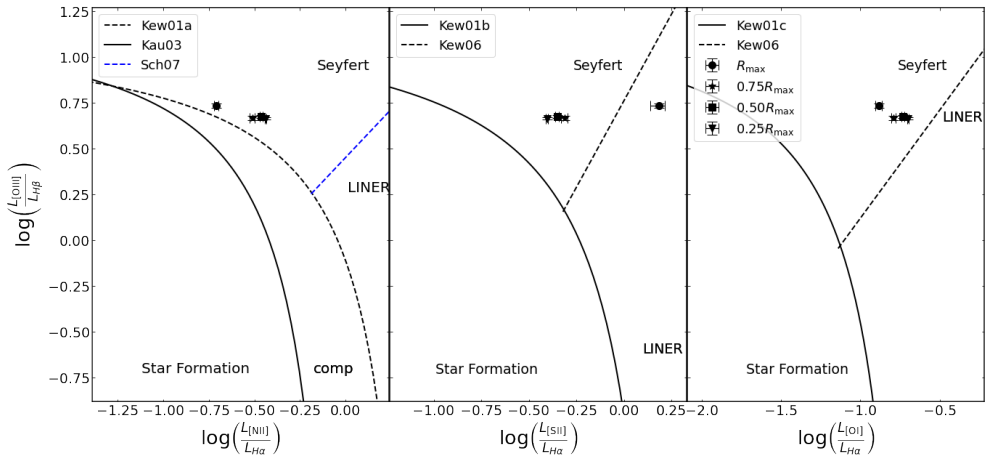| Name	t_{form}			t_{quench}			τ_{quench}		
	R_{1kpc}	$0.50R_{max}$	R_{max}	R_{1kpc}	$0.50R_{max}$	R_{max}	R_{1kpc}	$0.50R_{max}$	R_{max}
Mrk-290	$6.98^{+0.05}_{-0.04}$	$5.20^{+0.07}_{-0.07}$	$5.21^{+0.16}_{-0.16}$	$10.74^{+0.04}_{-0.05}$	8.98 ± 0.07	$8.96^{+0.16}_{-0.14}$	$3.76^{+0.08}_{-0.10}$	$3.78^{+0.11}_{-0.14}$	$3.75^{+0.27}_{-0.30}$
ARP151	$0.72^{+0.35}_{-0.26}$	$0.77^{+0.33}_{-0.31}$	$0.75^{+0.35}_{-0.30}$	$1.23^{+0.47}_{-0.42}$	$1.30^{+0.54}_{-0.42}$	$1.30+0.54-0.49$	$0.51^{+0.73}_{-0.51}$	$0.52^{+0.85}_{-0.52}$	$0.54^{+0.84}_{-0.54}$
NGC1194	$0.88^{+0.16}_{-0.08}$	$4.58^{+0.29}_{-0.25}$	$4.80^{+0.38}_{-0.40}$	$2.63^{+0.54}_{-0.25}$	$10.64^{+0.43}_{-0.40}$	$10.88^{+0.49}_{-0.57}$	$1.75^{+0.62}_{-0.41}$	$6.06^{+0.67}_{-0.68}$	$6.08^{+0.89}_{-0.94}$
NGC6086	$0.62^{+0.02}_{-0.01}$	$0.64^{+0.06}_{-0.03}$	$0.71^{+0.14}_{-0.08}$	1.88 ± 0.06	1.94 ± 0.13	$2.13^{+0.37}_{-0.25}$	$1.25^{+0.07}_{-0.09}$	$1.30^{+0.15}_{-0.18}$	$1.42^{+0.45}_{-0.39}$
NGC3982	$9.41^{+0.21}_{-0.19}$	$8.59^{+0.12}_{-0.13}$	$9.83^{+0.18}_{-0.22}$	-*	-*	-*	-*	-*	-*
NGC2960	10.34 ± 0.08	11.43 ± 0.06	11.48 ± 0.12	13.16 ± 0.01	-*	-*	$2.82^{+0.09}_{-0.08}$	-*	-*
NGC6264	$0.98^{+0.04}_{-0.02}$	$1.45^{+0.15}_{-0.08}$	$5.48^{+0.18}_{-0.25}$	$3.01^{+0.17}_{-0.06}$	$5.38^{+0.55}_{-0.36}$	$12.40^{+0.17}_{-0.22}$	$2.02^{+0.20}_{-0.10}$	$3.93^{+0.63}_{-0.51}$	$6.92^{+0.42}_{-0.40}$
NGC4395**	n. a.	$5.88^{+0.14}_{-0.20}$	$6.29^{+0.37}_{-0.22}$	n. a.	-*	-*	n. a.	-*	-*

Table 4.10: Continuation of the summary of the results described in the current Section. Units for t_{form}, t_{quench} and τ_{form} are given in Gyr. Column $M_{BH} - \sigma_*$. Dist refers to the distance to the $M_{BH} - \sigma_*$ relation (van den Bosch, 2016), as shown in Figure 2.2. *No quenching time for this aperture because it is classified as star forming. **For this galaxy the R_{1kpc} aperture is out of the FoV.

| Name | $\log(Z_*)$ | | | A_V | | | AGN | | $M_{\mathrm{BH}} - \sigma_*$ |
	R_{1kpc}	$0.50 R_{\mathrm{max}}$	R_{max}	R_{1kpc}	$0.50 R_{\mathrm{max}}$	R_{max}	VC06	IFS	Dist
Mrk290	$-1.69^{+0.02}_{-0.01}$	-1.26 ± 0.02	-1.02 ± 0.02	$< 10^{-3}$	$< 10^{-3}$	$< 10^{-3}$	S1.5	S	-0.02
ARP151	-0.65 ± 0.01	-0.59 ± 0.01	-0.56 ± 0.01	0.61 ± 0.01	0.55 ± 0.01	0.50 ± 0.01	S1[†]	S	-0.08
NGC1194	-0.45 ± 0.00	-0.41 ± 0.01	$-0.42^{+0.02}_{-0.01}$	1.34 ± 0.00	1.14 ± 0.01	0.97 ± 0.02	S1.9	S	0.04
NGC6086	-0.08 ± 0.00	-0.16 ± 0.01	-0.21 ± 0.01	0.37 ± 0.00	0.35 ± 0.01	0.34 ± 0.01	-	-	0.03
NGC3982	-0.85 ± 0.01	$0.35^{+0.00}_{-0.01}$	-0.92 ± 0.01	0.64 ± 0.01	0.73 ± 0.01	$0.59^{+0.01}_{-0.02}$	S1.9	*comp.*	0.02
NGC2960	$0.13^{+0.01}_{-0.02}$	0.33 ± 0.01	$0.32^{+0.01}_{-0.02}$	0.93 ± 0.00	1.00 ± 0.01	0.97 ± 0.02	Liner	Liner, S	-0.12
NGC6264	-0.31 ± 0.01	$-0.11^{+0.01}_{-0.02}$	-0.09 ± 0.03	0.65 ± 0.01	0.58 ± 0.01	0.58 ± 0.03	S2	S	-0.05
NGC4395**	n. a.	0.30 ± 0.01	-0.06 ± 0.01	n. a.	0.28 ± 0.03	$0.43^{+0.04}_{-0.03}$	S1.8	S	0.02

Table 4.11: Continuation of the summary of the results described in the current Section. Units for Z_* are given in $Z_\odot$, and for A_V in magnitudes. VC06 stands for Véron-Cetty & Véron (2006) and column IFS within the AGN group mean to state only if the objects are classified as hosting an AGN with our analysis (S stands for Seyfert). [†]Classification given by Khachikian & Weedman (1974). **For this galaxy the R_{1kpc} aperture is out of the FoV.

Chapter 5

Discussion

In this work we conducted a pilot study to understand the galaxy-SMBH co-evolution for which we carried out an analysis for galaxies with BH masses obtained via *direct methods* and for which Integral Field Spectroscopy, IFS, observations are available. To do so, we used the van den Bosch (2016) sample of ~ 250 galaxies for which the mass of their central BHs were robustly constrained by using dynamical tracers (such as gas, stars, masers) or the reverberation mapping technique. The van den Bosch (2016) BH sample was then cross-matched with the MaNGA one (Bundy *et al.*, 2015; Wake *et al.*, 2017) from the SDSS DR17 (Abdurro'uf *et al.*, 2022) which represents the state of the art of IFS observations. In total, the cross-matched sample resulted in 8 galaxies for which, hereafter, we will refer to it as the sample. From this sample of galaxies, we performed an exhaustive analysis to the MaNGA IFS observations in order to derive the stellar population properties of each galaxies in 8 different apertures (whenever it was possible); these are $R_{\max}$, $R_{\mathrm{eff},K}$, $R_{\mathrm{eff,r(s)}}$, $R_{\mathrm{eff,r(p)}}$, R_{1kpc}, $0.75R_{\max}$, $0.50R_{\max}$ and $0.25R_{\max}$, see Chapter 4 for a description of the definitions. The analysis of the MaNGA IFS data was performed by using one of the state of the art codes for modelling the spectra and photometry of the galaxies, BAGPIPES (Carnall *et al.*, 2018).

Our sample consist of seven galaxies that are AGNs and are known to be feeding their SMBHs in the radiative mode (also called quasar mode). Particularly, Mrk290 and ARP151 show narrow and broad emission lines that are consistent with being radiation emitted by an active BH. We also found a continuum emission that presumably comes from the AGN accretion disk. These two galaxies are consistent with being Type 1 AGNs (Véron-Cetty & Véron, 2006), and we confirm that are in the Seyfert region according to our classification from the BPT diagram.

The AGN model of NGC1194, NGC3982, NGC2960, NGC6264 and NGC4395 is well described by narrow lines from the NLR. Indeed we found that these 5 galaxies are classified as Type 2 AGN according to the Véron-Cetty & Véron (2006) catalog. Finally, NGC6086 is a BCG galaxy, it is a quiescent galaxy with not clear signatures of AGN activity in the optical region where MaNGA IFS data covers and with no signatures to be feeding its SMBH in the radiative mode.

Next in this Chapter, we discuss the implications of our results on the light of the galaxy-SMBH co-evolution. It is widely believed that AGNs play a fundamental role in this co-evolution. As discussed in the Introduction, there are two leading modes 1) the radiative mode and 2) the radio mode. While the radiative mode is thought to play a role in removing material from the galaxy (observed by outflows of molecular, atomic and ionised gas Sturm *et al.*, 2011; Cicone *et al.*, 2014; Fiore *et al.*, 2017); the radio mode is more often thought to act as a preventive mechanism (by heating the gas and preventing cooling and star formation, Croton *et al.*, 2006; Somerville *et al.*, 2018). Seven of the eight galaxies that we are studying here host AGNs[1] (*i.e.* are in the radiative mode) and we will spent more time discussing this mode in the light of our results.

Several previous studies have identified observational signatures of AGN-driven outflows (see e.g., Faucher-Giguère & Quataert, 2012; Hopkins *et al.*, 2016; López-Cobá *et al.*, 2020). In particular these studies have found that ejective feedback increases the sizes and flatten the central region of galaxies (Dubois *et al.*, 2016; Choi *et al.*, 2018). These findings suggest a plausible correlation between the size-mass and density-mass (or velocity dispersion-mass see e.g., Chen *et al.*, 2020) relations and the strength of AGN feedback, likely through the AGN luminosity. However, when we analyzed our sample (which is admittedly small), we did not observe any clear trends as shown in Figure 2.2. Specifically, our sample includes two powerful AGNs, Mrk290 and ARP151, which are compact galaxies undergoing a compaction event. In light of the above tension, we considered a proposal for quenching galaxies that could potentially explain our observations. This model states that dissipative contraction (*i.e.*, gas compaction), due to drastic angular momentum loss, leads to a compact star forming galaxy (often refer as blue nugget in the literature) that it will be more concentrated in its centre (for a recent review discussion see Lapiner *et al.*, 2023). A central bulge quenched region is expected from this model.

While our sample is small enough to draw any general conclusion, next we discuss in a galaxy-by-galaxy basis the implications of the results obtained from the IFS data analyzed with Bagpipes and draw individual possible scenarios

---

[1]It is not clear that the BGC NGC6086 is in the radio (or jet) mode as their are often found in central galaxies of groups and clusters. *X-ray* and *sub-mm* observations are required to clarify the above.

for the galaxy-SMBH co-evolution.[2]

- **Mrk290**: Mrk290 is a well know bright AGN, here we speculate that the origin for the high luminosity AGN and the negative gradients of $sSFR$ and stellar population ages could be related to the accretion of gas with low angular momentum. This gas fuels a centrally concentrated star formation burst and also could help to feed the SMBH in the central region. This phenomenon known as the compaction event (see e.g., Zolotov *et al.*, 2015; Tacchella *et al.*, 2016b,a), is typically characterised by relative low metallicity, young ages and high SFR and it could be triggered by disk instabilities and/or gas flowing directly from the intra-halo system or even mergers. In the case of Mrk290 its small size and the lack of evidence of recent mergers, points out that the compaction event most likely was the result of a violent disk instability in the past that occurred at $z < 1.0$ (according to the quenching times of the central part, see Figure 4.2). The results obtained suggest a very low Z_* and practically no dust attenuation; for a galaxy like this one, with $\log(M_*/M_\odot) = 10.30$, it could be worth considering the potential effects of the Z_*-age degeneracy[3], but in the corner figures of the 2D-posterior probability distributions (see Appendix A), it can be noticed that the analysis made through BAGPIPES breaks this degeneracy.

- **ARP151**: This galaxy appears to be an excellent candidate as a descendant of galaxies that quenched very early in the universe ($z > 3$). ARP151 formed over a period of $\sim$300 Myr around $z \sim 6$ from an intense burst of SF of primordial gas. Recently, Carnall *et al.* (2023a) identified a population of massive quiescent galaxies between $3 < z < 5$. Notably, the SFH of ARP151 resembles that of GS-9209 Carnall *et al.* (2023b), a galaxy that formed over a period of approximately 200 million years, centered at $z \sim 7$, and has a stellar mass of $\log(M_*/M_\odot) \sim 10.3$. GS-9209 has a supermassive black hole of $\sim 10^{8.7}$ $M_\odot$, which may have played a role in quenching the galaxy Carnall *et al.* (2023b). In our case, ARP151 has a black hole that is a factor of approximately 100 smaller than GS-9209's. Therefore, the BH activity in ARP151 is likely not the reason why the

---

[2]In this discussion we do not use the SED broad-band fitting results as they are less accurate than the IFS results and also because in some cases resulted in contradiction to our IFS analysis.

[3]The Z_*-age degeneracy is a significant challenge in the study of galactic evolution and stellar populations, it refers to the difficulty in distinguishing the age and metallicity of stars based on its observed characteristics; stars with higher metallicity tend to form later in the history of the galaxy, as they are enriched with heavier elements from previous generations of stars, on the other hand, lower metallicity stars are typically older. The degeneracy arises because changes in age and metallicity can produce similar effects on the spectra (see more at Worthey, 1993; Gallazzi *et al.*, 2005).

galaxy was quenched initially, but it has acted as the maintenance mechanism to keep ARP151 quenched.

- **NGC1194**: This galaxy enters into the canonical picture where galaxies formed from the inside-out, with older stars at the centre and younger stars in the outskirts, but it also quenched from the inside-out, possibly due to the activity of the AGN. When examining the SFH, the central region reached its peak star formation rate at $z \sim 5$ and had become quiescent by $z \sim 2.5$. This trend matches the epoch of peak QSO/AGN activity, which occurred around $z \sim 2$ (Merloni & Heinz, 2008). We speculate that the AGN could have helped to quench the galaxy and may also be responsible for maintaining the hot gas in the intra-halo system, which could be used as fuel for future star formation.

- **NGC6086**: This is a BCG that formed from the inside-out, with the older central regions forming first and the younger outer regions forming later. However, despite its initial star formation $\sim 300 \, M_\odot/yr$, NGC6086 galaxy became quiescent approximately 2 Gyr after the Big Bang. Similarly to ARP151, this makes it an interesting candidate as a descendant of quiescent galaxies that existed at $z > 3$ (Carnall *et al.*, 2023a). Regarding the role of the SMBH in NGC6086, it is not entirely clear how it helped to quench the SF of this galaxy. It is unlikely that the SMBH was the sole reason for the galaxy to quench, as this occurred too early in cosmic history ($\sim$2 Gyr after the BB) and before the appearance of the most powerful quasars and AGNs. However, the AGN feedback could have played an important role for decreasing and maintaining the the galaxy quenched.

- **NGC3982**: This is an interesting galaxy that exhibits several peculiarities. One such peculiarity is its massive SMBH, which is unusually large for a galaxy of its size and velocity dispersion and it is remarkably compact, as can be seen in Figure 2.2. However, despite these peculiarities, NGC3982 has remained a star-forming galaxy in its central region for an extended period of time, as shown in Figure 4.31. The combination of a compact, young, and star-forming central region with a low metallicity is similar to Mrk290 galaxy in which a compaction event, likely triggered by disk instabilities, has been proposed above as the mechanism for feeding the AGN in the central region and maintaining a young, low-metallicity population. Interestingly, the HST image of NGC3982 has revealed the presence of a nuclear mini-spiral between the circumnuclear star-forming region and the AGN. This structure has been theorized to serve as a pathway for gas to be transported to the SMBH from the circumnuclear star-forming region Zhang *et al.* (2008). It is possible that this mini-

spiral formed relatively recently and thus the AGN activity has not yet had sufficient time to affect the SFR in the galaxy.

- **NGC2969**: This galaxy shares similarities with NGC3982 in terms of its SFH and SMFH. It has a typical half-light radius and BH mass for its mass, but the SFR of its central region appears to be slightly suppressed, as evident in Figure 4.39, and it has a higher metallicity towards the outskirts. This galaxy assembled from the inside-out, with the inner aperture already quenched. While it is uncertain whether the SMBH has affected the SFR of the galaxy, AGN feedback from the SMBH could provide an explanation for its features. It is worth noting that the more metallic outskirts of the galaxy could be due to the baryon cycle of expulsion and reaccretion of material resulting from some feedback process. Given its significant mass, estimated at $M_* \sim 7.2 \times 10^{10}$ M$_\odot$, it is likely that NGC2960 resides in a dark matter halo of sufficient mass, around $M_{\mathrm{vir}} \sim 8 \times 10^{12}$ M$_\odot$ (Rodríguez-Puebla *et al.*, 2017), for stellar feedback[4] playing a role in enriching its outskirts but due to the AGN feedback. Another possible interpretation is that fresh gas with low angular momentum is feeding the central parts of the galaxy, including the AGN, similar to Mrk290. Further research is necessary to fully understand the mechanisms behind these characteristics.

- **NGC6264**: This galaxy is a prototype galaxy with a typical size and BH mass for its M_*. It assembled from the inside-out and also quenched in the same manner, as discussed previously. Figure 4.46 shows the stellar population properties of NGC6264 as a function of its galactocentric distance. It's notable that there is a sudden change below $\sim R_{\mathrm{eff},K}$ in all its stellar parameters; the star formation rate drops, the galaxy is older, and it quenched $\sim 2.5 - 4.5$ Gyr after its central part formed. Although NGC6264 has an active BH, it is not clear whether it's responsible for the central shut-off of the galaxy because its properties and BH mass are not different from those of a late-type galaxy. Furthermore, there are no indications that NGC6264 is building a core, as its value of $\Sigma_1 = M_*(R = 1\mathrm{kpc})/\pi \sim 2 \times 10^9 / M_\odot \cdot \mathrm{kpc}^{-2}$ NGC6264 is almost 0.5 dex below the relation of quiescent galaxies for its mass (see e.g., Fang *et al.*, 2013; Luo *et al.*, 2020). Woo & Ellison (2019) suggest that there is a group of galaxies that quenched in a secular manner by growing from the inside-out, characterized by their relatively low central mass density, Σ_1 and suppressed SFR, and we speculate that NGC6264 may fit into this

---

[4]Halos with masses below $M_{\mathrm{vir}} \sim 7 - 10 \times 10^{11} M_\odot$ are those whose stellar feedback might play a more relevant role (see e.g., Somerville & Davé, 2015; Rodríguez-Puebla *et al.*, 2017; Wechsler & Tinker, 2018)

category. However, further research is necessary to better understand this phenomenon. Finally, an interesting aspect of NGC6264 is its high metallicity in the outskirts. There is no evidence of mergers for this galaxy, and the stellar feedback may not be responsible for enriching the central ISM because this galaxy is quiescent for almost all radii. An intriguing possibility, similar to NGC2960, is that AGN feedback could be accountable for this phenomenon.

- **NGC4395**: This is the less massive galaxy of the final sample, even more, the SED studied on the IFS analysis corresponds only to a central star cluster in the galaxy, and that is maybe the main reason why the fitted M_* at $R_{\max}$ reaches only a 10% of the stellar mass inferred by its luminosity in the K-band, $M_*(L_K)$. The central BH of this galaxy is also the least massive of the sample, having a mass of approximately 10^4 $M_\odot$, which is in the border between the intermediate and the supermassive ones. This galaxy is highly star-forming with an $sSFR > 0.1$ Gyr^{-1} and no quenching time reported at all its apertures, having no signatures of a central shut-off caused by the SMBH. It has also a relatively young stellar population, with t_{form} around 6 Gyr after the BB, and a high stellar metallicity which converges near to the maximum prior value, 2.5 $Z_\odot$, at the innermost aperture. Further research and a SED fitting to data with a better spectral resolution is necessary to fully understand and characterise this dwarf galaxy and its AGN.

Finally, as a guideline for the reliability of our results, in Appendix B we present a comparison of the physical parameters, M_*, SFR, stellar age, Z_* and A_V, inferred through our IFS analysis vs. the ones reported by the last version of Pipe3D (pyPipe3D, Sánchez *et al.*, 2022). We noticed that pyPipe3D tends to estimate slightly larger M_* and Z_* than our IFS analysis with Bagpipes, this is most evident for Mrk290 and ARP151, both AGNs Type 1, as expected, since pyPipe3D is not considering in their models the radiation coming from the AGN and in consequence is overestimating the M_* and the Z_*. In the case of the SFR, it seems to be no evident bias for the entire sample, but looking again to the Type 1 AGNs mentioned above, Mrk290 and ARP151, the contribution of the continuum from the accretion disk of the AGN, not considered by pyPipe3D (but modeled with a power law in our IFS analysis), is making their SFRs get overestimated, because of the excess of radiation in the bluest part of the spectrum. Finally the A_V from the dust inferred by our IFS analysis is slightly greater than the one reported by pyPipe3D, and the age of the stellar populations seems to have no bias.

Chapter 6

Conclusions

In this study, we aimed to explore the co-evolution of galaxies with their central supermassive black holes (SMBH) by conducting a *pilot* analysis. We used a sample of galaxies from the van den Bosch (2016) catalog based on a large compilation from the literature of robust BH masses determinations from various methods, such as; dynamical tracers and reverberation mapping. We then cross-matched this BH sample with the Mapping Nearby Galaxies at Apache Point Observatory (MaNGA) (Bundy *et al.*, 2015; Wake *et al.*, 2017) Integral Field Spectroscopy (IFS) observations from SDSS DR17 (Abdurro'uf *et al.*, 2022), which is a state of the art survey for IFS observations. After the cross-match, we obtained a sample of 8 galaxies for which we performed an extensive analysis of the MaNGA IFS data.

To analyze the stellar population properties of each galaxy, we derived their properties in five different apertures, which were R_{max}, $R_{\mathrm{eff},K}$, $R_{\mathrm{eff,r(s)}}$, $R_{\mathrm{eff,r(p)}}$, and R_{1kpc}. The analysis was conducted using a modified version of BAGPIPES (Carnall *et al.*, 2018, 2019b), which is one of the most advanced codes for modeling the spectra and photometry of galaxies. We modified BAGPIPES to include a model for an AGN given by:

- Emission from the Narrow Line Region (NLR): We assume that each emission line, Hα, Hβ, Hγ, Hδ, [O\textsc{iii}]4363,4959,5007, [N\textsc{ii}]6548,6583, [S\textsc{ii}]4072,6717,6731 and [O\textsc{i}]6300,6365, are well described by single Gaussians.

- Emission from the Broad Line Region (BLR): We assume that the Balmer lines, Hα, Hβ, Hγ and Hδ, are sometimes described by a second *broad* component and sometimes even a third *very broad* component. We described each of these broad emission lines with Gaussian profiles.

- AGN continuum: When it was necessary to consider a continuum in the blue region of some AGNs we consider a power-law model over the en-

tire analysed wavelength range, with $\lambda_0 = 3800$ Å, resulting in two free parameters: A_{AGN} and α_{ANG}.

It is worth mentioning that our version of BAGPIPES fits all the different components of the galaxies at once, i.e., it fits the stellar continuum, nebular lines and our AGN model, all at the same time.

In addition to the SED fitting of the IFS data we performed a broad band fitting at different apertures by using the azimuthally-averaged radial surface brightness profile reported as the average surface brightness in a series of annuli for the seven-bands *FUV, NUV, u, g, r, i* and *z*, where *FUV* and *NUV* were taken from GALEX (Martin *et al.*, 2005) and *ugriz* from the SDSS photometric data from NSA catalog (Blanton *et al.*, 2017).

Our main results and conclusions are:

- Three galaxies, NGC4395, NGC2960 and NGC3982, are star forming galaxies, while six, NGC6264, NGC6086, NGC1194, ARP151 and Mrk290, are quiescent.

- Out of the 8 galaxies in our sample, seven are classified as active galactic nuclei (AGNs).

- Two of the galaxies, Mrk290 and ARP151, showed both narrow and broad emission lines that are consistent with radiation emitted by an active BH. We also detected continuum emission that is likely from the AGN accretion disk.

- These two galaxies are classified as Type 1 AGNs according to the Véron-Cetty & Véron (2006) catalog, and they fall within the Seyfert region based on our classification from the BPT diagram. The broad emission is consistent with the Véron-Cetty & Véron (2006) classification of Type 1.

- Using the BLR components both for Hα and Hβ lines and the single epoch spectroscopy method to infer M_{BH} (Greene & Ho, 2005) we estimated BH mases of 2×10^7 M$_\odot$ for Mrk290 and 2.5×10^6 M$_\odot$ for ARP151. In both cases the differences between direct methods where less than a factor of ~ 2.

- The AGN model of NGC1194, NGC3982, NGC2960, NGC6264, and NGC4395 is well-described by narrow lines from the narrow-line region (NLR), and they are classified as Type 2 AGNs based on the Véron-Cetty & Véron (2006) catalog, consistent with the narrow emission from their spectra.

- NGC6086 is a quiescent galaxy with no clear signatures of AGN activity in the optical region covered by the MaNGA IFS data. It is a BCG in the Abell 2162 cluster (McConnell *et al.*, 2011).

- The galaxies NGC1194, NGC6086 and NGC6264 enter into the canonical picture of galaxy formation: they formed from the inside-out. Galaxies NGC1194 and NGC6264 have also signatures of being quenched from the inside-out. While the galaxy NGC1194 was probably quenched due to the AGN activity, the same scenario is less clear for NGC6264 which is more consistent with being quenched by secular processes.

- The galaxies Mrk290, ARP151, NGC3982 and potentially NGC2960, are consistent with the features of experiencing a compaction event in which the accretion of gas with low angular momentum fuels a centrally concentrated star formation burst and also could help to feed the SMBH in the central region. The compaction event could be triggered by disk instabilities and/or gas flowing directly from the intra-halo system or even mergers.

- Our results suggest that the galaxy NGC2960 enriched its outskirts due the re-accretion of gas from the AGN feedback.

- Our results suggest that ARP151 and NGC6086 formed from a very intense burst of SF and then by $z \sim 6$ and $z \sim 3$, respectively, evolved as quiescent galaxies. These galaxies are excellent candidates to be the descendant of galaxies that quenched very early in the universe ($z > 3$) (Carnall $et\ al.$, 2023a,b).

- Our broad-band SED analysis helped to confirm that our stellar mass estimations were correct but they were not conclusive regarding the SFRs and time-scales.

While our results do not show a conclusive evidence of how SMBH, in particular the active ones (AGNs), shut-down the star formation or simply co-evolved with their host galaxies, our *pilot* study points out that probably this co-evolution is more complex of just a simple picture of a turn on (AGN) and shut down (SF) relationship. Next, we describe our future plans in order to improve our modelling and increase our statistics.

6.1 Outlook for Future Work

Several modifications from the approaches described in this work can improve our modeling and increase our statistics, below we describe few of them.

- In this work we used a power law to model the AGN spectra continuum only. It is desirable to include a more physically motivated model to increase the reality of the model and decrease the degrees of freedom in

the model. For example, the accretion disk of the AGN can be modelled like a black body.

- Perform a Bagpipes analysis by combining our MaNGA IFS data and our NSA azimuthally-averaged radial surface brightness profiles to include more *UV* bands.

- In order to improve the quality of the SED fitting analysis and the information around the SF processes, it would be useful to search for more *IR* observations, even if they are not spatially resolved, also *sub-mm* and *X-ray* bands would be useful to be included in our analysis.

- Cross match the van den Bosch (2016) sample with other IFS surveys, such as CALIFA, SAMI and AMUSING++ data, to enlarge our sample.

Appendix A

Spectral SED Fitting and Corner Diagrams

In Chapter 4 we present the results obtained from the SED fitting for each galaxy in the sample. Particularly we show the SED fitting model to the IFS data for R_{max} aperture. In this Appendix we present the SED fitting model to the IFS data and the corner diagrams, for each galaxy in the sample, at every studied aperture, including the FoV.

The figures can be found at `https://drive.google.com/drive/folders/12wVb6JmQETDtk8Nh-dDEom2OAb8vpD1G?usp=sharing`. They are organized by a directory per galaxy, and a subdirectory per analysed aperture. The description of the SED figures is similar to Figure 4.1, while the corner diagrams show the posterior probability distribution obtained for every free parameter included in the prior parameter space (these figures are relevant because they exhibit valuable information of the fitted model, such as correlations between free parameters).

Finally, BPT and WHAN diagrams, as well as the evolution figures and the radial profiles are also included in the digital repository mentioned above, together with the summary figures showed in the Section 2.2 (see Figure 2.3), for each galaxy.

Appendix B

Parameter Comparison vs. Pipe3D

In this Appendix we present the comparison between the physical parameters inferred through the IFS and the ones reported in the last version of Pipe3D (pyPipe3D, Sánchez *et al.*, 2022). Remember that our IFS analysis allow us to report results at different apertures, but for this comparison we consider the ones obtained for the $R_{\mathrm{eff,r(p)}}$ aperture (when possible, but for NGC3982 and NGC4395, where $R_{\mathrm{eff,r(p)}}$ is out of the FoV, we consider the results inferred at the FoV).

It is important to take into account that BAGPIPES considers the IMF described by Kroupa & Boily (2002), whilst pyPipe3D considers the one described by Salpeter (1955). It is important to consider the offsets that arise from the differences of the IMF when making the comparison of the parameters, particularly in the age, the M_* and the SFR; for this we use the values reported in Tables B1 and B3 of Pforr *et al.* (2012), for late and early type galaxies, respectively.

Figure B.1: Stellar mass comparison. In the vertical axis are the results obtained through our IFS analysis by BAGPIPES, in the horizontal axis are the results reported by pyPipe3D. Both are in logarithmic scale, in units of $M_\odot$. The galaxies are distinguished by early-type (red marker) and late-type (blue marker). It can be noticed that the results from pyPipe3D are slightly overestimated, compared with the ones from BAGPIPES.

Figure B.2: Star formation rate comparison. In the vertical axis are the results obtained through our IFS analysis by Bagpipes, in the horizontal axis are the results reported by pyPipe3D. Both are in logarithmic scale, in units of $M_\odot/yr$. The galaxies are distinguished by early-type (red marker) and late-type (blue marker) Both are in units of $\log(M_\odot)$. There is no evident bias for the entire sample, but for Mrk290 and NGC3982 the results from pyPipe3D are overestimated, and ARP151 does not appear because its SFR inferred by our IFS analysis is $<< 10^{-3}$ $M_\odot/yr$.
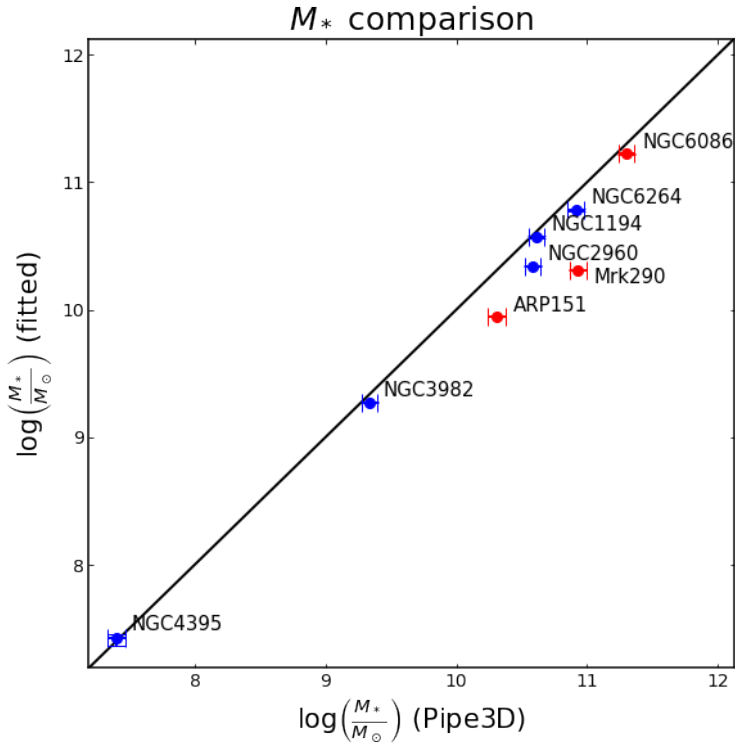
Figure B.3: Stellar age comparison. In the vertical axis are the results obtained through our IFS analysis by Bagpipes, in the horizontal axis are the results reported by pyPipe3D. Both are in units of Gyr. There is no evident bias.

Figure B.4: Stellar metallicity (mass weighted) comparison. In the vertical axis are the results obtained through our IFS analysis by BAGPIPES, in the horizontal axis are the results reported by pyPipe3D. Both are in logarithmic scale, in units of $Z_\odot$. The galaxies are distinguished by early-type (red marker) and late-type (blue marker). It can be noticed that the results from pyPipe3D are overestimated, compared with the ones from BAGPIPES.
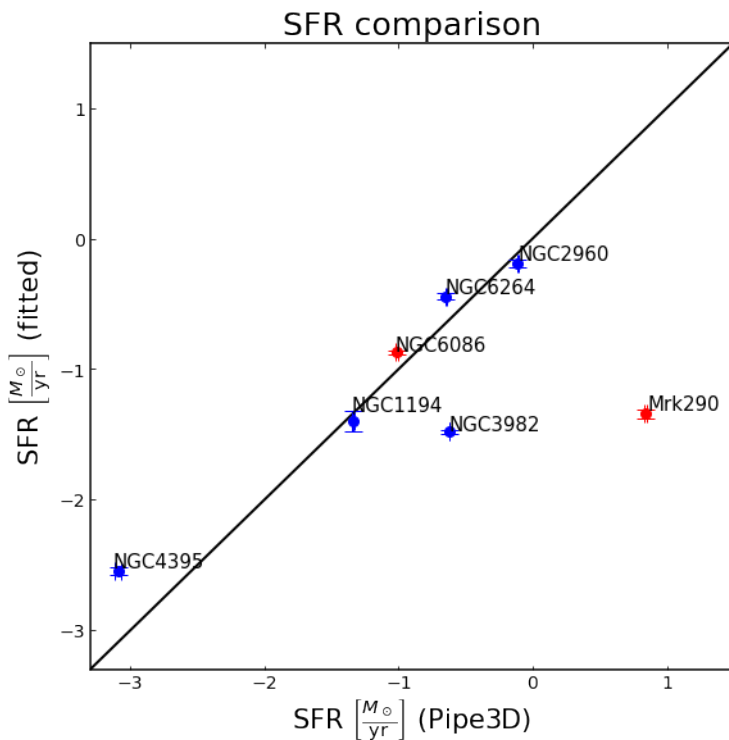
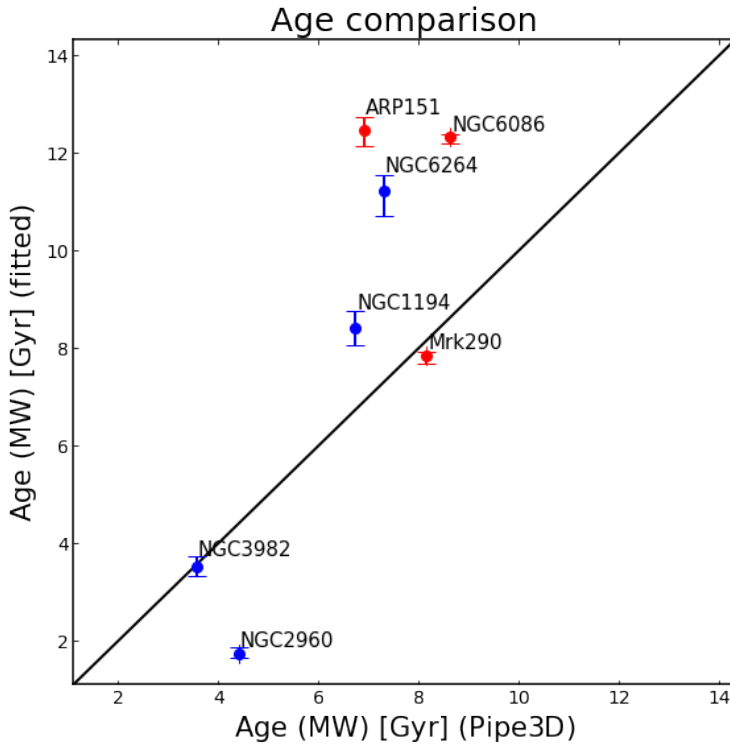Figure B.5: Dust attenuation comparison. In the vertical axis are the results obtained through our IFS analysis by BAGPIPES, in the horizontal axis are the SSP results reported by pyPipe3D. Both are in units of magnitudes. The galaxies 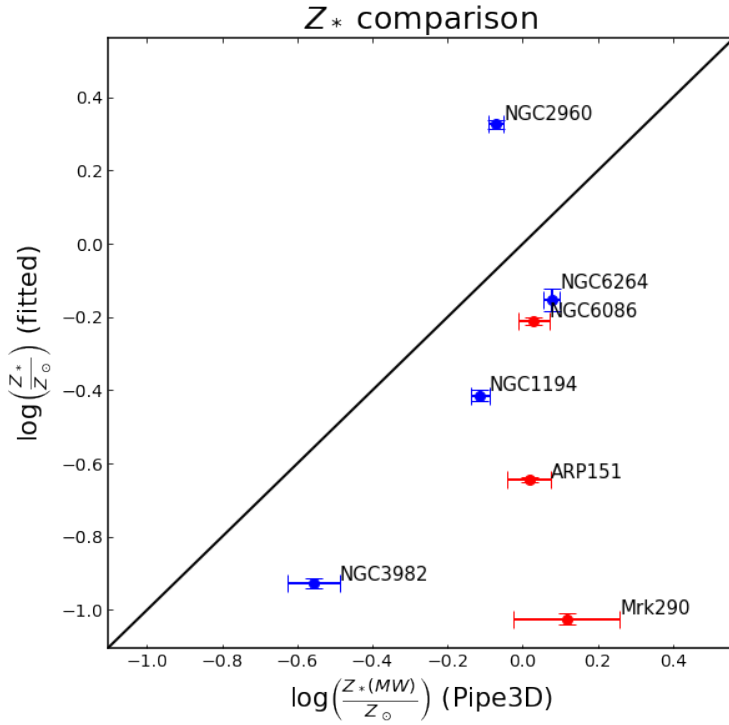are distinguished by early-type (red marker) and late-type (blue marker). It can be noticed that the results from pyPipe3D are slightly underestimated, compared with the ones from BAG-PIPES.
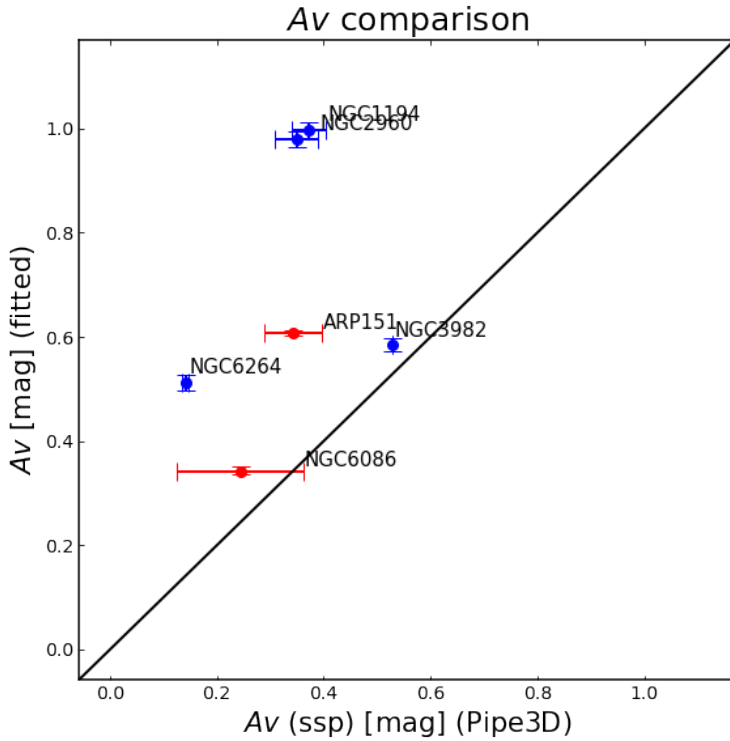
Appendix C

Evolution Histories From the Photometric Analysis

For each galaxy we present the star formation and mass assembly histories for all the analysed apertures above the PSF radius (of 2.52 arcsec) of the broadband analysis introduced in Subsection 3.2.5.

C.1   Mrk290

As discussed in Section 2.2, Mrk290 is a galaxy whose light is emitted from the AGN that dominates the bluest emission of the SED. It was not possible to fit simultaneously the stellar population and the AGN contribution because its emission is very complex.

Figure C.1 shows the SFHs inferred from the six analyzed apertures above the PSF radius. These results are considerably different from the ones obtained through the spectroscopic analysis, showing a flat SFH for the outer apertures and very young stellar populations on inner apertures. The evolution of $sSFR$ at all the apertures stays above the value of $2.5H(z)$ at all z, which indicates that the galaxy has been star forming since early epochs ($z \sim 10$) at all the analysed apertures; this means that the galaxy has not quenched yet and consequently t_{quench} is not defined for any aperture.

It is clear that for smaller apertures the formation time of the fitted stellar population corresponds to most current epochs, corresponding all to $z(t_{\mathrm{form}}) <$ 0.9, when for the smallest aperture ($R = 1.5\ R_{\mathrm{eff},K}$) $z(t_{\mathrm{form}})$ is even lower than 0.1. This means that the fitted stellar population is very young, even more at the centre of the galaxy. Finally, at the present time the circular aperture corresponding to $R = 6.33\ R_{\mathrm{eff},K}$ is the one with the closest inferred stellar mass to $M_*(L_K)$.
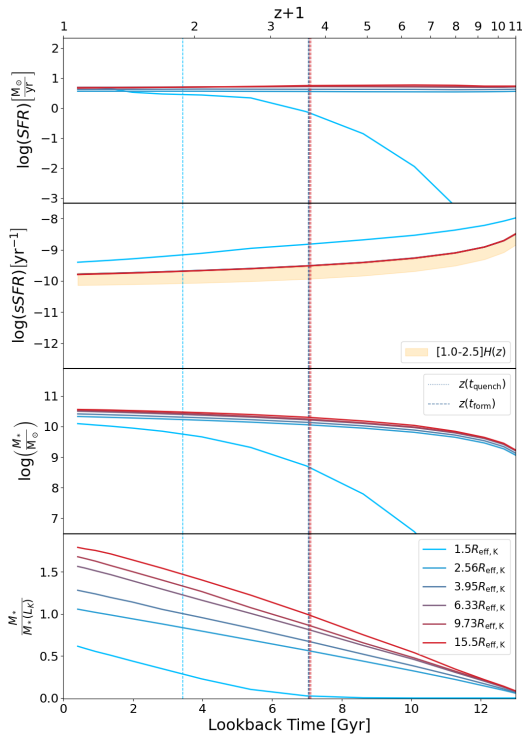
Figure C.1: Mrk290 evolution from photometry at different apertures.

C.2 ARP151

As in the case of Mrk290, the AGN continuum of ARP151 was not fitted simultaneously along with the stellar population because of its complex contribution to the SED. In Figure C.2 can be seen that the SFH is flat all along the galaxy with a SFR of approximately 1 $M_\odot$ per year. This galaxy has been star forming since early epochs, however only the inner aperture ($R = 0.27\ R_{\mathrm{eff},K}$) shows a slight decline in the SFR, leading to the present $sSFR$ being close to below $H(z)$.

In this galaxy the two largest apertures analyzed ($R = 1.75\ R_{\mathrm{eff},K}$ and $R = 2.80\ R_{\mathrm{eff},K}$) are both the ones with the actual M_* closest to $M_*(L_K)$, being around $(0.85 - 1.15)M_*(L_K)$. Also, the formation time corresponds to slightly earlier epochs for smaller apertures, with $z(t_{\mathrm{form}})$ around $(1.9 - 2.1)$, and there is not t_{quench} defined for any aperture. The above suggests that the distribution of the stellar population is more or less uniform.
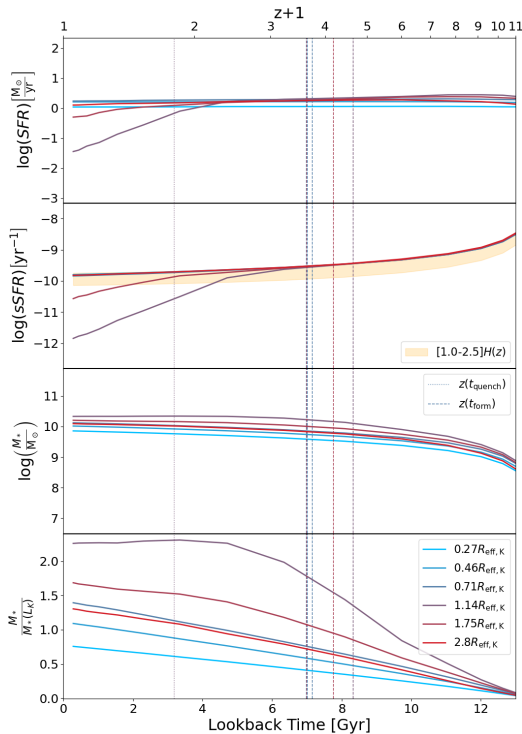
Figure C.2: ARP151 evolution from photometry at different apertures.

C.3 NGC1194

NGC1194 is a S0 galaxy with a central AGN catalogued as a Seyfert. Unlike Mrk290 and ARP151, the AGN emission of NGC1194 is dominated by narrow lines with and of low-luminosity. We notice also that for the rest of the galaxies the luminosity of their central AGNs are not too relevant to be accounted in our SED photometry fitting.

The evolution of the stellar population of NGC1194 is shown in Figure C.3. We notice that the SFH and SMFH are consistent with those that we inferred from our spectroscopic analysis, at all the apertures. Our best SED fitting results show that NGC1194 has been forming stars more actively in the centre, $R < 0.6 \ R_{\text{eff},K}$, than in outer radii since $z < 1$. Indeed, the outer radii, $R > 0.6 \ R_{\text{eff},K}$, has been quenched since $z \sim 1$. Nonetheless, the galaxy is consider quiescent as whole.

The central part of NGC1194 formed at $z \sim 2$ while the outer part at $z \sim 1$, that is, NGC1194 formed from the inside-out. This is also consistent with our spectroscopic analysis. We conclude that in general terms our SED photometric
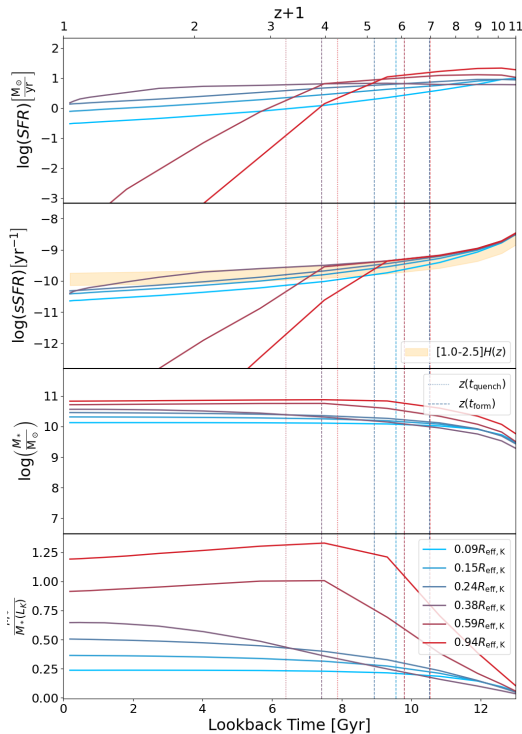
Figure C.3: NGC1194 evolution from photometry at different apertures.

analysis is consistent with the trends based on the most accurate spectroscopic results. Both of them support the idea that NGC1194 quenched due to the activity of its central SMBH.

C.4 NGC6086

As discussed previously NGC6086 is a retired galaxy, the most massive galaxy and host the most massive SMBH in our sample, with $M_*(L_K) \sim 10^{11.6}$ $M_\odot$ and $M_{\rm BH} \sim 10^{9.6}$ $M_\odot$, respectively. The evolution of its stellar population is shown in Figure C.4.

For the inner radii, we found that our results are inconsistent with their spectroscopic counterparts; photometric results show that it is star forming, in contrast to the spectroscopic results where the central parts are quiescent. As for the outer parts we found that are consistent with our spectroscopic results. Notice that our spectroscopic analysis was performed for three apertures only.

The resulting stellar populations within the inner apertures seem to be younger than what it was inferred by the spectroscopic analysis, getting younger
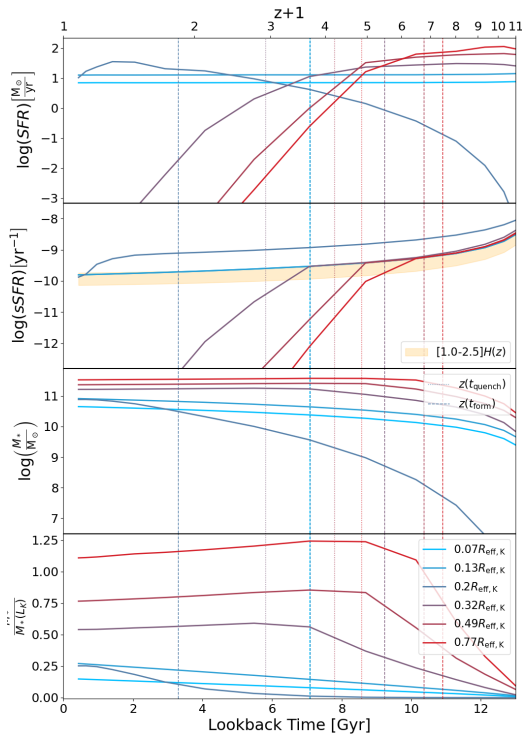
Figure C.4: NGC6086 evolution from photometry at different apertures.

populations for the inner apertures. This is not surprising given that the photometric analysis infers that the central part is star-forming.

C.5 NGC3982

There is no data for the radial surface brightness for NGC3982 in the *NUV* and *FUV* filters from GALEX. The above may lead to unreliable inferences of the SFH and the SMFH. Nonetheless, for completeness here we report the the broad-band fitting results for this galaxy.

Figure C.5 shows that the SFHs fitted for all the apertures are flat and with the $sSFR(z)$ above the Pacific criteria and all of them with similar redshifts of formation times $z \sim 0.8$. The above implies that this galaxy is still star forming at all radii in contrast to the spectroscopic results. As mentioned above, because of the fact that *FUV* and *NUV* bands were not used for the broad-band SED fitting, the model parameters are degenerated, in particular those describing the SFH, as it is evident in the corner plots shown in Appendix A.
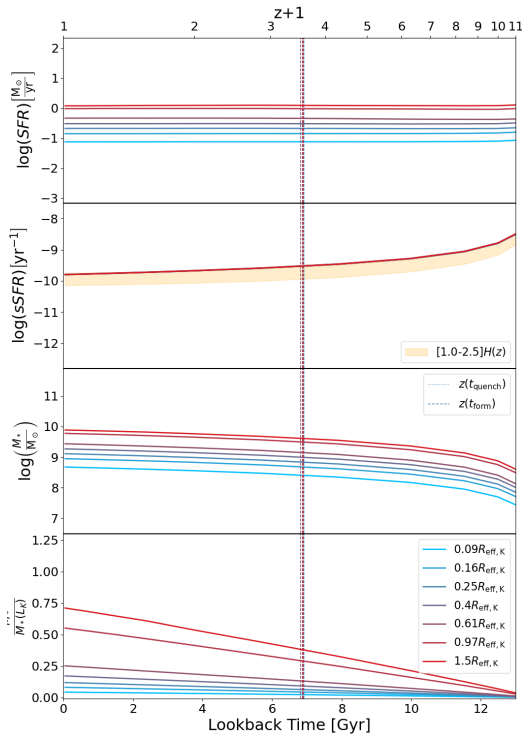
Figure C.5: NGC3982 evolution from photometry at different apertures.

C.6 NGC2960

NGC2960 is a galaxy hosting a Seyfert AGN with no contribution from the BLR nor the AGN continuum. The Figure C.6 shows that the fitted model of NGC2960 has older stellar populations at the outer apertures ($z(t_{\mathrm{form}}) > 1.0$), while the inner apertures have been formed very recently ($z(t_{\mathrm{form}}) \sim 0.1$). The SFH of the galaxy, for every aperture, also has a considerable falling slope in the SFR and the $sSFR$ at recent epochs, corresponding to quenching times of $z(t_{\mathrm{quench}}) < 1.0$ for the larger apertures, and even going to $z(t_{\mathrm{quench}}) < 0.1$ for the inner apertures. It is the outermost aperture ($R = 1.79\ R_{\mathrm{eff},K}$) the one with the closest approximation to the today $M_*(L_K)$ value.

C.7 NGC6264

The evolutionary history of NGC6264, classified as an AGN Type S2, is shown in Figure C.7. This galaxy has been star forming since early epochs, being $sSFR(z)$ above $2.5H(z)$ and having an increasing $SFR(z)$, $\forall z \leq 10$ with all
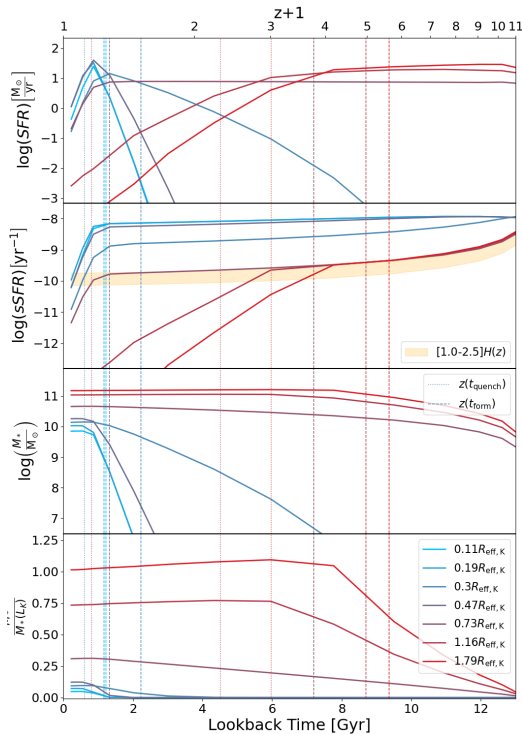
Figure C.6: NGC2960 evolution from photometry at different apertures.

the analysed apertures. This is equivalent to say that the galaxy has not been quenched at any analysed aperture, and therefore there is no t_{quench} reported.

For the outer apertures the populations are older, having flatter SFHs and t_{form} corresponding to $z(t_{\text{form}}) \sim 1.0$, while the inner apertures get younger stellar populations, with $z(t_{\text{form}}) \sim 0.1$ for the innermost. Finally none of the fitted apertures reach the value of $M_*(L_K)$ up to date, being the outermost aperture ($R = 0.89\ R_{\text{eff},K}$) the closest one, with a $M_*/M_*(L_K) \approx 0.8$.

C.8 NGC4395

As mentioned before, the less massive galaxy in our sample is the late type galaxy classified as an AGN Type S1.8, NGC4395. Its evolution is plotted in Figure C.8, which shows that it has been a star forming galaxy since early epochs $z \sim 10$, being the $sSFR$ above the Pacifici criteria at all epochs, i.e. it has not quenched yet. Furthermore, the galaxy has young stellar populations with $z(t_{\text{form}}) < 1.0$ for all the analyzed apertures, being much younger for the inner apertures (corresponding to $z(t_{\text{form}}) < 0.1$).
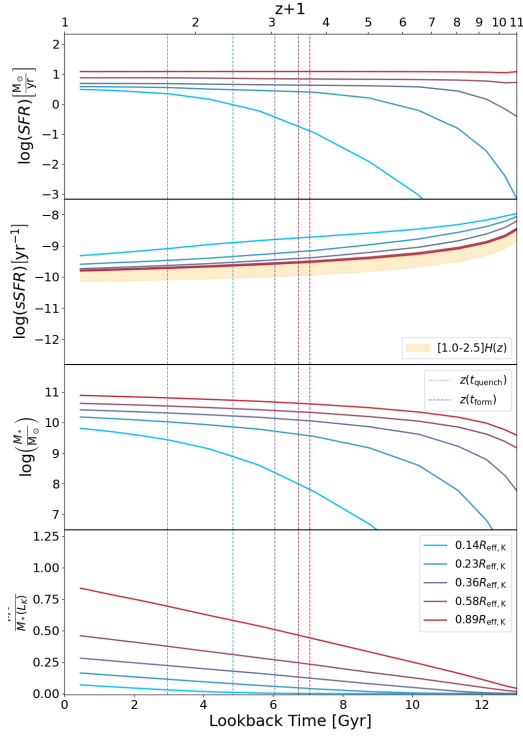
Figure C.7: NGC6264 evolution from photometry at different apertures.

Even if the stellar mass obtained from the K-luminosity is quite small $(M_*(L_K) = 10^{8.43}$ M$_\odot)$, none stellar mass of the fitted apertures get close to this value up to date, having $M_*/M_*(L_K) \approx 0.1$ for the outermost aperture.
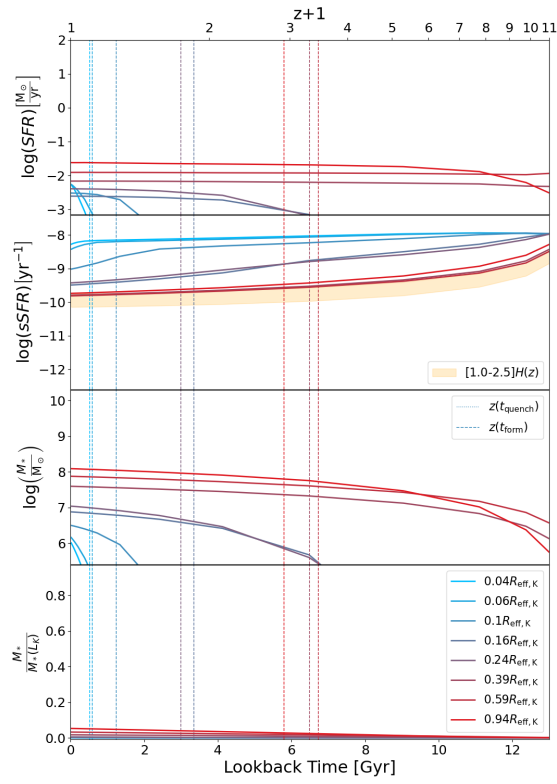
Figure C.8: NGC4395 evolution from photometry at different apertures.

Appendix D

List of Abbreviations and Variables

Abbreviations/variable	Meaning
AB_i	Absolute Magnitude of the Sun in the i-band
AGN	Active Galactic Nuclei
AMUSING++	All-weather MUse Integral-field of Nearby Galaxies++
A_V	Dust Attenuation
b/a	Axis Ratio
BB	Big Bang
BCG	Bright Cluster Galaxy
BH	Black Hole
CALIFA	Calar Alto Legaxy Integral Field Area Survey
CSP	Composite Stellar Population
D_L	Luminosity Distance
DAP	MaNGA Data Analysis Pipeline
DRP	MaNGA Data Reduction Pipeline
DR17	MaNGA 17th Data Release
DPL	Double Power Law (see Eq. 3.2)
FoV	Field of View
FUV	Far Ultraviolet
$FWHM$	Full Width at Half Maximum
H_0	Hubble Parameter at $z = 0$ (=70 km·s^{-1}·Mpc^{-1})
$H(z)$	Hubble Parameter
IFS	Integral Field Spectroscopy
IFU	Integral Field Unit
IMF	Initial Mass Function
ISM	Interstellar Medium
L_{bol}	Bolometric Luminosity

Table D.1: List of abbreviations and variables used in the text.

Abbreviations/variable	Meaning
L_K	Luminosity in the K-band
$L_\odot$	Solar luminosity $(= 3.828 \times 10^{33}$ erg$)^*$
m	Pogson Magnitude
MaNGA	Mapping Nearby Galaxies at Apache Point Observatory
$M_\odot$	Mass of the Sun $(= 1.988 \times 10^{33}$ g$)^*$
M_*	Stellar Mass
$M_{*,K}$	Stellar Mass inferred using L_K
$M_{*,\mathrm{bulge}}$	Bulge's Stellar Mass
$M_{*,\mathrm{formed}}$	Formed Stellar Mass
M_{BH}	Super Massive Black Hole's Mass
M_i	i-band Absolute Magnitude
MW	Mass Weighted
NIR	Near Infrared
NSA	NASA-Sloan Atlas
NUV	Near Ultraviolet
PA	Pitch Angle
PSF	Point Spread Function
QSO	Quasar
$R_{\mathrm{eff,K}}$	Effective Radius at K-band
$R_{\mathrm{eff,r(s)}}$	Effective Radius at r-band from Sersic fit
$R_{\mathrm{eff,r(p)}}$	Effective Radius at r-band from Petrosian fit
R_{max}	Maximum Aperture Within the FoV
SAMI	Sydney-AAO Multi-object Integral field spectrograph
SED	Spectral Energy Distribution
SF	Star Formation
SFH	Star Formation History
SFR	Star Formation Rate
SMBH	Super Massive Black Hole
SN	Supernova
SP	Stellar Population
SPS	Stellar Population Synthesis
$sSFR$	Specific Star Formation Rate
SSP	Single Stellar Population

Table D.2: Continuation of the list of abbreviations and variables used in the text. *From the resolution B3 of `https://www.iau.org/static/resolutions/IAU2015_English.pdf`).

Abbreviations/variable	Meaning
σ_*	Stellar Velocity Dispersion
$t_{\mathrm{Hubble}}(z)$	Hubble Time at z
$t_U(z)$	Age of the Universe at z
t_{form}	Formation Time
t_{quench}	Quenching Time
τ_{quench}	Quenching Scale
T_{eff}	Effective Temperature
UFO	Ultrafast X-ray Outflow
UV	Ultraviolet
μ	Mean Surface Brightness
VAC	Value Added Catalogues
$W_{H\alpha}$	Equivalent Width of Hα
WBL	Nearby Poor Cluster of Galaxies of White *et al.* (1999)
z	Redshift
Z_*	Stellar Metallicity
$\mathrm{Z}_\odot$	Solar Metallicity ($= 0.02$)

Table D.3: Continuation of the list of abbreviations and variables used in the text.

Bibliography

Abbott, B. P., Abbott, R., Abbott, T. D., *et al.* (2016). Observation of Gravitational Waves from a Binary Black Hole Merger. Physical Review Letters, 116(6):061102.

Abdurro'uf, Accetta, K., Aerts, C., *et al.* (2022). The Seventeenth Data Release of the Sloan Digital Sky Surveys: Complete Release of MaNGA, MaStar, and APOGEE-2 Data. The Astrophysical Journal Supplement Series, 259(2):35.

Antonucci, R. (1993). Unified models for active galactic nuclei and quasars. Annual Review of Astronomy & Astrophysics, 31:473–521.

Arp, H. (1966). Atlas of Peculiar Galaxies. The Astrophysical Journal Supplement Series, 14:1.

Baldwin, J. A., Phillips, M. M., Terlevich, R. (1981). Classification parameters for the emission-line spectra of extragalactic objects. The Publications of the Astronomical Society of the Pacific, 93:5–19.

Behroozi, P. S., Wechsler, R. H., Conroy, C. (2013). The Average Star Formation Histories of Galaxies in Dark Matter Halos from z = 0-8. The Astrophysical Journal, 770(1):57.

Beifiori, A., Courteau, S., Corsini, E. M., Zhu, Y. (2012). On the correlations between galaxy properties and supermassive black hole mass. Monthly Notices of the Royal Astronomical Society, 419(3):2497–2528.

Belczynski, K., Bulik, T., Fryer, C. L., *et al.* (2010). On the Maximum Mass of Stellar Black Holes. The Astrophysical Journal, 714(2):1217–1226.

Bell, E. F., Wolf, C., Meisenheimer, K., *et al.* (2004). Nearly 5000 Distant Early-Type Galaxies in COMBO-17: A Red Sequence and Its Evolution since z~1. The Astrophysical Journal, 608(2):752–767.

Benson, A. J., Bower, R. G., Frenk, C. S., *et al.* (2003). What Shapes the Luminosity Function of Galaxies? The Astrophysical Journal, 599(1):38–49.

Bentz, M. C., Walsh, J. L., Barth, A. J., *et al.* (2010). The Lick AGN Monitoring Project: Reverberation Mapping of Optical Hydrogen and Helium Recombination Lines. The Astrophysical Journal, 716(2):993–1011.

Bershady, M. A., Verheijen, M. A. W., Swaters, R. A., *et al.* (2010). The DiskMass Survey. I. Overview. The Astrophysical Journal, 716(1):198–233.

Bertelli, G., Bressan, A., Chiosi, C., *et al.* (1994). Theoretical isochrones from models with new radiative opacities. Astronomy and Astrophysics Suppl., 106:275–302.

Blanton, M. R., Bershady, M. A., Abolfathi, B., *et al.* (2017). Sloan Digital Sky Survey IV: Mapping the Milky Way, Nearby Galaxies, and the Distant Universe. The Astronomical Journal, 154(1):28.

Blanton, M. R. Roweis, S. (2007). K-Corrections and Filter Transformations in the Ultraviolet, Optical, and Near-Infrared. The Astronomical Journal, 133(2):734–754.

Bower, R. G., Benson, A. J., Malbon, R., *et al.* (2006). Breaking the hierarchy of galaxy formation. Monthly Notices of the Royal Astronomical Society, 370(2):645–655.

Bower, R. G., Schaye, J., Frenk, C. S., *et al.* (2017). The dark nemesis of galaxy formation: why hot haloes trigger black hole growth and bring star formation to an end. Monthly Notices of the Royal Astronomical Society, 465(1):32–44.

Brecher, K. (1976). Active galaxies. In Avrett, E. H., editor, Frontiers of Astrophysics, pp. 438–471.

Brinchmann, J., Charlot, S., White, S. D. M., *et al.* (2004). The physical properties of star-forming galaxies in the low-redshift Universe. Monthly Notices of the Royal Astronomical Society, 351(4):1151–1179.

Bruzual, G. Charlot, S. (2003). Stellar population synthesis at the resolution of 2003. Monthly Notices of the Royal Astronomical Society, 344(4):1000–1028.

Buchner, J., Georgakakis, A., Nandra, K., *et al.* (2014). X-ray spectral modelling of the AGN obscuring region in the CDFS: Bayesian model selection and catalogue. Astronomy & Astrophysics, 564:A125.

Bundy, K., Bershady, M. A., Law, D. R., *et al.* (2015). Overview of the SDSS-IV MaNGA Survey: Mapping nearby Galaxies at Apache Point Observatory. The Astrophysical Journal, 798(1):7.

Calzetti, D. (2001). The Dust Opacity of Star-forming Galaxies. The Publications of the Astronomical Society of the Pacific, 113(790):1449–1485.

Caplar, N. Tacchella, S. (2019). Stochastic modelling of star-formation histories I: the scatter of the star-forming main sequence. Monthly Notices of the Royal Astronomical Society, 487(3):3845–3869.

Cardelli, J. A., Clayton, G. C., Mathis, J. S. (1989). The Relationship between Infrared, Optical, and Ultraviolet Extinction. The Astrophysical Journal, 345:245.

Carnall, A. C., Leja, J., Johnson, B. D., *et al.* (2019a). How to Measure Galaxy Star Formation Histories. I. Parametric Models. The Astrophysical Journal, 873(1):44.

Carnall, A. C., McLeod, D. J., McLure, R. J., *et al.* (2023a). A surprising abundance of massive quiescent galaxies at $3 < z < 5$ in the first data from JWST CEERS. Monthly Notices of the Royal Astronomical Society.

Carnall, A. C., McLure, R. J., Dunlop, J. S., *et al.* (2019b). The VANDELS survey: the star-formation histories of massive quiescent galaxies at $1.0 < z < 1.3$. Monthly Notices of the Royal Astronomical Society, 490(1):417–439.

Carnall, A. C., McLure, R. J., Dunlop, J. S., Davé, R. (2018). Inferring the star formation histories of massive quiescent galaxies with BAGPIPES: evidence for multiple quenching mechanisms. Monthly Notices of the Royal Astronomical Society, 480(4):4379–4401.

Carnall, A. C., McLure, R. J., Dunlop, J. S., *et al.* (2023b). A massive quiescent galaxy at redshift 4.658. arXiv e-prints, p. arXiv:2301.11413.

Cattaneo, A., Dekel, A., Devriendt, J., *et al.* (2006). Modelling the galaxy bimodality: shutdown above a critical halo mass. Monthly Notices of the Royal Astronomical Society, 370(4):1651–1665.

Chabrier, G. (2003). Galactic Stellar and Substellar Initial Mass Function. The Publications of the Astronomical Society of the Pacific, 115(809):763–795.

Charlot, S. Fall, S. M. (2000). A Simple Model for the Absorption of Starlight by Dust in Galaxies. The Astrophysical Journal, 539(2):718–731.

Chen, Z., Faber, S. M., Koo, D. C., *et al.* (2020). Quenching as a Contest between Galaxy Halos and Their Central Black Holes. The Astrophysical Journal, 897(1):102.

Choi, E., Somerville, R. S., Ostriker, J. P., *et al.* (2018). The Role of Black Hole Feedback on Size and Structural Evolution in Massive Galaxies. The Astrophysical Journal, 866(2):91.

Cicone, C., Maiolino, R., Sturm, E., *et al.* (2014). Massive molecular outflows and evidence for AGN feedback from CO observations. Astronomy & Astrophysics, 562:A21.

Cid Fernandes, R., Stasińska, G., Mateus, A., Vale Asari, N. (2011). A comprehensive classification of galaxies in the Sloan Digital Sky Survey: how to tell true from fake AGN? Monthly Notices of the Royal Astronomical Society, 413(3):1687–1699.

Cid Fernandes, R., Stasińska, G., Schlickmann, M. S., *et al.* (2010). Alternative diagnostic diagrams and the 'forgotten' population of weak line galaxies in the SDSS. Monthly Notices of the Royal Astronomical Society, 403(2):1036–1053.

Cole, S., Lacey, C. G., Baugh, C. M., Frenk, C. S. (2000). Hierarchical galaxy formation. Monthly Notices of the Royal Astronomical Society, 319(1):168–204.

Condon, J. J., Cotton, W. D., Greisen, E. W., *et al.* (1998). The NRAO VLA Sky Survey. The Astronomical Journal, 115(5):1693–1716.

Conroy, C. (2013). Modeling the Panchromatic Spectral Energy Distributions of Galaxies. Annual Review of Astronomy & Astrophysics, 51(1):393–455.

Conroy, C. Gunn, J. E. (2010). The Propagation of Uncertainties in Stellar Population Synthesis Modeling. III. Model Calibration, Comparison, and Evaluation. The Astrophysical Journal, 712(2):833–857.

Conselice, C. J., Wilkinson, A., Duncan, K., Mortlock, A. (2016). The Evolution of Galaxy Number Density at z < 8 and Its Implications. The Astrophysical Journal, 830(2):83.

Cortes-Suárez, E., Negrete, C. A., Hernández-Toledo, H. M., *et al.* (2022). SDSS-IV MaNGA: Identification and multi-wavelength properties of Type-1 AGN in the DR15 sample. Monthly Notices of the Royal Astronomical Society, 514(3):3626–3649.

Croom, S. M., Lawrence, J. S., Bland-Hawthorn, J., *et al.* (2012). The Sydney-AAO Multi-object Integral field spectrograph. Monthly Notices of the Royal Astronomical Society, 421(1):872–893.

Croton, D. J. (2006). Evolution in the black hole mass-bulge mass relation: a theoretical perspective. Monthly Notices of the Royal Astronomical Society, 369(4):1808–1812.

Croton, D. J., Springel, V., White, S. D. M., *et al.* (2006). The many lives of active galactic nuclei: cooling flows, black holes and the luminosities and colours of galaxies. Monthly Notices of the Royal Astronomical Society, 365(1):11–28.

da Cunha, E., Charlot, S., Elbaz, D. (2008). A simple model to interpret the ultraviolet, optical and infrared emission from galaxies. Monthly Notices of the Royal Astronomical Society, 388(4):1595–1617.

de Vaucouleurs, G., de Vaucouleurs, A., Corwin, J. R. (1976). Second reference catalogue of bright galaxies. Second reference catalogue of bright galaxies, 1976:0.

Dekel, A., Lapiner, S., Dubois, Y. (2019). Origin of the Golden Mass of Galaxies and Black Holes. arXiv e-prints, p. arXiv:1904.08431.

den Brok, M., Seth, A. C., Barth, A. J., *et al.* (2015). Measuring the Mass of the Central Black Hole in the Bulgeless Galaxy NGC 4395 from Gas Dynamical Modeling. The Astrophysical Journal, 809(1):101.

Denney, K. D., Peterson, B. M., Pogge, R. W., *et al.* (2010). Reverberation Mapping Measurements of Black Hole Masses in Six Local Seyfert Galaxies. The Astrophysical Journal, 721(1):715–737.

Diemer, B., Sparre, M., Abramson, L. E., Torrey, P. (2017). Lognormal Star Formation Histories in Simulated and Observed Galaxies. The Astrophysical Journal, 839(1):26.

DiPompeo, M. A., Hickox, R. C., Carroll, C. M., *et al.* (2018). The [O III] Profiles of Infrared-selected Active Galactic Nuclei: More Powerful Outflows in the Obscured Population. The Astrophysical Journal, 856(1):76.

Drory, N., MacDonald, N., Bershady, M. A., *et al.* (2015). The MaNGA Integral Field Unit Fiber Feed System for the Sloan 2.5 m Telescope. The Astronomical Journal, 149(2):77.

Dubois, Y., Peirani, S., Pichon, C., *et al.* (2016). The HORIZON-AGN simulation: morphological diversity of galaxies promoted by AGN feedback. Monthly Notices of the Royal Astronomical Society, 463(4):3948–3964.

Dutton, A. A. van den Bosch, F. C. (2009). The impact of feedback on disc galaxy scaling relations. Monthly Notices of the Royal Astronomical Society, 396(1):141–164.

Elbert, O. D., Bullock, J. S., Kaplinghat, M. (2018). Counting black holes: The cosmic stellar remnant population and implications for LIGO. Monthly Notices of the Royal Astronomical Society, 473(1):1186–1194.

Faber, S., Tinsley, B. M., Larson, R. B., Gehret, D. C. (1977). Evolution of galaxies and stellar populations.

Faber, S. M. (1972). Quadratic programming applied to the problem of galaxy population synthesis. Astronomy & Astrophysics, 20:361.

Faber, S. M., Willmer, C. N. A., Wolf, C., et al. (2007). Galaxy Luminosity Functions to z~1 from DEEP2 and COMBO-17: Implications for Red Galaxy Formation. The Astrophysical Journal, 665(1):265–294.

Falcón-Barroso, J., Sánchez-Blázquez, P., Vazdekis, A., et al. (2011). An updated MILES stellar library and stellar population models. Astronomy & Astrophysics, 532:A95.

Fang, J. J., Faber, S. M., Koo, D. C., Dekel, A. (2013). A Link between Star Formation Quenching and Inner Stellar Mass Density in Sloan Digital Sky Survey Central Galaxies. The Astrophysical Journal, 776(1):63.

Faucher-Giguère, C.-A. Quataert, E. (2012). The physics of galactic winds driven by active galactic nuclei. Monthly Notices of the Royal Astronomical Society, 425(1):605–622.

Ferland, G. J., Chatzikos, M., Guzmán, F., et al. (2017). The 2017 Release Cloudy. Revista Mexicana de Astronomía y Astrofísica, 53:385–438.

Feroz, F. Hobson, M. P. (2008). Multimodal nested sampling: an efficient and robust alternative to Markov Chain Monte Carlo methods for astronomical data analyses. Monthly Notices of the Royal Astronomical Society, 384(2):449–463.

Feroz, F., Hobson, M. P., Bridges, M. (2009). MULTINEST: an efficient and robust Bayesian inference tool for cosmology and particle physics. Monthly Notices of the Royal Astronomical Society, 398(4):1601–1614.

Feroz, F., Hobson, M. P., Cameron, E., Pettitt, A. N. (2019). Importance Nested Sampling and the MultiNest Algorithm. The Open Journal of Astrophysics, 2(1):10.

Ferrarese, L. Ford, H. (2005). Supermassive Black Holes in Galactic Nuclei: Past, Present and Future Research. Space Science Reviews, 116(3-4):523–624.

Ferrarese, L. Merritt, D. (2000). A Fundamental Relation between Supermassive Black Holes and Their Host Galaxies. The Astrophysical Journal Letters, 539(1):L9–L12.

Fiore, F., Feruglio, C., Shankar, F., *et al.* (2017). AGN wind scaling relations and the co-evolution of black holes and galaxies. Astronomy & Astrophysics, 601:A143.

Firmani, C. Avila-Reese, V. (2000). Disc galaxy evolution models in a hierarchical formation scenario: structure and dynamics. Monthly Notices of the Royal Astronomical Society, 315(3):457–472.

Fouque, P., Gourgoulhon, E., Chamaraux, P., Paturel, G. (1992). Groups of galaxies within 80 Mpc. II. The catalogue of groups and group members. Astronomy and Astrophysics Suppl., 93:211–233.

Frenk, C. S. White, S. D. M. (2012). Dark matter and cosmic structure. Annalen der Physik, 524(9-10):507–534.

Frogel, J. A. (1988). The galactic nuclear bulge and the stellar content of spheroidal systems. Annual Review of Astronomy & Astrophysics, 26:51–92.

Gallazzi, A., Charlot, S., Brinchmann, J., *et al.* (2005). The ages and metallicities of galaxies in the local universe. Monthly Notices of the Royal Astronomical Society, 362(1):41–58.

Garcia, A. M. (1993). General study of group membership. II. Determination of nearby groups. Astronomy and Astrophysics Suppl., 100:47–90.

Gebhardt, K., Bender, R., Bower, G., *et al.* (2000). A Relationship between Nuclear Black Hole Mass and Galaxy Velocity Dispersion. The Astrophysical Journal Letters, 539(1):L13–L16.

Geller, M. J. Huchra, J. P. (1983). Groups of galaxies. III. THe CfA survey. The Astrophysical Journal Supplement Series, 52:61–87.

Gies, D. R. Bolton, C. T. (1986). The Optical Spectrum of HDE 226868=Cygnus X-1. II. Spectrophotometry and Mass Estimates. The Astrophysical Journal, 304:371.

Graham, A. W. Soria, R. (2019). Expected intermediate-mass black holes in the Virgo cluster - I. Early-type galaxies. Monthly Notices of the Royal Astronomical Society, 484(1):794–813.

Graham, A. W., Soria, R., Davis, B. L. (2019). Expected intermediate-mass black holes in the Virgo cluster - II. Late-type galaxies. Monthly Notices of the Royal Astronomical Society, 484(1):814–831.

Green, R. F., Schmidt, M., Liebert, J. (1986). The Palomar-Green Catalog of Ultraviolet-Excess Stellar Objects. The Astrophysical Journal Supplement Series, 61:305.

Greene, J. E. Ho, L. C. (2005). Estimating Black Hole Masses in Active Galaxies Using the Hα Emission Line. The Astrophysical Journal, 630(1):122–129.

Greiner, J., Cuby, J. G., McCaughrean, M. J. (2001). An unusually massive stellar black hole in the Galaxy. Nature, 414(6863):522–525.

Gunn, J. E., Siegmund, W. A., Mannery, E. J., et al. (2006). The 2.5 m Telescope of the Sloan Digital Sky Survey. The Astronomical Journal, 131(4):2332–2359.

Hickox, R. C. Alexander, D. M. (2018). Obscured Active Galactic Nuclei. Annual Review of Astronomy & Astrophysics, 56:625–671.

Hoessel, J. G., Gunn, J. E., Thuan, T. X. (1980). The photometry properties of brightest cluster galaxies. I. Absolute magnitudes in 116 nearby Abell clusters. The Astrophysical Journal, 241:486–492.

Hopkins, P. F., Cox, T. J., Kereš, D., Hernquist, L. (2008a). A Cosmological Framework for the Co-Evolution of Quasars, Supermassive Black Holes, and Elliptical Galaxies. II. Formation of Red Ellipticals. The Astrophysical Journal Supplement Series, 175(2):390–422.

Hopkins, P. F., Hernquist, L., Cox, T. J., Kereš, D. (2008b). A Cosmological Framework for the Co-Evolution of Quasars, Supermassive Black Holes, and Elliptical Galaxies. I. Galaxy Mergers and Quasar Activity. The Astrophysical Journal Supplement Series, 175(2):356–389.

Hopkins, P. F., Somerville, R. S., Hernquist, L., et al. (2006). The Relation between Quasar and Merging Galaxy Luminosity Functions and the Merger-driven Star Formation History of the Universe. The Astrophysical Journal, 652(2):864–888.

Hopkins, P. F., Torrey, P., Faucher-Giguère, C.-A., et al. (2016). Stellar and quasar feedback in concert: effects on AGN accretion, obscuration, and outflows. Monthly Notices of the Royal Astronomical Society, 458(1):816–831.

Huchra, J. P. Geller, M. J. (1982). Groups of Galaxies. I. Nearby groups. The Astrophysical Journal, 257:423–437.

Igo, Z., Parker, M. L., Matzeu, G. A., et al. (2020). Searching for ultra-fast outflows in AGN using variability spectra. Monthly Notices of the Royal Astronomical Society, 493(1):1088–1108.

Ilbert, O., McCracken, H. J., Le Fèvre, O., *et al.* (2013). Mass assembly in quiescent and star-forming galaxies since z 4 from UltraVISTA. Astronomy & Astrophysics, 556:A55.

Iyer, K. G., Tacchella, S., Genel, S., *et al.* (2020). The diversity and variability of star formation histories in models of galaxy evolution. Monthly Notices of the Royal Astronomical Society, 498(1):430–463.

Kaiser, M. E., Lee, J. C., Kriss, G. A., *et al.* (2006). Intrinsic FUV Absorption in Mrk290. In Sonneborn, G., Moos, H. W., Andersson, B. G., editores, Astrophysics in the Far Ultraviolet: Five Years of Discovery with FUSE, volume 348 of Astronomical Society of the Pacific Conference Series, p. 522.

Kauffmann, G. (1996). Disc galaxies at z=0 and at high redshift: an explanation of the observed evolution of damped Lyalpha absorption systems. Monthly Notices of the Royal Astronomical Society, 281(2):475–486.

Kauffmann, G., Heckman, T. M., Tremonti, C., *et al.* (2003). The host galaxies of active galactic nuclei. Monthly Notices of the Royal Astronomical Society, 346(4):1055–1077.

Keel, W. C. (1985). Two active galaxies with tidal tails and companions. The Astronomical Journal, 90:1449–1456.

Kennicutt, Robert C., J. (1998). The Global Schmidt Law in Star-forming Galaxies. The Astrophysical Journal, 498(2):541–552.

Kewley, L. J., Dopita, M. A., Sutherland, R. S., *et al.* (2001). Theoretical Modeling of Starburst Galaxies. The Astrophysical Journal, 556(1):121–140.

Kewley, L. J., Groves, B., Kauffmann, G., Heckman, T. (2006). The host galaxies and classification of active galactic nuclei. Monthly Notices of the Royal Astronomical Society, 372(3):961–976.

Khachikian, E. Y. Weedman, D. W. (1974). An atlas of Seyfert galaxies. The Astrophysical Journal, 192:581–589.

Kocevski, D. D., Barro, G., Faber, S. M., *et al.* (2017). CANDELS: Elevated Black Hole Growth in the Progenitors of Compact Quiescent Galaxies at z $\sim$ 2. The Astrophysical Journal, 846(2):112.

Kormendy, J. Ho, L. C. (2013). Coevolution (Or Not) of Supermassive Black Holes and Host Galaxies. Annual Review of Astronomy & Astrophysics, 51(1):511–653.

Kriss, G. A., Lee, J. C., Danehkar, A. (2018). A Search for H I Lyα Counterparts to Ultrafast X-Ray Outflows. The Astrophysical Journal, 859(2):94.

Kroupa, P. Boily, C. M. (2002). On the mass function of star clusters. Monthly Notices of the Royal Astronomical Society, 336(4):1188–1194.

Kuo, C. Y., Braatz, J. A., Condon, J. J., *et al.* (2011). The Megamaser Cosmology Project. III. Accurate Masses of Seven Supermassive Black Holes in Active Galaxies with Circumnuclear Megamaser Disks. The Astrophysical Journal, 727(1):20.

Lacerda, E. A. D., Sánchez, S. F., Mejía-Narváez, A., *et al.* (2022). pyFIT3D and pyPipe3D - The new version of the integral field spectroscopy data analysis pipeline. New Astronomy, 97:101895.

Lada, C. J. Lada, E. A. (2003). Embedded Clusters in Molecular Clouds. Annual Review of Astronomy & Astrophysics, 41:57–115.

Lange, R., Driver, S. P., Robotham, A. S. G., *et al.* (2015). Galaxy And Mass Assembly (GAMA): mass-size relations of z < 0.1 galaxies subdivided by Sérsic index, colour and morphology. Monthly Notices of the Royal Astronomical Society, 447(3):2603–2630.

Lapiner, S., Dekel, A., Freundlich, J., *et al.* (2023). Wet Compaction to a Blue Nugget: a Critical Phase in Galaxy Evolution. arXiv e-prints, p. arXiv:2302.12234.

Law, D. R., Cherinka, B., Yan, R., *et al.* (2016). The Data Reduction Pipeline for the SDSS-IV MaNGA IFU Galaxy Survey. The Astronomical Journal, 152(4):83.

Law, D. R., Westfall, K. B., Bershady, M. A., *et al.* (2021). SDSS-IV MaNGA: Modeling the Spectral Line-spread Function to Subpercent Accuracy. The Astronomical Journal, 161(2):52.

Lawrence, A. (1987). Classification of active galaxies and the prospect of a unified phenomenology. The Publications of the Astronomical Society of the Pacific, 99:309–334.

Leja, J., Johnson, B. D., Conroy, C., *et al.* (2017). Deriving Physical Properties from Broadband Photometry with Prospector: Description of the Model and a Demonstration of its Accuracy Using 129 Galaxies in the Local Universe. The Astrophysical Journal, 837(2):170.

Lilly, S. J., Carollo, C. M., Pipino, A., *et al.* (2013). Gas Regulation of Galaxies: The Evolution of the Cosmic Specific Star Formation Rate, the Metallicity-Mass-Star-formation Rate Relation, and the Stellar Content of Halos. The Astrophysical Journal, 772(2):119.

López-Cobá, C., Sánchez, S. F., Anderson, J. P., *et al.* (2020). The AMUS-ING++ Nearby Galaxy Compilation. I. Full Sample Characterization and Galactic-scale Outflow Selection. The Astronomical Journal, 159(4):167.

Luo, Y., Faber, S. M., Rodríguez-Puebla, A., *et al.* (2020). Structural and stellar-population properties versus bulge types in Sloan Digital Sky Survey central galaxies. Monthly Notices of the Royal Astronomical Society, 493(2):1686–1707.

Lynden-Bell, D. (1969). Galactic Nuclei as Collapsed Old Quasars. Nature, 223(5207):690–694.

Lynden-Bell, D. Rees, M. J. (1971). On quasars, dust and the galactic centre. Monthly Notices of the Royal Astronomical Society, 152:461.

Magorrian, J., Tremaine, S., Richstone, D., *et al.* (1998). The Demography of Massive Dark Objects in Galaxy Centers. The Astronomical Journal, 115(6):2285–2305.

Mahtessian, A. P. (1998). Groups of Galaxies. III. Some Empirical Characteristics. Astrofizika, 41:308.

Maraston, C. (1998). Evolutionary synthesis of stellar populations: a modular tool. Monthly Notices of the Royal Astronomical Society, 300(3):872–892.

Markarian, B. E. (1967). Galaxies with an ultraviolet continuum. Astrofizika, 3:24–38.

Markarian, B. E. (1969). Galaxies with ultraviolet continuum. III. Astrofizika, 5:286–301.

Markarian, B. E., Lipovetskii, V. A., Stepanian, D. A. (1981). Galaxies with ultraviolet continuum. XV. Astrofizika, 17:619–627.

Martin, D. C., Fanson, J., Schiminovich, D., *et al.* (2005). The Galaxy Evolution Explorer: A Space Ultraviolet Survey Mission. The Astrophysical Journal Letters, 619(1):L1–L6.

McConnell, N. J., Ma, C.-P., Graham, J. R., *et al.* (2011). The Black Hole Mass in the Brightest Cluster Galaxy NGC 6086. The Astrophysical Journal, 728(2):100.

McKee, C. F. Ostriker, E. C. (2007). Theory of Star Formation. Annual Review of Astronomy & Astrophysics, 45(1):565–687.

Merloni, A. Heinz, S. (2008). A synthesis model for AGN evolution: supermassive black holes growth and feedback modes. Monthly Notices of the Royal Astronomical Society, 388(3):1011–1030.

Merloni, A., Rudnick, G., Di Matteo, T. (2004). Tracing the cosmological assembly of stars and supermassive black holes in galaxies. Monthly Notices of the Royal Astronomical Society, 354(3):L37–L42.

Miller, J. M., Fabbiano, G., Miller, M. C., Fabian, A. C. (2003). X-Ray Spectroscopic Evidence for Intermediate-Mass Black Holes: Cool Accretion Disks in Two Ultraluminous X-Ray Sources. The Astrophysical Journal Letters, 585(1):L37–L40.

Miller, M. C. Colbert, E. J. M. (2004). Intermediate-Mass Black Holes. International Journal of Modern Physics D, 13(1):1–64.

Miyauchi-Isobe, N., Nakajima, K., Maehara, H. (2004). The Kiso Survey for Ultraviolet-excess Galaxies (KUG). In Ochsenbein, F., Allen, M. G., Egret, D., editores, Astronomical Data Analysis Software and Systems (ADASS) XIII, volume 314 of Astronomical Society of the Pacific Conference Series, p. 161.

Mo, H., van den Bosch, F. C., White, S. (2010). Galaxy Formation and Evolution.

Mullaney, J. R., Alexander, D. M., Fine, S., et al. (2013). Narrow-line region gas kinematics of 24 264 optically selected AGN: the radio connection. Monthly Notices of the Royal Astronomical Society, 433(1):622–638.

Muzzin, A., Marchesini, D., Stefanon, M., et al. (2013). The Evolution of the Stellar Mass Functions of Star-forming and Quiescent Galaxies to z = 4 from the COSMOS/UltraVISTA Survey. The Astrophysical Journal, 777(1):18.

Netzer, H. (2015). Revisiting the Unified Model of Active Galactic Nuclei. Annual Review of Astronomy & Astrophysics, 53:365–408.

Noyola, E., Gebhardt, K., Bergmann, M. (2008). Gemini and Hubble Space Telescope Evidence for an Intermediate-Mass Black Hole in ω Centauri. The Astrophysical Journal, 676(2):1008–1015.

O'Connell, R. W. (1999). Far-Ultraviolet Radiation from Elliptical Galaxies. Annual Review of Astronomy & Astrophysics, 37:603–648.

O'Dell, S. L. (1986). The optical continuum emission of active galactic nuclei. The Publications of the Astronomical Society of the Pacific, 98:140–147.

O'Dell, S. L., Scott, H. A., Stein, W. A. (1987). The Origin of the Photoionizing Continuum of Active Galactic Nuclei and Quasars. The Astrophysical Journal, 313:164.

Orosz, J. A. (2003). Inventory of black hole binaries. In van der Hucht, K., Herrero, A., Esteban, C., editores, A Massive Star Odyssey: From Main Sequence to Supernova, volume 212, p. 365.

Osterbrock, D. E. Ferland, G. J. (2006). Astrophysics of gaseous nebulae and active galactic nuclei.

Pacifici, C., Kassin, S. A., Weiner, B. J., et al. (2016). The Evolution of Star Formation Histories of Quiescent Galaxies. The Astrophysical Journal, 832(1):79.

Padovani, P. (2017). On the two main classes of active galactic nuclei. Nature Astronomy, 1:0194.

Pandya, V., Fielding, D. B., Bryan, G. L., et al. (2022). A unified model for the co-evolution of galaxies and their circumgalactic medium: the relative roles of turbulence and atomic cooling physics. arXiv e-prints, p. arXiv:2211.09755.

Panter, B., Heavens, A. F., Jimenez, R. (2004). The mass function of the stellar component of galaxies in the Sloan Digital Sky Survey. Monthly Notices of the Royal Astronomical Society, 355(3):764–768.

Peng, Y.-j., Lilly, S. J., Kovač, K., et al. (2010). Mass and Environment as Drivers of Galaxy Evolution in SDSS and zCOSMOS and the Origin of the Schechter Function. The Astrophysical Journal, 721(1):193–221.

Peterson, B. M., Bentz, M. C., Desroches, L.-B., et al. (2005). Multiwavelength Monitoring of the Dwarf Seyfert 1 Galaxy NGC 4395. I. A Reverberation-based Measurement of the Black Hole Mass. The Astrophysical Journal, 632(2):799–808.

Pforr, J., Maraston, C., Tonini, C. (2012). Recovering galaxy stellar population properties from broad-band spectral energy distribution fitting. Monthly Notices of the Royal Astronomical Society, 422(4):3285–3326.

Pietrinferni, A., Cassisi, S., Salaris, M., Castelli, F. (2004). A Large Stellar Evolution Database for Population Synthesis Studies. I. Scaled Solar Models and Isochrones. The Astrophysical Journal, 612(1):168–190.

Postman, M. Lauer, T. R. (1995). Brightest Cluster Galaxies as Standard Candles. The Astrophysical Journal, 440:28.

Prantzos, N. Boissier, S. (2000). Chemo-spectrophotometric evolution of spiral galaxies - III. Abundance and colour gradients in discs. Monthly Notices of the Royal Astronomical Society, 313(2):338–346.

Reines, A. E. Volonteri, M. (2015). Relations between Central Black Hole Mass and Total Galaxy Stellar Mass in the Local Universe. The Astrophysical Journal, 813(2):82.

Richstone, D., Ajhar, E. A., Bender, R., *et al.* (1998). Supermassive black holes and the evolution of galaxies. Nature, 385(6701):A14.

Rodríguez-Puebla, A., Calette, A. R., Avila-Reese, V., *et al.* (2020). The bivariate gas-stellar mass distributions and the mass functions of early- and late-type galaxies at z ∼ 0. Publications of the Astronomical Society of Australia, 37:e024.

Rodríguez-Puebla, A., Primack, J. R., Avila-Reese, V., Faber, S. M. (2017). Constraining the galaxy-halo connection over the last 13.3 Gyr: star formation histories, galaxy mergers and structural properties. Monthly Notices of the Royal Astronomical Society, 470(1):651–687.

Salim, S., Boquien, M., Lee, J. C. (2018). Dust Attenuation Curves in the Local Universe: Demographics and New Laws for Star-forming Galaxies and High-redshift Analogs. The Astrophysical Journal, 859(1):11.

Salim, S. Narayanan, D. (2020). The Dust Attenuation Law in Galaxies. Annual Review of Astronomy & Astrophysics, 58:529–575.

Salpeter, E. E. (1955). The Luminosity Function and Stellar Evolution. The Astrophysical Journal, 121:161.

Salpeter, E. E. (1964). Accretion of Interstellar Matter by Massive Objects. The Astrophysical Journal, 140:796–800.

Sánchez, S. F., Avila-Reese, V., Hernandez-Toledo, H., *et al.* (2018). SDSS IV MaNGA - Properties of AGN Host Galaxies. Revista Mexicana de Astronomía y Astrofísica, 54:217–260.

Sánchez, S. F., Barrera-Ballesteros, J. K., Lacerda, E., *et al.* (2022). SDSS-IV MaNGA: pyPipe3D Analysis Release for 10,000 Galaxies. The Astrophysical Journal Supplement Series, 262(2):36.

Sánchez, S. F., Kennicutt, R. C., Gil de Paz, A., *et al.* (2012). CALIFA, the Calar Alto Legacy Integral Field Area survey. I. Survey presentation. Astronomy & Astrophysics, 538:A8.

Sánchez, S. F., Pérez, E., Sánchez-Blázquez, P., *et al.* (2016a). Pipe3D, a pipeline to analyze Integral Field Spectroscopy Data: II. Analysis sequence and CALIFA dataproducts. Revista Mexicana de Astronomía y Astrofísica, 52:171–220.

Sánchez, S. F., Pérez, E., Sánchez-Blázquez, P., *et al.* (2016b). Pipe3D, a pipeline to analyze Integral Field Spectroscopy Data: I. New fitting philosophy of FIT3D. Revista Mexicana de Astronomía y Astrofísica, 52:21–53.

Sargent, W. L. W. (1970). A Spectroscopic Survey of Compact and Peculiar Galaxies. The Astrophysical Journal, 160:405.

Savorgnan, G. A. D. Graham, A. W. (2015). Overmassive black holes in the M_{BH}-σ diagram do not belong to over (dry) merged galaxies. Monthly Notices of the Royal Astronomical Society, 446(3):2330–2336.

Scalo, J. M. (1986). The Stellar Initial Mass Function. Fundamentals of Cosmic Physics, 11:1–278.

Schaller, G., Schaerer, D., Meynet, G., Maeder, A. (1992). New Grids of Stellar Models from 0.8-SOLAR-MASS to 120-SOLAR-MASSES at Z=0.020 and Z=0.001. Astronomy and Astrophysics Suppl., 96:269.

Schawinski, K., Thomas, D., Sarzi, M., *et al.* (2007). Observational evidence for AGN feedback in early-type galaxies. Monthly Notices of the Royal Astronomical Society, 382(4):1415–1431.

Schlegel, D. J., Finkbeiner, D. P., Davis, M. (1998). Maps of Dust Infrared Emission for Use in Estimation of Reddening and Cosmic Microwave Background Radiation Foregrounds. The Astrophysical Journal, 500(2):525–553.

Schmidt, M. Green, R. F. (1983). Quasar evolution derived from the Palomar bright quasar survey and other complete quasar surveys. The Astrophysical Journal, 269:352–374.

Schutte, Z., Reines, A. E., Greene, J. E. (2019). The Black Hole-Bulge Mass Relation Including Dwarf Galaxies Hosting Active Galactic Nuclei. The Astrophysical Journal, 887(2):245.

Sexton, R. O., Matzko, W., Darden, N., *et al.* (2021). Bayesian AGN Decomposition Analysis for SDSS spectra: a correlation analysis of [O III] λ5007 outflow kinematics with AGN and host galaxy properties. Monthly Notices of the Royal Astronomical Society, 500(3):2871–2895.

Shankar, F., Bernardi, M., Haiman, Z. (2009). The Evolution of the M_{BH}-σ Relation Inferred from the Age Distribution of Local Early-Type Galaxies and

Active Galactic Nuclei Evolution. The Astrophysical Journal, 694(2):867–878.

Sijacki, D., Springel, V., Di Matteo, T., Hernquist, L. (2007). A unified model for AGN feedback in cosmological simulations of structure formation. Monthly Notices of the Royal Astronomical Society, 380(3):877–900.

Silk, J. Rees, M. J. (1998). Quasars and galaxy formation. Astronomy & Astrophysics, 331:L1–L4.

Silverman, J. D., Green, P. J., Barkhouse, W. A., et al. (2008). The Luminosity Function of X-Ray-selected Active Galactic Nuclei: Evolution of Supermassive Black Holes at High Redshift. The Astrophysical Journal, 679(1):118–139.

Simha, V., Weinberg, D. H., Conroy, C., et al. (2014). Parametrising Star Formation Histories. arXiv e-prints, p. arXiv:1404.0402.

Skilling, J. (2006). Nested sampling for general Bayesian computation. Bayesian Analysis, 1(4):833 – 859.

Smee, S. A., Gunn, J. E., Uomoto, A., et al. (2013). The Multi-object, Fiber-fed Spectrographs for the Sloan Digital Sky Survey and the Baryon Oscillation Spectroscopic Survey. The Astronomical Journal, 146(2):32.

Somerville, R. S., Behroozi, P., Pandya, V., et al. (2018). The relationship between galaxy and dark matter halo size from $z \sim 3$ to the present. Monthly Notices of the Royal Astronomical Society, 473(2):2714–2736.

Somerville, R. S. Davé, R. (2015). Physical Models of Galaxy Formation in a Cosmological Framework. Annual Review of Astronomy & Astrophysics, 53:51–113.

Spinrad, H. Taylor, B. J. (1971). The Stellar Content of the Nuclei of Nearby Galaxies. I. M31, M32, and M81. The Astrophysical Journal Supplement Series, 22:445.

Springel, V. Hernquist, L. (2003). The history of star formation in a Λ cold dark matter universe. Monthly Notices of the Royal Astronomical Society, 339(2):312–334.

Steinmetz, M. Mueller, E. (1994). The formation of disk galaxies in a cosmological context: Populations, metallicities and metallicity gradients. Astronomy & Astrophysics, 281(3):L97–L100.

Stoughton, C., Lupton, R. H., Bernardi, M., et al. (2002). Sloan Digital Sky Survey: Early Data Release. The Astronomical Journal, 123(1):485–548.

Stringer, M. J. Benson, A. J. (2007). The formation of galaxy discs in a hierarchical universe. Monthly Notices of the Royal Astronomical Society, 382(2):641–651.

Sturm, E., González-Alfonso, E., Veilleux, S., et al. (2011). Massive Molecular Outflows and Negative Feedback in ULIRGs Observed by Herschel-PACS. The Astrophysical Journal Letters, 733(1):L16.

Tacchella, S., Dekel, A., Carollo, C. M., et al. (2016a). Evolution of density profiles in high-z galaxies: compaction and quenching inside-out. Monthly Notices of the Royal Astronomical Society, 458(1):242–263.

Tacchella, S., Dekel, A., Carollo, C. M., et al. (2016b). The confinement of star-forming galaxies into a main sequence through episodes of gas compaction, depletion and replenishment. Monthly Notices of the Royal Astronomical Society, 457(3):2790–2813.

Tacchella, S., Forbes, J. C., Caplar, N. (2020). Stochastic modelling of star-formation histories II: star-formation variability from molecular clouds and gas inflow. Monthly Notices of the Royal Astronomical Society, 497(1):698–725.

Taylor, E. N., Hopkins, A. M., Baldry, I. K., et al. (2015). Galaxy And Mass Assembly (GAMA): deconstructing bimodality - I. Red ones and blue ones. Monthly Notices of the Royal Astronomical Society, 446(2):2144–2185.

Terrazas, B. A., Bell, E. F., Henriques, B. M. B., et al. (2016). Quiescence Correlates Strongly with Directly Measured Black Hole Mass in Central Galaxies. The Astrophysical Journal Letters, 830(1):L12.

Terrazas, B. A., Bell, E. F., Woo, J., Henriques, B. M. B. (2017). Supermassive Black Holes as the Regulators of Star Formation in Central Galaxies. The Astrophysical Journal, 844(2):170.

Tinsley, B. M. (1972). Galactic Evolution. Astronomy & Astrophysics, 20:383.

Tinsley, B. M. (1980). Evolution of the Stars and Gas in Galaxies. Fundamentals of Cosmic Physics, 5:287–388.

Tombesi, F., Cappi, M., Reeves, J. N., et al. (2010). Evidence for ultra-fast outflows in radio-quiet AGNs. I. Detection and statistical incidence of Fe K-shell absorption lines. Astronomy & Astrophysics, 521:A57.

Tremaine, S., Gebhardt, K., Bender, R., et al. (2002). The Slope of the Black Hole Mass versus Velocity Dispersion Correlation. The Astrophysical Journal, 574(2):740–753.

Trump, J. R., Hsu, A. D., Fang, J. J., *et al.* (2013a). A Census of Broad-line Active Galactic Nuclei in Nearby Galaxies: Coeval Star Formation and Rapid Black Hole Growth. The Astrophysical Journal, 763(2):133.

Trump, J. R., Konidaris, N. P., Barro, G., *et al.* (2013b). Testing Diagnostics of Nuclear Activity and Star Formation in Galaxies at z > 1. The Astrophysical Journal Letters, 763(1):L6.

Trump, J. R., Sun, M., Zeimann, G. R., *et al.* (2015). The Biases of Optical Line-Ratio Selection for Active Galactic Nuclei and the Intrinsic Relationship between Black Hole Accretion and Galaxy Star Formation. The Astrophysical Journal, 811(1):26.

Tucci, M. Volonteri, M. (2017). Constraining supermassive black hole evolution through the continuity equation. Astronomy & Astrophysics, 600:A64.

Turner, E. L. Gott, J. R., I. (1976). Groups of galaxies. I. A catalog. The Astrophysical Journal Supplement Series, 32:409–427.

Urry, C. M. Padovani, P. (1995). Unified Schemes for Radio-Loud Active Galactic Nuclei. The Publications of the Astronomical Society of the Pacific, 107:803.

Valenti, S., Sand, D. J., Barth, A. J., *et al.* (2015). Robotic Reverberation Mapping of Arp 151. The Astrophysical Journal Letters, 813(2):L36.

van den Bosch, F. C. (2002). The impact of cooling and feedback on disc galaxies. Monthly Notices of the Royal Astronomical Society, 332(2):456–472.

van den Bosch, R. C. E. (2016). Unification of the fundamental plane and Super Massive Black Hole Masses. The Astrophysical Journal, 831(2):134.

van den Bosch, R. C. E., Gebhardt, K., Gültekin, K., *et al.* (2015). Hunting for Supermassive Black Holes in Nearby Galaxies With the Hobby-Eberly Telescope. The Astrophysical Journal Supplement Series, 218(1):10.

Vázquez-Mata, J. A., Hernández-Toledo, H. M., Avila-Reese, V., *et al.* (2022). SDSS IV MaNGA: visual morphological and statistical characterization of the DR15 sample. Monthly Notices of the Royal Astronomical Society, 512(2):2222–2244.

Veilleux, S., Kim, D. C., Sanders, D. B., *et al.* (1995). Optical Spectroscopy of Luminous Infrared Galaxies. II. Analysis of the Nuclear and Long-Slit Data. The Astrophysical Journal Supplement Series, 98:171.

Véron-Cetty, M. P. Véron, P. (2006). A catalogue of quasars and active nuclei: 12th edition. Astronomy & Astrophysics, 455(2):773–777.

Vorontsov-Velyaminov, B. A. (1959). Atlas i Katalog Vzaimodejstvuûših Galakatik I.Atlas i Katalog Vzaimodejstvuûših Galakatik I.Atlas and catalog of interacting galaxies. 1959, Sternberg Institute, Moscow State University. Atlas and Catalog of Interacting Galaxies (1959, p. 0.

Wake, D. A., Bundy, K., Diamond-Stanic, A. M., *et al.* (2017). The SDSS-IV MaNGA Sample: Design, Optimization, and Usage Considerations. The Astronomical Journal, 154(3):86.

Walcher, J., Groves, B., Budavári, T., Dale, D. (2011). Fitting the integrated spectral energy distributions of galaxies. Astrophysics and Space Science, 331:1–52.

Walters, D., Woo, J., Ellison, S. L. (2022). Quenching time-scales in the IllustrisTNG simulation. Monthly Notices of the Royal Astronomical Society, 511(4):6126–6142.

Wechsler, R. H. Tinker, J. L. (2018). The Connection Between Galaxies and Their Dark Matter Halos. Annual Review of Astronomy & Astrophysics, 56:435–487.

Weedman, D. W. (1973). A Photometric Study of Markarian Galaxies. The Astrophysical Journal, 183:29–40.

Weinberger, R., Springel, V., Hernquist, L., *et al.* (2017). Simulating galaxy formation with black hole driven thermal and kinetic feedback. Monthly Notices of the Royal Astronomical Society, 465(3):3291–3308.

Weinberger, R., Springel, V., Pakmor, R., *et al.* (2018). Supermassive black holes and their feedback effects in the IllustrisTNG simulation. Monthly Notices of the Royal Astronomical Society, 479(3):4056–4072.

Westfall, K. B., Cappellari, M., Bershady, M. A., *et al.* (2019). The Data Analysis Pipeline for the SDSS-IV MaNGA IFU Galaxy Survey: Overview. The Astronomical Journal, 158(6):231.

White, R. A., Bliton, M., Bhavsar, S. P., *et al.* (1999). A Catalog of Nearby Poor Clusters of Galaxies. The Astronomical Journal, 118(5):2014–2037.

White, S. D. M. Frenk, C. S. (1991). Galaxy Formation through Hierarchical Clustering. The Astrophysical Journal, 379:52.

White, S. D. M. Rees, M. J. (1978). Core condensation in heavy halos: a two-stage theory for galaxy formation and clustering. Monthly Notices of the Royal Astronomical Society, 183:341–358.

Willmer, C. N. A. (2018). The Absolute Magnitude of the Sun in Several Filters. The Astrophysical Journal Supplement Series, 236(2):47.

Woo, J. Ellison, S. L. (2019). Two growing modes and the morphology-quiescence relation in isolated galaxies. Monthly Notices of the Royal Astronomical Society, 487(2):1927–1945.

Woo, J.-H., Cho, H., Gallo, E., et al. (2019). A 10,000-solar-mass black hole in the nucleus of a bulgeless dwarf galaxy. Nature Astronomy, 3:755–759.

Worthey, G. (1993). The Dependence of the Brightness Fluctuation Distance Indicator on Stellar Population Age and Metallicity. The Astrophysical Journal, 409:530.

Wright, E. L., Eisenhardt, P. R. M., Mainzer, A. K., et al. (2010). The Wide-field Infrared Survey Explorer (WISE): Mission Description and Initial On-orbit Performance. The Astronomical Journal, 140(6):1868–1881.

Yan, R., Tremonti, C., Bershady, M. A., et al. (2016). SDSS-IV/MaNGA: Spectrophotometric Calibration Technique. The Astronomical Journal, 151(1):8.

Zel'dovich, Y. B. Novikov, I. D. (1964). Estimating the Mass of a Super-Star. Doklady Akademii Nauk SSSR, 158(4):811–814.

Zhang, S.-N., Gu, Q.-S., Wang, Y.-P. (2008). Circumnuclear Star Forming Activity in NGC 3982. , 8(5):555–565.

Zhang, S. N., Ji, L., Kallman, T. R., et al. (2015). Modelling warm absorption in HST/COS spectrum of Mrk 290 with XSTAR. Monthly Notices of the Royal Astronomical Society, 447(3):2671–2682.

Zhang, S. N., Ji, L., Marshall, H. L., et al. (2011). Chandra and XMM-Newton view of the warm absorbing gas in Mrk 290. Monthly Notices of the Royal Astronomical Society, 410(4):2274–2290.

Zolotov, A., Dekel, A., Mandelker, N., et al. (2015). Compaction and quenching of high-z galaxies in cosmological simulations: blue and red nuggets. Monthly Notices of the Royal Astronomical Society, 450(3):2327–2353.

Zwicky, F. Zwicky, M. A. (1971). Catalogue of selected compact galaxies and of post-eruptiv